

SEICING IN FLAT-BOTTOMED BASINS: AN APPLICATION

OF MULTIMODE TRANSPORT METHODS

Frank I. González

Hawaii Institute of Geophysics
University of Hawaii, Honolulu

and

Joint Tsunami Research Effort
Pacific Marine Environmental Laboratory
National Oceanic and Atmospheric Administration

March 1977

Harold S. Loomis
Director
Joint Tsunami Research Effort

C. H. Lee
Director
Hawaii Institute of Geophysics

ABSTRACT

Calculations of eigencurves have been made for the three cases of rotating rectangular, trapezoidal, and circular segment basins, all with flat bottoms. These eigencurves yield eigenfrequencies for basins of given geometry and rotation or conversely, geometry and rotational parameters for a given frequency.

Using these curves to obtain an eigenfrequency, calculations of eigenmodes were also made for selected basins representative of the three classes.

The computations agree well with previously obtained results and indicate that the multimode transport approach to these problems is a viable one.

SEICHING IN FLAT-BOTTOMED BASINS: AN APPLICATION
OF MULTIMODE TRANSPORT METHODS

By

Frank I. González

1. INTRODUCTION

Recent reports (Preisendorfer, 1975; González, 1975) have applied multimode transport theory to two-dimensional time-harmonic, long surface waves in irregular basins. These works were principally theoretical; the main concern was to develop two-dimensional transport methods for linear hydrodynamics.

This study applies the resulting theory to the problem of seiching in irregular basins with flat bottoms. The flat bottom feature considerably simplifies the theory, while still retaining significant generality and usefulness.

Calculations of eigencurves were performed for the cases of rotating rectangular, trapezoidal, and circular segment basins.

2. PHYSICAL SETTING

The types of basins we will consider are illustrated below.

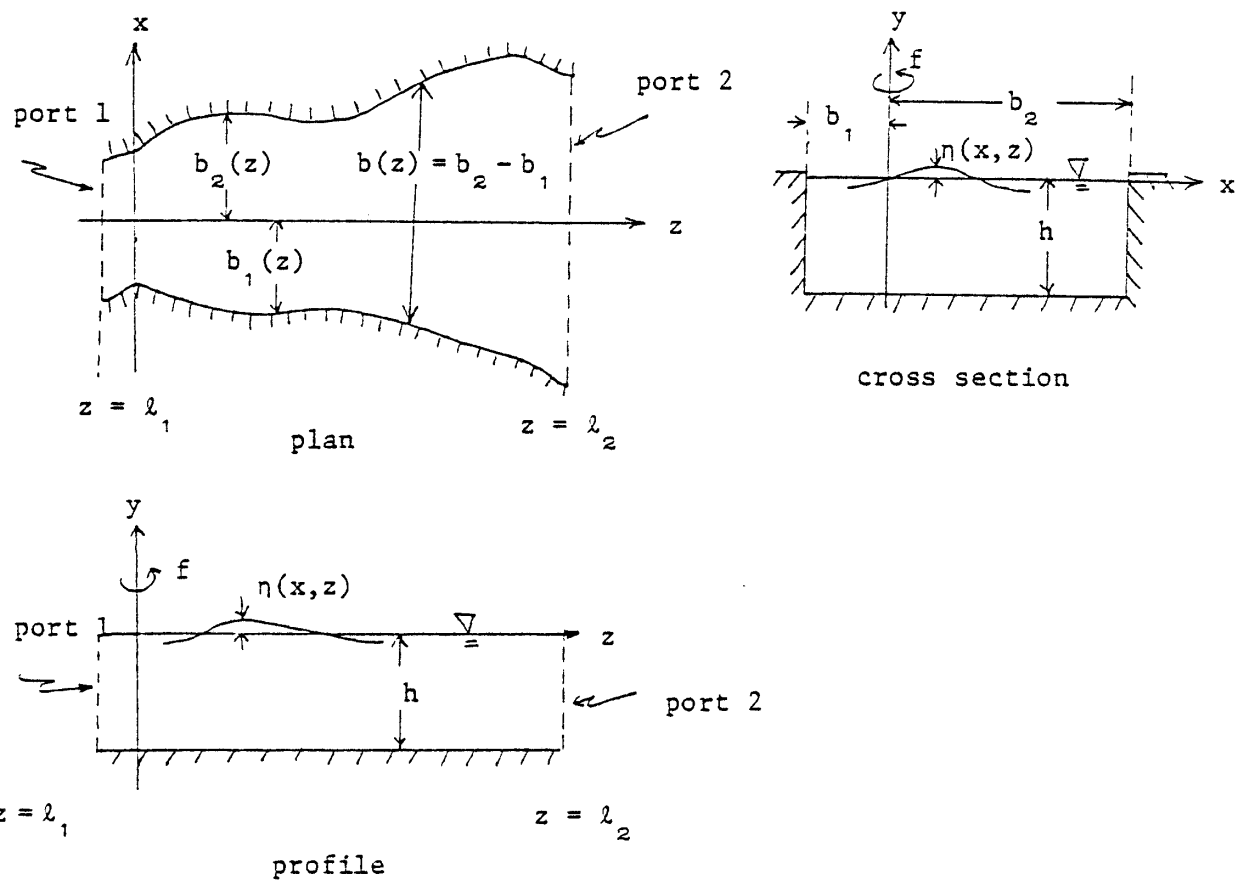


Figure 1. Flat-bottomed basins and notation.

As shown, $n(x, z)$ is the time harmonic deviation from mean water level; the constant depth is h ; the breadth is given by $b(z) = b_2(z) - b_1(z)$, and the ports by $z = \lambda_1$, $z = \lambda_2$; the entire basin rotates around the y -axis with constant angular velocity f (the f -plane approximation).

3. THE PARTIAL DIFFERENTIAL EQUATIONS AND BOUNDARY CONDITIONS

For time-harmonic motion in a frictionless, sourceless basin, the governing equations are given by

$$\left. \begin{aligned} \frac{\partial \eta}{\partial z} &= k_+ (\tilde{\phi} - i f \bar{\phi}) \\ \frac{\partial \eta}{\partial x} &= k_+ (\bar{\phi} + i f \tilde{\phi}) \end{aligned} \right\} \quad \text{(dynamic equations)} \quad (3.1)$$

$$\frac{\partial \tilde{\phi}}{\partial z} + \frac{\partial \bar{\phi}}{\partial x} = i \sigma \eta \quad \text{(continuity equation)} \quad (3.2)$$

Here $\bar{\phi}$ and $\tilde{\phi}$ are the mass transports per unit breadth

$$\bar{\phi} = hu$$

$$\tilde{\phi} = hw$$

with u and w the water velocities in the x and z directions, respectively. The time dependence of the complex field variables η , $\bar{\phi}$, $\tilde{\phi}$ is recovered on multiplication by the factor $e^{-i\sigma t}$, where σ is the time-harmonic frequency of the oscillation.

The coefficients are

$$k_+ = \frac{i\sigma}{gh} \quad (3.3)$$

and the nondimensional Coriolis parameter

$$f = 2 \frac{\Omega}{\sigma} \sin \theta \quad (3.4)$$

where Ω and θ are the earth's angular rotation rate and latitude, respectively.

If we introduce the nondimensional variables

$$\left. \begin{aligned} \eta_0 &= k_0 \eta & \tilde{\phi}_0 &= k_+ \tilde{\phi} & \bar{\phi}_0 &= k_+ \bar{\phi} \\ x_0 &= k_0 x & z_0 &= k_0 z & b_0 &= k_0 b \\ k_0 &= \frac{\sigma}{\sqrt{gh}} \end{aligned} \right\} \quad (3.6)$$

then drop the subscript zero for brevity, the dynamic and continuity equations become

$$\left. \begin{aligned} \eta' &= \tilde{\phi} - i f \bar{\phi} \\ \eta' &= \bar{\phi} + i f \tilde{\phi} \end{aligned} \right\} \quad \begin{array}{l} \text{(dimensionless} \\ \text{dynamic} \\ \text{equations)} \end{array} \quad (3.7)$$

$$\tilde{\phi}' + \bar{\phi}' = -\eta \quad \begin{array}{l} \text{(dimensionless} \\ \text{continuity equation)} \end{array} \quad (3.8)$$

where we have introduced the notation for partial derivatives

$$\psi'(x, z) = \frac{\partial \psi}{\partial x}(x, z)$$

$$\psi'(x, z) = \frac{\partial \psi}{\partial z}(x, z)$$

On eliminating $\bar{\phi}$ and $\tilde{\phi}$ in turn, the dynamic equations yield

$$\left. \begin{aligned} \tilde{\phi} &= \frac{1}{(1-f^2)} (\eta' + i f \eta') \\ \bar{\phi} &= \frac{1}{(1-f^2)} (\eta' - i f \eta') \end{aligned} \right\} \quad (3.9)$$

which, on insertion into the continuity equation, yields the *basin equation*

$$\eta'' + \eta' + k^2 \eta = 0 \quad (3.10)$$

with

$$k^2 \equiv 1 - f^2 . \quad (3.11)$$

At the boundaries of the basin, we require the normal component of the flow to vanish, which gives rise to the familiar condition

$$\bar{\phi}(b_k, z) = b_k'(z) \tilde{\phi}(b_k, z) ; \quad k = 1, 2 \quad (3.12)$$

or, using (3.9),

$$\eta'(b_k, z) = 2B(b_k, z)\eta'(b_k, z) ; \quad k = 1, 2 \quad (3.13)$$

with

$$2B(b_k, z) = \frac{b_k' + if}{1 - ib_k'f} . \quad (3.14)$$

4. THE MULTIMODE CIRCUIT EQUATIONS

We now assume the wave elevation and the mass transport functions may be represented across the basin at each fixed z by eigenfunction expansions of the form

$$\eta(x, z) = \sum_{m=0}^{\infty} \eta_m(z) f_m(x|z) \quad (4.1)$$

$$\tilde{\phi}(x, z) = \sum_{m=0}^{\infty} \tilde{\phi}_m(z) f_m(x|z) \quad (4.2)$$

$$\bar{\phi}(x, z) = \sum_{m=0}^{\infty} \bar{\phi}_m(z) f_m(x|z) . \quad (4.3)$$

The eigenfunctions we choose are solutions of the eigenvalue problem

$$\left. \begin{aligned} f_m''(x|z) + k^2 f_m(x|z) &= \kappa_m^2(z) f_m(x|z) \\ f_m'(b_k|z) &= 0 ; \quad k = 1, 2 \end{aligned} \right\} \quad (4.4)$$

and are thus given by

$$f_m(x|z) = A_m(z) \cos [\lambda_m(z)(x-b_1)] \quad (4.5)$$

where

$$\left. \begin{aligned} \lambda_m^2 &= k^2 - \kappa_m^2 = 1 - f^2 - \kappa_m^2 = \left(\frac{m\pi}{b}\right)^2 \\ A_m &= \left[\frac{2 - I_{m0}}{b} \right]^{\frac{1}{2}} \end{aligned} \right\} \quad (4.6)$$

so that the family $\{f_m\}$ is orthonormal

$$\int_{b_1(z)}^{b_2(z)} f_m(x|z) f_n(x|z) dx = I_{mn} = \begin{cases} 0 ; & m \neq n \\ 1 ; & m = n \end{cases} \quad (4.7)$$

with I_{mn} the identity matrix.

Multiplying (4.1) to (4.3) by f_n and integrating across the breadth, this orthonormality property yields the following expressions for the coefficients of the expansions

$$\left. \begin{aligned} n_n(z) &= \int_{b_1(z)}^{b_2(z)} n(x, z) f_n(x|z) dx \\ \tilde{\phi}_n(z) &= \int_{b_1(z)}^{b_2(z)} \tilde{\phi}(x, z) f_n(x|z) dx \\ \bar{\phi}_n(z) &= \int_{b_1(z)}^{b_2(z)} \bar{\phi}(x, z) f_n(x|z) dx \end{aligned} \right\} \quad (4.8)$$

We proceed to obtain the governing differential equations for n_n and $\tilde{\phi}_n$. Multiplying (3.7) and (3.8) by f_n , integrating over $[b_1, b_2]$, then rearranging, we have

$$\left. \begin{aligned} \int n' f_n dx &= \int \tilde{\phi} f_n dx - if \int \bar{\phi} f_n dx \\ \int \tilde{\phi}' f_n dx &= - \int n f_n dx - \int \bar{\phi}^* f_n dx \\ \int \bar{\phi} f_n dx &= \int n^* f_n dx - if \int \tilde{\phi} f_n dx \end{aligned} \right\} \quad (4.9)$$

Here, and in what follows, we drop explicit reference to the independent variables x and z as well as to the limits of integration and summation. Explicit expressions will be reintroduced only when this is necessary to avoid confusion.

Combining (4.8) and (4.9) gives us

$$\left. \begin{aligned} \int n' f_n dx &= \tilde{\phi}_n - i f \bar{\phi}_n \\ \int \tilde{\phi}' f_n dx &= - n_n - \int \bar{\phi}' f_n dx \\ \bar{\phi}_n &= \int n' f_n dx - i f \tilde{\phi}_n \end{aligned} \right\} \quad (4.10)$$

and we see that there are four integrals which must be evaluated further.

By using Leibniz's rule to differentiate the first equation of (4.8), we have

$$n'_n = \int n' f_n dx + \int n f'_n dx + [b' n f_n]_1^2,$$

where the notation of the last term means to take a difference

$$[b'(z)\psi(x,z)]_1^2 = b'_2(z)\psi(b_2, z) - b'_1(z)\psi(b_1, z).$$

Rearranging the first expression and inserting the expansion (4.1) for n gives us

$$\int n' f_n dx = n'_n - \sum_m n_m \left[\int f_m f'_n dx + [b' f_m f_n]_1^2 \right]. \quad (4.11)$$

Now by differentiating (4.7), we also have

$$\int f'_m f_n dx + \int f_m f'_n dx + [b' f_m f_n]_1^2 = 0 \quad (4.12)$$

so that (4.11) can be written

$$\int \eta' f_n dx = \eta'_n + \sum_m \eta_m \int f'_m f_n dx . \quad (4.13)$$

We have thus obtained an expression for the first integral in (4.10) in terms of the expansion coefficients η_n and its derivatives.

In an identical manner, we find that

$$\int \tilde{\phi}' f_n dx = \tilde{\phi}'_n + \sum_m \tilde{\phi}_m \int f'_m f_n dx . \quad (4.14)$$

We turn now to the remaining two integrals of (4.10). An integration by parts gives us

$$\begin{aligned} \int \eta^* f_n dx &= [\eta f_n]_1 - \int \eta f_n^* dx \\ &= \sum_m \eta_m \left\{ [f_m f_n]_1^2 - \int f_m f_n^* dx \right\} \end{aligned}$$

where we have simply inserted (4.1) for the second step. Another integration by parts of the last integral then gives us

$$\int \eta^* f_n dx = \sum_m \eta_m \int f_m^* f_n dx . \quad (4.15)$$

Finally, we have that

$$\int \bar{\phi}^* f_n dx = [\bar{\phi} f_n]_1^2 - \int \bar{\phi} f_n^* dx .$$

At this point we take the critical step of introducing the boundary condition (3.12) into the first term on the right. This ensures

satisfaction of this condition by the expansion (4.1) to (4.3). (See Preisendorfer (1975) for the outline of a proof.) Thus

$$\int \bar{\phi} \cdot f_n dx = [b' \tilde{\phi} f_n]_1^2 - \int \bar{\phi} f_n' dx$$

or, introducing the expansions (4.2), (4.3),

$$\int \bar{\phi} \cdot f_n dx = \sum_m \tilde{\phi}_m [b' f_m f_n]_1^2 - \sum_m \bar{\phi}_m \int f_m f_n' dx . \quad (4.16)$$

By combining equations (4.10) to (4.16), we then have

$$\left. \begin{aligned} \eta'_n &= \tilde{\phi}_n - i f \bar{\phi}_n - \sum_m \eta_m \int f_m' f_n dx \\ \tilde{\phi}'_n &= -\eta_n + \sum_m \bar{\phi}_m \int f_m f_n' dx - \sum_m \tilde{\phi}_m \left\{ \int f_m' f_n dx + [b' f_m f_n]_1^2 \right\} \\ \bar{\phi}_n &= \sum_m \eta_m \int f_m' f_n dx - i f \tilde{\phi}_n \end{aligned} \right\} \quad (4.17)$$

If we now identify the matrices

$$\left. \begin{aligned} \int f_m' f_n dx &\equiv \tilde{D}_{mn} \\ \int f_m' f_n dx &\equiv \bar{D}_{mn} \\ \int f_m f_n' dx &\equiv \tilde{E}_{mn} \\ \int f_m f_n' dx &\equiv \bar{E}_{mn} \\ [b' f_m f_n]_1^2 &\equiv \hat{b}_{mn} \end{aligned} \right\} \quad (4.18)$$

and adopt an underbar to denote the row vectors

$$\underline{\eta} = (\eta_0, \eta_1, \eta_2, \dots)$$

$$\underline{\phi} = (\phi_0, \phi_1, \phi_2, \dots)$$

$$\overline{\phi} = (\overline{\phi}_0, \overline{\phi}_1, \overline{\phi}_2, \dots) .$$

We may write (4.17) in the convenient vector matrix notation

$$\left. \begin{aligned} \underline{\eta}' &= \underline{\phi} - \text{if } \overline{\phi} - \underline{\eta} \tilde{D} \\ \underline{\phi}' &= -\underline{\eta} + \overline{\phi} \overline{E} - \underline{\phi}(\tilde{D} + \hat{b}) \\ \overline{\phi} &= \underline{\eta} \overline{D} - \text{if } \underline{\phi} \end{aligned} \right\} \quad (4.19)$$

In this notation, we have, from (4.12),

$$\tilde{D} + \hat{b} = -\overline{E} . \quad (4.20)$$

Inserting this, and eliminating $\overline{\phi}$ from the first two equations of (4.19), we get

$$\left. \begin{aligned} \underline{\eta}' &= \underline{\phi} K^+ + \underline{\eta} L^+ \\ \underline{\phi}' &= \underline{\eta} K^- + \underline{\phi} L^- \end{aligned} \right\} \quad (4.21)$$

where we have identified the coefficient matrices

$$\left. \begin{aligned} K^+ &= k^2 I \\ L^+ &= -\tilde{D} - \text{if } \overline{D} \\ K^- &= \overline{D} \overline{D} - I = \lambda^2 - I = -(\kappa^2 + f^2 I) \\ L^- &= \overline{E} - \text{if } \overline{E} \end{aligned} \right\} \quad (4.22)$$

The following expressions for the matrices in (4.18) and (4.22) are derived in the Mathematical Appendix.

$$\left. \begin{aligned} \bar{D}_{oo} &= \bar{E}_{oo} = 0 \\ \bar{D}_{on} &= \bar{E}_{no} = 0 \\ \bar{D}_{mo} &= \bar{E}_{om} = \frac{2^{\frac{1}{2}}}{b} [(-1)^m - 1] \\ \bar{D}_{mm} &= \bar{E}_{mm} = 0 \\ \bar{D}_{mn} &= \bar{E}_{nm} = \frac{2}{b} \left(\frac{m^2}{m^2 - n^2} \right) \left[(-1)^{m+n} - 1 \right]; \quad m \neq n \end{aligned} \right\} \quad (4.23)$$

$$\left. \begin{aligned} \tilde{D}_{oo} &= \tilde{E}_{oo} = -\frac{b'}{2b} \\ \tilde{D}_{on} &= \tilde{E}_{no} = 0 \\ \tilde{D}_{mo} &= \tilde{E}_{om} = -\frac{2^{\frac{1}{2}}}{b} [(-1)^m b'_2 - b'_1] \\ \tilde{D}_{mm} &= \tilde{E}_{mm} = -\frac{b'}{b} \\ \tilde{D}_{mn} &= \tilde{E}_{nm} = -\frac{2}{b} \left(\frac{m^2}{m^2 - n^2} \right) \left[(-1)^{m+n} b'_2 - b'_1 \right]; \quad m \neq n \end{aligned} \right\} \quad (4.24)$$

$$\left. \begin{aligned} \hat{b}_{oo} &= \frac{b'}{b} \\ \hat{b}_{on} &= \frac{2^{\frac{1}{2}}}{b} [(-1)^n b'_2 - b'_1] \\ \hat{b}_{mo} &= \frac{2^{\frac{1}{2}}}{b} [(-1)^m b'_2 - b'_1] \\ \hat{b}_{mm} &= 2 \frac{b'}{b} \\ \hat{b}_{mn} &= \frac{2}{b} [(-1)^{m+n} b'_2 - b'_1] \end{aligned} \right\} \quad (4.25)$$

$$\left. \begin{aligned} \bar{D} \bar{E} &= \lambda^2 \\ \lambda_{mn}^2 &= \lambda_m^2 I_{mn} \end{aligned} \right\} \quad (4.26)$$

Here λ_m is given by (4.6).

Equations (4.21) are known as the *multimode circuit equations*, by analogy with electrical circuit theory. Here η corresponds to voltage, while $\tilde{\phi}$ corresponds to current, and $(\eta, \tilde{\phi})$ are the coefficients of a Fourier-like decomposition of the two-dimensional field variables $(\eta, \tilde{\phi})$.

5. SEICHE CALCULATIONS VIA THE ADMITTANCE AND IMPEDANCE MATRICES

We wish to calculate the eigenfrequencies and eigenmodes at which a basin such as that in Figure 1 will oscillate. At the lateral boundaries, condition (3.12) must hold. This condition is satisfied by our multimode formulation, which introduces the boundary condition into the derivation of equation (4.16).

At the ends we must satisfy boundary conditions appropriate to open or closed ports. By a closed port we mean one which is impenetrable to flow, thus requiring that

$$\tilde{\phi}(x, z) = 0 ; \quad z = \ell_1 \text{ or } \ell_2 \quad (\text{closed port boundary condition}) \quad (5.1)$$

By an open port, we mean one which abuts an infinitely wide and/or infinitely deep sea. Since the principal purpose of this study is the testing and demonstration of the multimode transport techniques, we will forego a complicated analysis of the appropriate open boundary condition

and require, instead, the presence of a node. Thus,

$$\eta(x, z) = 0; \quad z = \ell_1 \text{ or } \ell_2 \quad (\text{open port boundary condition}). \quad (5.2)$$

Though strictly incorrect, this condition considerably simplifies the computations, while still at least roughly approximating the effects of an open port on seiching.

To translate these statements into restraints on the multimode vectors, we insert (4.1) and (4.2), obtaining the conditions

$$\sum_m \tilde{\phi}_m(\ell_k) f_m(x|\ell_k) = 0$$

$$\sum_m \eta_m(\ell_k) f_m(x|\ell_k) = 0 .$$

Since the members of the family $\{f_m\}$ are linearly independent, we must then require that

$$\left. \begin{aligned} \tilde{\phi}(\ell_k) &= 0; \quad k = 1, 2 \quad (\text{closed port at } z = \ell_k) \\ \eta(\ell_k) &= 0; \quad k = 1, 2 \quad (\text{open port at } z = \ell_k). \end{aligned} \right\} \quad (5.3)$$

A particular basin may have four different combinations of closed/open ports at $z = \ell_1, \ell_2$. They are

$$\left. \begin{aligned} \tilde{\phi}(\ell_1) &= 0 \\ \tilde{\phi}(\ell_2) &= 0 \end{aligned} \right\} \quad (\ell_1, \ell_2) = (\text{closed, closed}) = (c, c) \quad (5.4)$$

$$\left. \begin{aligned} \tilde{\phi}(\ell_1) &= 0 \\ \eta(\ell_2) &= 0 \end{aligned} \right\} \quad (\text{closed, open}) = (c, o) \quad (5.5)$$

$$\left. \begin{array}{l} \underline{\eta}(\ell_1) = 0 \\ \tilde{\phi}(\ell_2) = 0 \end{array} \right\} \quad (o,c) \quad (5.6)$$

$$\left. \begin{array}{l} \underline{\eta}(\ell_1) = 0 \\ \underline{\eta}(\ell_2) = 0 \end{array} \right\} \quad (o,o) \quad (5.7)$$

Of these four boundary value problems only the first three will be considered here, as they are the most important and frequently encountered.

To compute solutions of (4.21) subject to (5.4), (5.5), or (5.6), we define mutually inverse admittance and impedance matrices, such that

$$\tilde{\phi}(z) = \underline{\eta}(z)Y(z) \quad (5.8)$$

$$\underline{\eta}(z) = \tilde{\phi}(z)Z(z) \quad (5.9)$$

$$Z(z) = Y^{-1}(z) \quad . \quad (5.10)$$

To obtain the Riccati equations for Y and Z we first differentiate (5.8) and (5.9), using the circuit equations (4.21) to eliminate $\underline{\eta}'$ and $\tilde{\phi}'$

$$\tilde{\phi}' = \underline{\eta} K^- + \tilde{\phi} L^- = (\tilde{\phi} K^+ + \underline{\eta} L^+)Y + \underline{\eta} Y' = \underline{\eta}' Y + \underline{\eta} Y'$$

$$\underline{\eta}' = \tilde{\phi} K^+ + \underline{\eta} L^+ = (\underline{\eta} K^- + \tilde{\phi} L^-)Z + \tilde{\phi} Z' = \tilde{\phi}' Z + \tilde{\phi} Z' \quad .$$

We now use (5.8) and (5.9) in the first and second of these equations, respectively, and collect terms, to obtain

$$\underline{\eta}(Y' - K^- - YL^- + L^+Y + YK^+Y) = 0$$

$$\tilde{\phi}(Z' - K^+ - ZL^+ + L^-Z + ZK^-Z) = 0$$

which, for arbitrary $(\underline{n}, \tilde{\phi})$, requires that

$$Y' = K^- + Y L^- - L^+ Y - Y K^+ Y \quad (5.11)$$

$$Z' = K^+ + Z L^+ - L^- Z - Z K^- Z . \quad (5.12)$$

We note that these equations are dependent on the time-harmonic frequency, σ ; although this is not explicitly indicated here, its presence can be traced starting with equations (3.16). The same is true of the circuit equations (4.21).

As an example of how these equations would be used, consider the boundary conditions for the case (c, o) . Using (5.8) and (5.9) in (5.5), we have

$$\underline{n}(\ell_1) Y(\ell_1) = 0 \quad (5.13)$$

$$\tilde{\phi}(\ell_2) Z(\ell_2) = 0 . \quad (5.14)$$

Satisfying the first condition by setting

$$Y(\ell_1) = 0 \quad (5.15)$$

we choose a frequency, σ , and integrate (5.11) from ℓ_1 to ℓ_2 . If any singularities are encountered along the way, we switch to the integration of Z , using (5.10) and (5.12). If we have chosen a proper frequency, then (5.14) will hold on our arrival at $z = \ell_2$, thus requiring that the determinant of Z be zero. That is, we will find that

$$|Z(\ell_2)| = |Y^{-1}(\ell_2)| = 0 . \quad (5.16)$$

If this condition does in fact hold true, then (5.14) specifies an eigenvector problem for $\tilde{\phi}(\ell_z)$. Standard procedures, such as Gaussian elimination, will yield this special vector $\tilde{\phi}(\ell_z)$. With this eigenvector in hand, a solution of (4.21) subject to (5.5) can be obtained by its integration from $z = \ell_z$ to $z = \ell_1$ with initial values $(0, \tilde{\phi}(\ell_z))$ for the multimode vectors. Finally, the two-dimensional fields can be constructed using (4.1), (4.2), (4.3), and the last equation of (4.19).

If (5.16) is not satisfied, successive integrations with different frequencies must be tried until the correct frequency is zeroed in on. This would be the so-called "shooting method" and would be employed in the general case of a basin whose breadth could not be expressed as a simple analytic function.

In the case of basins with simple analytic breadth functions, invariant imbedding techniques can be used to generate families of eigencurves which yield eigenfrequencies for entire families of similar basins. In this method, a series of frequencies are chosen and an integration is made with each, while the condition (5.16) is monitored for those *eigenlengths*, $\ell_z(\sigma)$ for which it holds true. The technique was first used in a hydrodynamic setting by Preisendorfer and González (1973) and has been used in this study.

As an illustrative example, we first consider rectangular basins.

A. Rectangular Basins.

These basins are illustrated below.

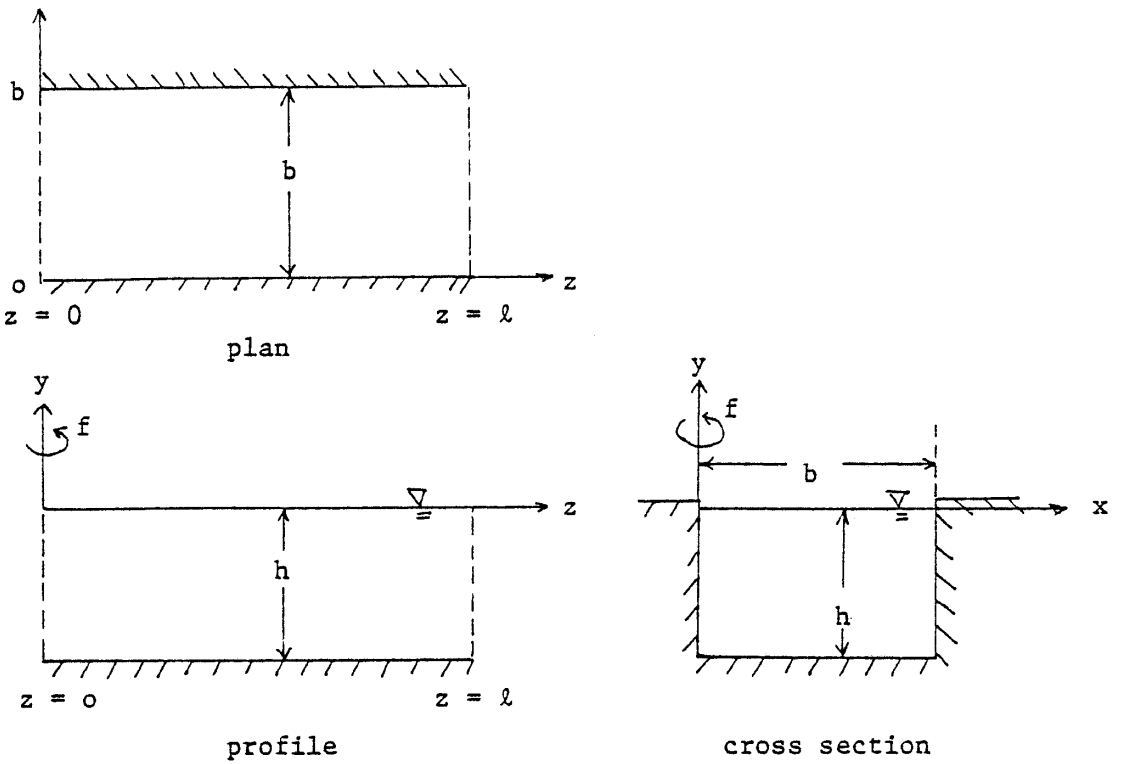


Figure 2. Rectangular basins.

Setting $b' = b'_1 = b'_2 = 0$ in (4.24) we find that (4.22) reduces to

$$\left. \begin{aligned} K^+ &= k^2 I \\ L^+ &= -if\bar{D} \\ K^- &= \lambda^2 - I = -(\kappa^2 + fI) \\ L^- &= -if\bar{E} \end{aligned} \right\} \quad (5.17)$$

With the breadth variation eliminated, equation (4.21) thus becomes a system of coupled equations with constant coefficients. In the simple static case of no rotation, with $f = 0$, these equations uncouple, becoming

$$\left. \begin{aligned} \eta'_m &= \tilde{\phi}_m \\ \tilde{\phi}'_m &= -\kappa_m^2 \eta_m \end{aligned} \right\} \quad (5.18)$$

By eliminating $\tilde{\phi}_m$, we obtain

$$\eta''_m + \kappa_m^2 \eta_m = 0 \quad (5.19)$$

which has solutions

$$\left. \begin{aligned} \eta_m(z) &= A_m \cos \kappa_m z + B_m \sin \kappa_m z \\ \tilde{\phi}_m(z) &= -\kappa_m (A_m \sin \kappa_m z - B_m \cos \kappa_m z) \end{aligned} \right\} \quad (5.20)$$

and thus

Application of the boundary conditions (5.4) to (5.7) with

$\lambda_1 \equiv 0$ and $\lambda_2 \equiv \lambda$ gives the following results for the four combinations of open and closed ports.

$$\left. \begin{aligned} \eta_m(z) &= A_m \cos \kappa_m z \\ \tilde{\phi}_m(z) &= -\kappa_m A_m \sin \kappa_m z \\ \kappa_m &= n\pi/\lambda ; \quad n = 1, 2, \dots \end{aligned} \right\} (c,c) \text{ ports} \quad (5.21)$$

$$\left. \begin{aligned} \eta_m(z) &= A_m \cos k_m z \\ \tilde{\phi}_m(z) &= -k_m A_m \sin k_m z \\ k_m &= (n + 1/2)\pi/\ell ; \quad n = 0, 1, 2, \dots \end{aligned} \right\} (c,o) \text{ ports} \quad (5.22)$$

$$\left. \begin{aligned} \eta_m(z) &= B_m \sin k_m z \\ \tilde{\phi}_m(z) &= k_m B_m \cos k_m z \\ k_m &= (n + 1/2)\pi/\ell ; \quad n = 0, 1, 2, \dots \end{aligned} \right\} (o,c) \text{ ports} \quad (5.23)$$

$$\left. \begin{aligned} \eta_m(z) &= B_m \sin k_m z \\ \tilde{\phi}_m(z) &= k_m B_m \cos k_m z \\ k_m &= n\pi/\ell ; \quad n = 1, 2, \dots \end{aligned} \right\} (o,o) \text{ ports} \quad (5.24)$$

These restrictions on k_m yield Merian's formulae for rectangular basins; thus, squaring the last expressions in (5.21) and (5.22), then inserting (4.6) for k_m , we get

$$1 = (m\pi/b)^2 + (n\pi/\ell)^2 \quad (c,c) \text{ and } (o,o) \text{ ports} \quad (5.25)$$

$$1 = (m\pi/b)^2 + [(n + 1/2)\pi/\ell]^2 \quad (c,o) \text{ and } (o,c) \text{ ports} \quad (5.26)$$

which are the usual eigenfrequency equations for rectangular basins, but in dimensionless disguise. (The dimensional statements can be recovered by using (3.6).) For our purposes, it is convenient to write them as

$$s^2 = m^2 + n^2 r^2 \quad (c,c) \text{ and } (o,o) \text{ ports} \quad (5.27)$$

$$s^2 = m^2 + (n + 1/2)^2 r^2 \quad (c,o) \text{ and } (o,c) \text{ ports} \quad (5.28)$$

where we have identified

$$s^2 \equiv (b/\pi)^2$$

$$r^2 \equiv (b/\ell)^2$$

for convenience. These relationships are illustrated in Figures 5, 6, 7, and 8 for several values of (m,n) , (see pp. 52 and 53).

It is instructive to examine how the Riccati equations would be used to construct these simple curves, since essentially the same methods were used to construct the corresponding curves for rotating and nonrectangular basins in the rest of the figures.

In the cases of (c,c) and (c,o) ports, with $f = 0$, Y and Z are diagonal

$$Y_{mm}(z) = \tilde{\phi}_m(z)/\eta_m(z) = -\kappa_m \tan \kappa_m z \quad (5.29)$$

$$Z_{mm}(z) = \eta_m(z)/\tilde{\phi}_m(z) = -\kappa_m^{-1} \cot \kappa_m z \quad (5.30)$$

and satisfy the reduced Riccati equations

$$Y'_{mm} = -\kappa_m^2 - Y_{mm}^2 \quad (5.31)$$

$$Z'_{mm} = 1 + \kappa_m^2 Z_{mm}^2 \quad . \quad (5.32)$$

Referring to Figure 5, we begin by choosing a value on the vertical axis, $s^2 = (b/\pi)^2$. Then $\kappa_m^2 = 1 - m^2(\pi/b)^2 = 1 - m^2/s^2$, and the integration of (5.31) can commence at $z = 0$ with $Y_{mm}(0) = 0$. As the integration proceeds and z increases, we move from right to left along the horizontal line $s^2 = (b/\pi)^2 = \text{constant}$, i.e., from $r^2 = (b/\ell)^2 = \infty$ toward $r^2 = (b/\ell)^2 = 0$. Since the solution evolves

according to (5.29), we will find that $|Y| = 0$ at $z = n\pi/\kappa_m$ for $n = 1, 2, \dots$, and $m = 0, 1, 2, \dots, < b/\pi = s$. (For $m > b/\pi = s$, κ_m is imaginary, and Y_{mm} is hyperbolic in nature and does not contribute to the zeros of $|Y|$.) These values of z are *eigenlengths* of the case (c,c) and will be located at the intersections of the curves in Figure 5 with the line $s^2 = (b/\pi)^2 = \text{constant}$.

Y has singularities at $z = (n + 1/2)\pi/\kappa_m$, and before these points are reached we must invert Y and switch to an integration of Z , using (5.32). $|Z| = 0$ at these singular points of Y , yielding the eigenlengths for the case (c,o) and providing data points for the construction of Figure 7.

How many data points will we obtain on one such integration sweep? Consider first only Figure 5, and thus those points for which $|Y| = 0$. In principle, if M is the largest integer less than $s = b/\pi$, and if the expansions (4.1) to (4.3) are truncated to $N + 1$ terms, so that Y and Z are $(N + 1)$ -square matrices, then we will find an $(M + 1)$ -fold or $(N + 1)$ -fold infinity of points, whichever is smaller. The same holds true for the data points of Figure 7, for which $|Z| = 0$. In practice, of course, we will be limited by such things as expense and loss of accuracy when integrating out to very large values of z .

Note that for large b and M , if we decide to truncate the multimode expansions to $(N + 1) < (M + 1)$ terms, then we limit the number of transverse modes we can detect. This is not surprising, since the expansions are made in a direction across the breadth of the basin.

This limitation on the number of transverse modes detectable in wide basins is probably true in general for this method. The results in this study were obtained with the multimode series expansions of (4.1) to (4.3) truncated to five terms.

B. Trapezoidal Basins

These basins are characterized by breadth functions

$$b(z) = 2b_2(z) = -2b_1(z) = b_0 + 2\beta z$$

$$b'(z) = 2b'_2(z) = -2b'_1(z) = 2\beta$$

$$\beta = \tan \gamma$$

where γ is the flare angle defined in Figure 3, below.

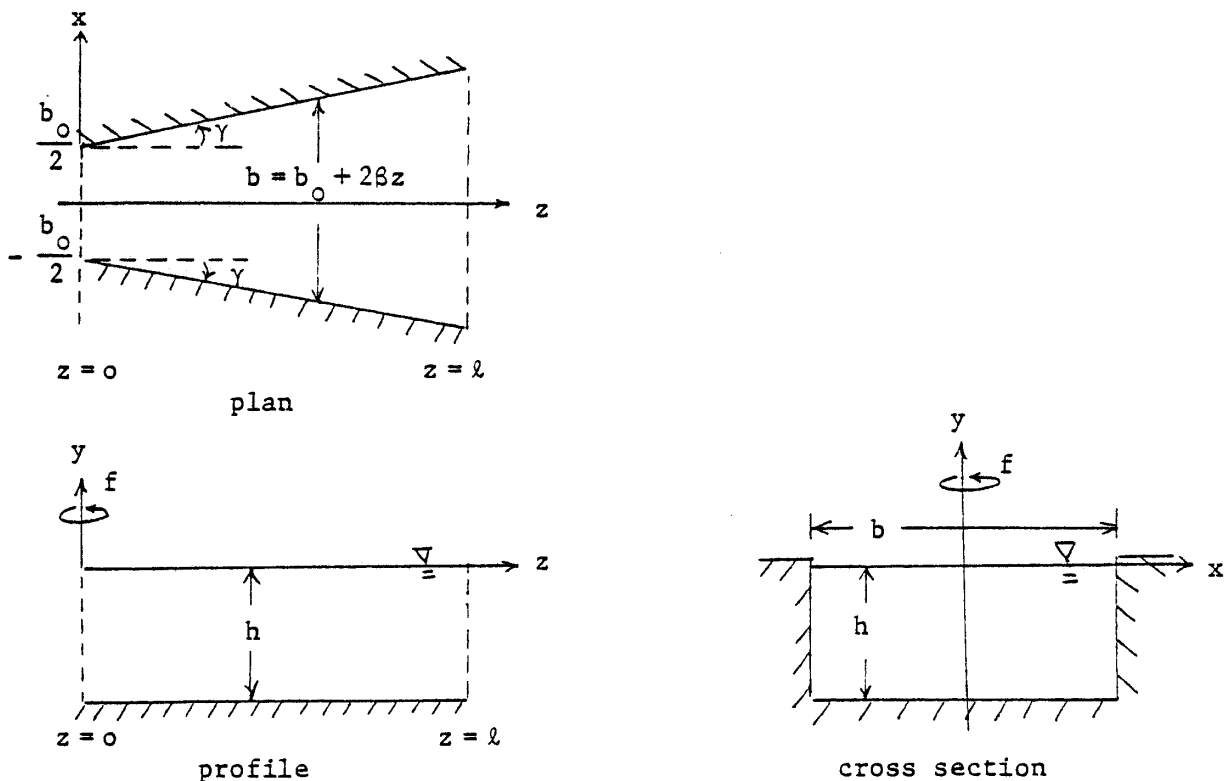


Figure 3. Trapezoidal basins.

Using these relationships in (4.22) to (4.25), we then have for the matrix coefficients

$$\begin{aligned}
 K_{mn}^+ &= (1-f^2) I_{mn} \\
 K_{mn}^- &= \left[\left(\frac{\pi}{b_0 + 2\beta z} \right)^2 - 1 \right] I_{mn} \\
 L_{mn}^+ &= - \left(L_{nm}^- \right)^* = \begin{cases} (2-I_{on}) \frac{\beta}{b_0 + 2\beta z} ; & m = n \\ \frac{2^{\frac{1}{2}} (2-I_{on})^{\frac{1}{2}}}{b_0 + 2\beta z} \left(\frac{\pi^2}{m^2 - n^2} \right) \left\{ \beta \left[1 + (-1)^{m+n} \right] + i f \left[1 - (-1)^{m+n} \right] \right\} ; & m \neq n \end{cases}
 \end{aligned}
 \tag{5.34}$$

We note that as $\gamma \rightarrow 0$, then $\beta \rightarrow 0$ and we return to the rectangular basins of the previous section.

For purposes of the eigencurve calculations of Figures 21 to 52 (pp.62-77) for these basins, we have defined the parameters s^2 and r^2 as

$$s^2 = \left[\frac{b(0)}{\pi} \right]^2$$

$$r^2 = \left[\frac{b(\lambda)}{\lambda} \right]^2 .$$

Note that as γ goes to zero we have $b(0) = b(\lambda)$, and we return to the case of rotating rectangular basins in the previous section.

C. Circular Segment Basins

Here the breadth functions are given by

$$b(z) = 2b_z(z) = -2b_1(z) = 2(2r_0 z - z^2)^{\frac{1}{2}}$$

$$b'(z) = 2b'_z(z) = -2b'_1(z) = 2(r_0 - z)(2r_0 z - z^2)^{-\frac{1}{2}} = 4(r_0 - z)/b$$

where r_0 is the (nondimensional) radius of the basin as shown in Figure 4, below.

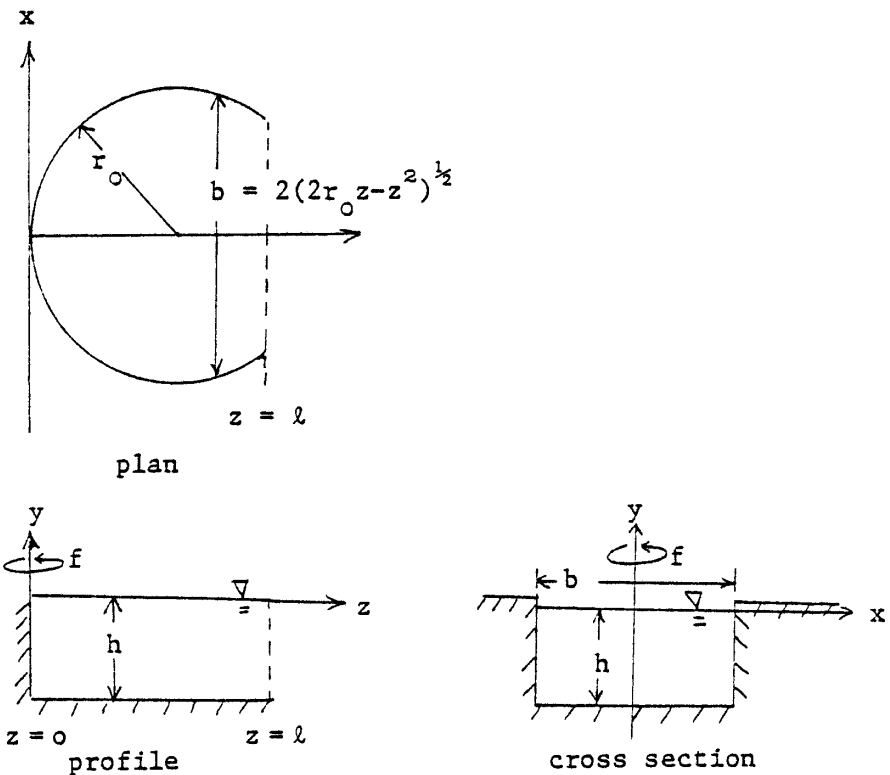


Figure 4. Circular segment basins.

With these breadth functions, the coefficient matrices become

$$\left. \begin{aligned}
 K_{mn}^+ &= (1-f^2) I_{mn} \\
 K_{mn}^- &= \left[\frac{(m\pi)^2}{4z(2r_o-z)} - 1 \right] I_{mn} \\
 L_{mn}^+ &= - \left(L_{nm}^- \right)^* = \begin{cases} \frac{(2-I_{on})}{2} \cdot \frac{(r_o-z)}{z(2r_o-z)} ; & m = n \\ \frac{(2-I_{on})^{1/2}}{2^{1/2}(2r_o z - z^2)^{1/2}} \left(\frac{m}{m^2-n^2} \right) \left\{ \frac{(r_o-z)}{(2r_o z - z^2)^{1/2}} \left[1 + (-1)^{m+n} \right] \right. \\ \left. + \text{ if } \left[1 - (-1)^{m+n} \right] \right\} ; & m \neq n \end{cases} \end{aligned} \right\} \quad (5.35)$$

The nondimensional parameters s^2 and r^2 are now defined as

$$s^2 = (r_o/\pi)^2$$

$$r^2 = (r_o/l)^2$$

for the eigencurves of Figures 53 to 64 (pp. 78-85)

6. DISCUSSION OF GRAPHS

A. Eigencurves for rotationless rectangular basins (Figures 5-8)

The curves for Figures 5 to 8 are eigencurves for rotationless rectangular basins. These curves were not obtained by individual integrations of the circuit equations, though they could have been, as explained in section 5A; rather, they were drawn using the analytic

expressions (5.27) and (5.28). These relationships are well known; they are simply Merian's formulae in nondimensional form. The nondimensional parameters s and r are given below (5.28).

It is instructive to use these graphs in a few simple examples. The use of the more general graphs for rotating basins of other shapes is similar.

Suppose we were given the dimensions h , b , and ℓ of a real basin, and we wished to find the eigenfrequency for the case in which the basin was closed at both ends. The following steps would lead to a determination of several eigenfrequencies for that particular basin.

1. Form $r = (b/\ell)$
2. Locate this value on the horizontal axis and draw a vertical line intersecting the eigencurves of each mode whose eigenfrequency we require.
3. Identify the vertical coordinate, s , for each intersection, using a horizontal line drawn to the vertical s -axis.
4. Compute (see (3.6)),

$$\sigma = \frac{s\pi}{b} \sqrt{gh}$$

for each of the values of s so obtained. The result is a set of eigenfrequencies for the modes of interest.

As an example, suppose we require eigenfrequencies for a closed, rotationless rectangular basin of breadth $b = 10$ km, length $\ell = 25$ km, and depth $h = 50$ m. Then $r = (0.4) = 0.16$, and we find that values of s^2 and s corresponding to the lowest four eigenfrequencies are:

$$s_{01}^2 = 0.16 \quad s_{01} = 0.40$$

$$s_{02}^2 = 0.64 \quad s_{02} = 0.80$$

$$s_{10}^2 = 1.00 \quad s_{10} = 1.00$$

$$s_{11}^2 = 1.16 \quad s_{11} = 1.08$$

where the subscripts refer to the mode numbers. Then, using $T = 2\pi/\sigma$ and $g = 9.8 \text{ m/sec}^2$, we compute the corresponding eigenperiods

$$T_{01} = \frac{1}{s_{01}} \cdot \frac{2b}{\sqrt{gh}} = \frac{903.51}{s_{01}} \text{ secs} = 2258 \text{ sec} = 37.6 \text{ min}$$

$$T_{02} = 18.82 \text{ min}$$

$$T_{10} = 15.06 \text{ min}$$

$$T_{11} = 13.82 \text{ min} .$$

If now, the corresponding eigenfrequencies were used to construct the coefficient matrices in (5.17), (with f set equal to zero for this rotationless case), the admittance and impedance equations (5.11) and (5.12) could be integrated from $z = l$ to $z = 0$ with $Y(l) = 0$. AT $z = 0$ we would find that $|Y(0)| = 0$, so that $\underline{\phi}(0) = \underline{n}(0)Y(0) = \underline{0}$ would specify an eigenvector problem for $\underline{n}(0)$. After obtaining $\underline{n}(0)$ by Gaussian elimination, we could integrate the circuit equations (4.21) from $z = 0$ to $z = l$, starting the integration with $(\underline{n}(0), \underline{0})$. This procedure would yield $\underline{n}(z)$ for all z , $0 \leq z \leq l$; finally, the two-dimensional sea surface elevation corresponding to each different eigen-mode could be constructed by use of the series (4.1).

The procedure just outlined was used to compute the eigenmodes for a small number of more complicated basins displayed in Figure 65 et sequentes (pp.86-105).

For this simplest case of a rotationless, closed rectangular basin, of course, the eigenmodes are given by

$$\eta_{mn}(x, z) = A_{mn} \cos \frac{m\pi}{b} x \cos \frac{n\pi}{l} z \quad m = 0, 1, 2, \dots \\ n = 1, 2, \dots$$

B. Eigencurves for Rotating Rectangular Basins (Figures 9-20)

The data points in Figures 9-65 are marked with a plus sign (+). Each of these data points was obtained by an integration of the admittance and impedance equations with the free dimensionless parameters f and b set to specific values in the coefficient matrices (5.17). The values of $|Y|$ and $|Z|$ were monitored during the integration so that, when an eigenlength λ was found such that $|Y| = 0$ or $|Z| = 0$, then the coordinates of the data point were computable as $s^2 = (b/\pi)^2$ and $r^2 = (b/\lambda)^2$. In Figure 10, for example, f was set equal to 0.25 and b was chosen during one integration run to be equal to $\sqrt{\pi/0.6}$ so that $s^2 = 0.6$. As the integration proceeded, an eigenlength was found at a distance about π units from the origin, so that r^2 was computed to be approximately $r^2 = (b/\lambda)^2 \approx (\pi \sqrt{0.6}/\pi)^2 \approx 0.6$, resulting in the lowest and leftmost data point in Figure 10. The solid lines are the eigencurves of Figures 5 to 8 for the rotationless cases; they were included to demonstrate the effects of rotation on the eigenfrequencies.

There are certain features we expect to find in such diagrams. Very small or very large values of r^2 correspond to basins which are long, narrow canals. In this type of setting, we expect only oscillations in

the longest dimension to be important and, furthermore, such oscillations should be relatively unaffected by rotation. Consequently, we expect eigencurves which approach asymptotically those of the rotationless longitudinal modes, $(0,1)$, $(0,2)$, ..., as r^2 gets very small and eigencurves which approach those of the rotationless transverse modes, $(1,0)$, $(2,0)$, ..., as r^2 gets very large. Both of these features can be seen in the diagrams.

In cases without rotation, there exist pairs of degenerate modes which oscillate at identical frequencies. These eigenmode pairs are known as *doublets*, and it is well known that rotation will cause the phenomenon known as *frequency splitting*, in which the frequency of each mode will shift such that each oscillates at a new, distinct frequency.

In Figure 6, for example, such doublets are manifested by the intersection of eigencurves for different modes. At such intersections, each basin of given geometry has two eigenmodes with the same eigenfrequency. In Figure 10, we see the effects of rotation on these doublets. Consider the region in the neighborhood $(r^2, s^2) = (1.0, 1.0)$. Here the rotationless doublet has disappeared, the intersecting solid lines being replaced by two divergent eigencurves.

On the other hand, we see in Figure 10 that, even with rotation, there are geometries for which doublets do exist. Consider, for example, the intersection of two eigencurves at coordinates $(r^2, s^2) \approx (3.33, 3.58)$. Since $f = 2\omega \sin \theta/\sigma$ in Figure 10, then $\sigma = 2\omega \sin \theta/0.25$. Then for any given latitude θ , there will be two different eigenmodes with that same eigenfrequency for any basin with geometry such that the relations $b/l = r = \sqrt{3.33} = 1.82$ and $\sigma b/\pi \sqrt{gh} = s = \sqrt{3.58} = 1.89$ are satisfied.

As the integration of the matrix equations proceeds away from the origin, the value of r will decrease; as this process continues we expect a deterioration of accuracy in the results. Since the basins are closed rectangles, there is an internal consistency check we can perform which will indicate the accuracy of the computations. Thus, if we interchange ℓ and b in the computations of r^2 and s^2 , we would expect these new data points to fall on existing eigencurves, namely these eigencurves of opposite transverse or longitudinal mode sense. Thus interchanging ℓ and b for points on a $(1,0)$ eigencurve should transform these points to values on the $(0,1)$ eigencurve. This was done, and the results are indicated by x 's rather than $+$'s in Figures 10-14. In general the new points deviate from the curves by as much as 4 or 5 percent. At least for small values of r , then, the accuracy of these curves can not be considered to be any greater than this amount.

As another check on the integrations, comparisons were made with the computations of Rao (1966), who obtained good agreement with tank experiments. The values of Tables 1 and 2 were obtained by interpolating values from Rao's Table 1; the fourth column lists the corresponding values read from the eigencurves of this study. We see that agreement is better for square basins, for which $r = 1$, than for the 2×1 rectangles, for which $r = 0.25$. This is to be expected, since the rectangles require twice the integration length. We also notice a rather consistent trend toward less accurate results at higher values of f . This is probably due to the fact that higher rotation usually results in spatially more complicated eigenmodes, and the limited number of

Table 1. Comparison of Square Basin Computations ($r = 1$) with the Results of Rao

Mode	f	Rao study s	Present study s	Percent difference
(1,0)	0.25	0.915	0.917	-0.26
	0.35	0.887	0.894	-0.85
	0.50	0.851	0.859	-0.94
(0,1)	0.25	1.124	1.127	-0.26
	0.35	1.191	1.198	-0.59
	0.50	1.323	1.330	-0.53
(1,1)	0.25	1.396	1.398	-0.14
	0.35	1.382	1.393	-0.8
	0.50	1.359	1.375	-1.2
(2,0)	0.25	2.040	2.044	-0.20
	0.35	2.082	2.085	-0.14
	0.50	2.144	2.182	-1.76
(0,2)	0.25	2.090	2.095	-0.24
	0.35	2.177	2.191	-0.64
	0.50	2.404	-	-
(1,2)	0.25	2.112	2.119	-0.33
	0.35	2.075	2.088	-0.63
	0.50	2.058	2.088	-1.46

eigenfunctions used is not sufficient to resolve the more complex sea surface topography.

Three examples of eigenmode calculations are given in Figures 65, 66, and 67. These correspond to Rao's (1966) Figures 4(a) (bottom), 6(a) (bottom), and 6(a) (top), respectively. In our Figures, s^2 and r^2 are printed out by the computer as S2 and R2. The units for the real part, imaginary part, and modulus of η (eta) are arbitrary. An overstrike with a minus sign indicates a negative value. The argument of η (arg eta) is plotted such that an area defined by a field of integers n means that in the defined field the argument takes on values

Table 2. Comparison of 2×1 Rectangular Basin ($r = 0.5$) Computations with the Results of Rao

Mode	f	Rao study s	Present study s	Percent difference
(0,1)	0.25	0.500	0.490	2.00
	0.35	0.499	0.500	-0.20
	0.50	0.498	0.490	1.61
(0,2)	0.25	0.989	0.975	1.42
	0.35	0.982	0.964	1.83
	0.50	0.967	0.933	3.52
(1,0)	0.25	1.008	1.030	-2.18
	0.35	1.015	1.063	-4.73
	0.50	1.031	1.127	-9.3
(1,1)	0.25	1.137	1.183	-4.05
	0.35	1.154	1.241	-7.54
	0.50	1.185	1.345	-13.5
(1,2)	0.25	1.398	1.382	1.14
	0.35	1.389	1.375	1.01
	0.50	1.377	1.396	-1.38
(0,3)	0.25	1.527	1.587	-3.93
	0.35	1.548	1.655	-6.90
	0.50	1.584	1.769	-11.70
(1,3)	0.25	1.794	1.783	0.61
	0.35	1.788	1.783	0.28
	0.50	1.778	1.769	0.51
(2,0)	0.25	2.011	2.045	-1.69
	0.35	2.022	2.092	-3.46
	0.50	2.044	2.177	-6.51
(0,4)	0.25	2.026	2.095	-3.43
	0.35	2.048	2.184	-6.65
	0.50	2.093	-	-
(2,1)	0.25	2.069	2.090	-1.01
	0.35	2.077	2.126	-2.36
	0.50	2.091	2.209	-5.63

between $30 \cdot n$ and $30 \cdot n + 15$ degrees; the letters A and B take on values of 10 and 11.

These three eigenmodes compare very well with those found in Rao (1966), but there are differences. Most notably there are slight

asymmetries in the wave patterns of Figures 65 and 66 which would not exist if the basins were exactly square and r^2 were exactly equal to 1. This slight deviation from a square is due to some difficulty in choosing the free parameters f and b in our integration such that when an eigenlength is found, a match is made to the parameters $f/\gamma_1 = 2\omega l \sin \theta/\pi \sqrt{gh}$ and $\sigma/\gamma_1 = \sigma l/\pi \sqrt{gh}$ in the figures of Rao (1966). Note also the double amphidromic point in Figure 66, while the corresponding diagram in Rao shows only a single amphidromic point; this illustrates the sensitivity of the solution to slight variations in the free parameters f and b .

C. Eigencurves for Trapezoidal Basins (Figures 21-52)

If we flare the sides of a basin by a small angle γ , we obtain the trapezoidal basins of Figure 3. Figures 21 and 22 demonstrate the effect of this flare on the eigenfrequencies. For the small angle $\gamma = 2.5^\circ$, the purely longitudinal modes $(0,1), (0,2), \dots$, are least affected and lie very close to the solid eigencurves for the square rotationless basin. The frequencies of the transverse series $(1,0), (1,1), (1,2), \dots$, have been depressed somewhat, and the eigenfrequencies of the series $(2,0), (2,1), (2,2), \dots$, have been lowered further still. Presumably this trend continues with higher transverse modes. In Figure 37 we see that the imposition of a larger flare angle, $\gamma = 7.5^\circ$, increases the differences between the data points obtained and the square basin eigencurves.

In the rotationless setting, doublets exist in these types of basins, though perhaps shifted somewhat. For example, consider the

rectangular basin doublet in Figure 21 indicated by the intersection of the solid $(1,0)$ and $(0,2)$ eigencurves at $(r^2, s^2) = (0.25, 1)$; with the slight spreading of the sides by 2.5° , this point has migrated to a slightly higher frequency or wider, shallower basins at $(r^2, s^2) \approx (0.266, 1.06)$. Many other such doublets can be seen in this figure and the next, Figure 22. With the addition of rotation, however, in Figures 23 and 24 all such doublets except one disappear, the eigenfrequency involved being split into two separate frequencies. The existence of the remaining doublet, at $(r^2, s^2) \approx (0.354, 3.91)$, is questionable. It is obvious that the number and position of the existing data points in that region are insufficient to resolve a crossing from a near-incident grazing of the two eigencurves involved. We speculate that, unlike rectangular basins, the imposition of rotation on trapezoidal basins completely eliminates all doublets; degenerate eigenmodes seem to exist for rotating trapezoidal basins. Future computations are planned to resolve this point.

All of the foregoing comments seem to be applicable as well to the remaining cases of $(c,0)$, $(0,c)$, and $(0,0)$ ports displayed in the remaining figures of the trapezoidal basin series.

Several eigenmode calculations were made using information from the eigencurves. Figure 68 displays the second transverse eigenmode for a basin open at the wide end, $(c,0)$. This eigenmode corresponds to the data point in the upper right-hand corner of Figure 44 $(r^2, s^2) = (4.07, 4.80)$, and is associated with the eigencurve for the $(2,0)$ mode. The data point a couple of units to the left, $(r^2, s^2) = (1.95, 4.80)$, is associated with the eigencurve $(0,1)$ and the corresponding eigenmode calculations produce

Figure 69. Note that both calculations evidently satisfy the boundary condition at the open end, where the wave elevation must be zero. If the open and closed ports are reversed, it appears that the principal result is to change the phase by 180° and move the surface pattern about a quarter wavelength toward the narrow end. To see this, compare Figures 69 and 70. Figure 70 corresponds to the data point $(r^2, s^2) = (2.05, 4.80)$ in Figure 48, and is also associated with the $(0, 1)$ eigen-curve. Some distortion does take place, of course, since now the wave elevation must be zero at the narrow end of the basin. (There is, in addition, another slight distortion in these three figures; due to a programming error in the plotting routine, the flare angle was plotted as 15° rather than 7.5° .)

D. Eigencurves for Circular Segment Basins (Figures 53-64)

The series of Figures 53 to 64 was obtained by integrating the admittance and impedance equations with the coefficients given by (5.35). The coordinate and abscissa, r^2 and s^2 are defined just below (5.35).

The eigenmodes for a closed circular basin of uniform depth are well known [see, for example, Lamb (1945), §210], and these solutions can be used as a check on the accuracy of the present computations.

Transforming (3.10) to polar coordinates ($x = \rho \sin \theta$, $z = \rho \cos \theta$) we get

$$\frac{\partial^2 \eta}{\partial \rho^2} + \frac{1}{\rho} \frac{\partial \eta}{\partial \rho} + \frac{1}{\rho^2} \frac{\partial^2 \eta}{\partial \theta^2} + k^2 \eta = 0$$

with boundary condition

$$\frac{\partial \eta}{\partial \rho} + \frac{if}{\rho} \frac{\partial \eta}{\partial \theta} = 0 \quad \text{at} \quad \rho = r_o \quad .$$

Solutions are given by

$$\eta = A J_m(\alpha) e^{im\theta}$$

where

$$\alpha = kp$$

and is such that it satisfies the transcendental equation

$$\alpha \frac{\partial J_m}{\partial \alpha} - m f J_m = 0 \quad .$$

Now the vertical axes $r^2 = 0.25$ in Figures 53, 55, and 57 correspond to a completely circular basin; the "+" data points to the left of these axes were obtained by solving the transcendental equation for successive values of m and for $f = 0, 0.25$, and 0.5 . For each root α we then have

$$s^2 = (r^2/\pi)^2 = (\alpha/k\pi)^2 = \alpha^2/\pi^2(1-f^2) \quad .$$

It can be seen that where enough data points exist to draw the eigencurves into the vertical axis, the correspondence is good for the first four or five eigenmodes. For higher modes, however, the accuracy of the integrations and the five-term series representation evidently begins to deteriorate, and the end points of the eigencurves do not extrapolate well to the expected intersections on the vertical axis.

A careful inspection of Figures 59-64 reveals that the first four or five modes also tend to the same limits at $r^2 = 0.25$. This is reasonable, since a completely circular basin with $(c,0)$ ports corresponds to an infinitely small opening at $z = l = 2r_0$; we would not expect a significant change of resonant frequencies of such a basin from its completely closed counterpart. In the case of the $(c,0)$ basins, however, additional modes appear, corresponding to the limit $s^2 = 0$ at $r = 0.25$. These are manifested by the bottom eigencurve in Figures 59 to 64. Since $s = r_0/\pi = \sigma r/\pi \sqrt{gh}$ (with r a dimensional quantity), this eigenmode for a complete circle with a pointlike open port evidently represents a flat surface with zero frequency of oscillation. Why this "quiescent mode" gives rise to nonquiescent modes for $r^2 > 0.25$ in the case of $(c,0)$ basins and not in the case of (c,c) basins is not clear at this time.

Figure 71 and 72 are examples of eigenmodes for $(c,0)$ basins which lie on eigencurves of Figure 62. They illustrate the effect of basin radius/length ratio on the type of oscillation for a given frequency. The length in Figure 71 is about half the radius, and the result is a single wave which rotates counterclockwise around a point near the head of the basin. At a basin length of about three quarters of the radius, we find an eigenmode with the same frequency but an altered surface configuration. Now two counterclockwise rotating waves can be seen in the basin, with amphidromic points located to the left and right of the basin axis.

E. Example of Use of Eigencurves

Suppose we wish to estimate the lowest eigenfrequencies of basins open to the sea which can be approximated by circular segment basins which have a radius-to-length ratio of $5/3$ or 1.67 . Then $r^2 = (1.67)^2 = 2.78$ and from Figures 60, 62, and 64 we have $s^2 = 0.93, 1.00$, and 1.14 for $f = 0, 0.25$, and 0.5 , respectively. To put this information into convenient form, we note that

$$s = \frac{\sigma}{\sqrt{gh}} \frac{v_o}{\pi} = \frac{2 r_o}{T \sqrt{gh}}$$

$$f = \frac{2\omega}{\sigma} \sin \theta = \frac{\omega T}{\pi} \sin \theta$$

where T is the period and r_o and h are now dimensional quantities. We then have, after some algebra,

$$\sin \theta = p \frac{\sqrt{h}}{r_o}$$

$$T = q \frac{r_o}{\sqrt{h}}$$

where

$$p \equiv \frac{\pi \sqrt{g}}{2\omega} \cdot fs$$

$$q = \frac{2}{\sqrt{g}} \cdot \frac{1}{s} .$$

Using $g = 9.8 \text{ m/sec}^2$ and $\omega = 7.29 \times 10^{-5}/\text{sec}$, we can then compute the following values:

P	q
0	0.663
1.69×10^4	0.640
7.22×10^4	0.597

Suppose now we are interested in a basin at 60° latitude, with $r_o = 50$ km, $\lambda = 30$ km, and $h = 25$ m. We thus require that

$$\sin \theta = 0.866 = p \frac{\sqrt{h}}{r_o} = p \frac{\sqrt{25}}{50 \times 10^3},$$

that is

$$p = \frac{0.866 \times 50 \times 10^3}{\sqrt{25}} = 0.866 \times 10^4.$$

By graphical means, we find that at this value of p , q is about 0.65, so that

$$T = q \frac{r_o}{\sqrt{h}} = \frac{0.65 \times 50 \times 10^3}{\sqrt{25}} = 6.5 \times 10^3 \text{ sec},$$

that is

$$T \approx 1.8 \text{ hours.}$$

Similar computations can be made using the eigencurves for rectangular and trapezoidal basins.

7. MATHEMATICAL APPENDIX I

For convenience, we repeat the following identities and equations.

The matrices in question are defined by

$$\bar{D}_{mn} = \bar{E}_{nm} = \int_{b_1}^{b_2} f_m^* f_n dx \quad (I.1)$$

$$\tilde{D}_{mn} = \tilde{E}_{nm} = \int_{b_1}^{b_2} f_m^* f_n dx \quad (I.2)$$

$$\hat{b}_{mn} = [b^* f_m f_n]_1^2 \quad (I.3)$$

where f_m satisfies the eigenvalue problem

$$f_m'' + \lambda_m^2 f_m = 0 \quad (I.4)$$

$$f_m(b_1) = f_m(b_2) = 0 \quad (I.5)$$

and is thus given by

$$f_m = A_m \cos \lambda_m (x - b_1) \quad (I.6)$$

$$\lambda_m = \frac{m\pi}{b} \quad (I.7)$$

$$A_m = \left(\frac{2 - I_{mo}}{b} \right)^{\frac{1}{2}} \quad . \quad (I.8)$$

We start with the evaluation of the matrix \bar{D} .

$$(1) \quad \bar{D}_{oo} .$$

Since $f'_o = 0$, we then have $\bar{D}_{oo} = 0$.

$$(2) \quad \bar{D}_{on}, \quad n \neq 0.$$

For the same reason, $\bar{D}_{on} = 0$.

$$(3) \quad \bar{D}_{mo}, \quad m \neq 0.$$

Here we have

$$\bar{D}_{mo} = A_o \int_1^2 f_m dx = A_o [f_m]_1^2. \quad .$$

Now

$$f_m(b_2) = A_m \cos \frac{m\pi}{b} (b_2 - b_1) = A_m \cos m\pi. \quad .$$

Therefore

$$f_m(b_2) = A_m (-1)^m. \quad . \quad (I.9)$$

Also

$$f_m(b_1) = A_m \cos \lambda_m (b_1 - b_1) = A_m. \quad . \quad (I.10)$$

Thus

$$\bar{D}_{mo} = A_o A_m [(-1)^m - 1]$$

$$\bar{D}_{mo} = \frac{2^{\frac{1}{2}}}{b} [(-1)^m - 1]; \quad m \neq 0. \quad . \quad (I.11)$$

$$(4) \quad \bar{D}_{mm}, \quad m \neq 0.$$

Here, note that

$$\int (f_m^2)^\cdot dx = [f_m^2]_1^2 = 2 \int f_m^\cdot f_m dx$$

so that

$$\bar{D}_{mm} = \int f_m^\cdot f_m dx = \frac{1}{2} [f_m^2]_1^2$$

and, using (I.9) and (I.10),

$$\bar{D}_{mm} = \frac{\lambda_m^2}{2} [(-1)^{2m} - 1] = 0; \quad m \neq 0 \quad (I.12)$$

$$(5) \quad \bar{D}_{mn}, \quad m \neq n, \quad m, n \neq 0.$$

Multiply (I.4) by f_n^\cdot , then integrate over $[b_1, b_2]$ to get

$$-\lambda_m^2 \int f_m f_n^\cdot dx = \int f_m^\cdot f_n^\cdot dx .$$

Integrating by parts on both sides,

$$-\lambda_m^2 [f_m f_n]_1^2 + \lambda_m^2 \int f_m^\cdot f_n dx = [f_m^\cdot f_n^\cdot]_1^2 - \int f_m^\cdot f_n^\cdot dx .$$

Using the boundary condition (I.5) and the equation (I.4), then solving for \bar{D}_{mn} , we get

$$\bar{D}_{mn} = \int f_m^\cdot f_n dx = \frac{\lambda_m^2}{\lambda_m^2 - \lambda_n^2} [f_m f_n]_1^2$$

Using (I.7) to (I.10) and simplifying,

$$\bar{D}_{mn} = \frac{m^2}{m^2 - n^2} \cdot \left(\frac{2}{b} \right) [(-1)^{m+n} - 1]; \quad m \neq n, \quad (I.13)$$

$m, n \neq 0$

Next we take \tilde{D} , defined by (I.2).

$$(1) \quad \tilde{D}_{oo}.$$

Here we have

$$\tilde{D}_{oo} = \int_{b_1}^{b_2} f'_o f_o dx = A'_o A_o \int_{b_1}^{b_2} dx = A'_o A_o b. .$$

Performing the indicated differentiation on (I.8) with $m = 0$ and simplifying,

$$\tilde{D}_{oo} = - \frac{b'}{2b} . \quad (I.14)$$

$$(2) \quad \tilde{D}_{on}, \quad n \neq 0.$$

Here

$$\tilde{D}_{on} = A'_o \int_{b_1}^{b_2} f_n dx .$$

Using (I.4)

$$\tilde{D}_{on} = - \frac{A'_o}{\lambda_n^2} \int_{b_1}^{b_2} f_n'' dx = - \frac{A'_o}{\lambda_n^2} [f_n'']_1^2$$

so that, by virtue of the boundary condition (I.5),

$$\tilde{D}_{on} = 0, \quad n \neq 0. \quad (I.15)$$

$$(3) \quad \tilde{D}_{mo}, \quad m \neq 0.$$

We first note that

$$\int_{b_1}^{b_2} f_m f_o dx = I_{mo} = 0 \quad .$$

Differentiating with respect to z , using Leibnitz' rule, we get

$$\int f'_m f_o dx + \int f_m f'_o dx + [b' f_m f_o]_1^2 = 0$$

which can be written

$$\tilde{D}_{mo} + \tilde{D}_{om} = - A_o [b' f_m]_1^2 \quad .$$

Using (I.15) and (I.8) to (I.10), we then get

$$\tilde{D}_{mo} = - \frac{2}{b} [(-1)^m b'_2 - b'_1]; \quad m \neq 0 \quad . \quad (I.16)$$

$$(4) \quad \tilde{D}_{mm}, \quad m \neq 0.$$

Here we start with

$$\int_{b_1}^{b_2} f_m^2 dx = I_{mm} = 1 \quad .$$

Differentiating with respect to z , again using Leibnitz' rule, we have

$$2 \int f'_m f_m dx + [b' f_m^2]_1^2 = 0$$

that is,

$$\tilde{D}_{mm} = -\frac{1}{2} [b' f_m^2]_1^2$$

or, using (I.8) to (I.10)

$$\tilde{D}_{mm} = -\frac{1}{b} [b'_2 (-1)^{2m} - b'_1]$$

that is,

$$\tilde{D}_{mm} = -\frac{b'}{b} . \quad (I.17)$$

$$(5) \quad \tilde{D}_{mn}; \quad m \neq n; \quad m, n \neq 0.$$

Consider the relation

$$\int (f_m' f_n')'' dx = [(f_m' f_n')']_1^2 . \quad (I.18)$$

Expanding the integral,

$$\int (f_m' f_n')'' dx = \int f_m''' f_n dx + 2 \int f_m'' f_n' dx + \int f_m' f_n'' dx .$$

Using (I.4) to replace f_m'' and f_n'' , and integrating the middle integral by parts,

$$\int (f_m' f_n')'' dx = \int (-\lambda_m^2 f_m')' f_n dx + 2 \left\{ [f_m' f_n']_1^2 - \int f_m' f_n'' dx \right\} - \lambda_n^2 \int f_m' f_n dx .$$

Again using (I.4) to replace f_n'' , applying the boundary condition (I.5), then expanding the first integral and collecting terms, we have

$$\int (f_m' f_n')'' dx = - \left(\lambda_m^2 \right)' I_{mn} - \left(\lambda_m^2 - \lambda_n^2 \right) \tilde{D}_{mn} . \quad (I.19)$$

Expanding the right side of (I.18) and applying (I.5), we have

$$[(f_m' f_n')']_1^2 = [f_m'' f_n']_1^2 + [f_m' f_n'']_1^2 = [f_m'' f_n'']_1^2 . \quad (I.20)$$

From (1.6) we form

$$f_m'(x|z) = A_m' \cos \lambda_m(x - b_1) - A_m [\lambda_m'(x - b_1) - \lambda_m b_1'] \sin \lambda_m(x - b_1)$$

$$\begin{aligned} f_m''(x|z) &= -\lambda_m A_m' \sin \lambda_m(x - b_1) - A_m \lambda_m' \sin \lambda_m(x - b_1) \\ &\quad - \lambda_m A_m [\lambda_m'(x - b_1) - \lambda_m b_1'] \cos \lambda_m(x - b_1) \end{aligned}$$

from which we obtain

$$f_m''(b_1|z) = \lambda_m^2 A_m b_1'$$

$$f_m''(b_2|z) = \lambda_m^2 A_m (-1)^m b_2' .$$

This last expression was obtained by using the relationship

$$\lambda_m' = -\lambda_m \frac{b'}{b}$$

obtained by differentiation of (I.7).

We thus have

$$[f_m'' f_n']_1^2 = 2 \frac{\lambda_m^2}{b} [(-1)^{m+n} b_2' - b_1']$$

and, combining this expression with (I.18) to (I.20), we get

$$(\lambda_m^2 - \lambda_n^2) \tilde{D}_{mn} = - \left(\lambda_m^2 \right)' I_{mn} - 2 \frac{\lambda_m^2}{b} [(-1)^{m+n} b_2' - b_1']$$

or, using (I.7) and setting $m \neq n$,

$$\tilde{D}_{mn} = - \frac{2m^2}{b(m^2 - n^2)} [(-1)^{m+n} b'_2 - b'_1] . \quad (I.21)$$

Turning now to (I.3), a straightforward use of (I.8) to (I.10) allows us to evaluate the members of the matrix \hat{b} . The results are given by (4.25) in the text and will not be repeated here.

Finally, we wish to prove the relationship

$$\overline{DE} = \lambda^2 .$$

We start by multiplying (I.4) by f_n , then integrating over $[b_1, b_2]$ to get

$$\int f_m'' f_n dx = - \lambda_m^2 \int f_m f_n dx = 0$$

or

$$\int f_m'' f_n dx = - \lambda_m^2 I_{mn} .$$

Integrating by parts, we have

$$[f_m' f_n']_1^2 - \int f_m' f_n' dx = - \lambda_m^2 I_{mn}$$

or, using, the boundary condition (I.5),

$$\int f_m' f_n' dx = \lambda_m^2 I_{mn} . \quad (I.22)$$

Now we have that

$$f_m^*(x) = \sum_{\ell} \bar{D}_{m\ell} f_{\ell}(x)$$

which can be proven by multiplying both sides by $f_n(x)$ and integrating over $[b_1, b_2]$. Then we can use this in (I.22) to obtain

$$\int \sum_{\ell} \bar{D}_{m\ell} f_{\ell} f_n^* dx = \sum_{\ell} D_{m\ell} \int f_{\ell} f_n^* dx = \lambda_m^2 I_{mn}$$

or,

$$\sum_{\ell} \bar{D}_{m\ell} \bar{E}_{\ell n} = \lambda_m^2 I_{mn}$$

which is the desired relationship.

8. ACKNOWLEDGMENTS

This work was performed at the Joint Tsunami Research Effort in Hawaii, while the author was supported by the National Research Council as a Resident Research Associate.

Ms. Louise L. Lembeck typed the manuscript and her able effort is gratefully acknowledged.

9. REFERENCES

- González, F. I. 1975. Multimode Long Wave Transport in Irregular Basins. *HIG-75-9, Hawaii Inst. Geophys.*, University of Hawaii, Honolulu, 202 pp.
- Lamb, H., 1945. *Hydrodynamics* (6th edition), Dover Press, New York.
- Preisendorfer, R. W. 1975. Multimode Long Surface Waves in Two-Port Basins. *HIG-75-4, Hawaii Inst. Geophys.*, University of Hawaii, Honolulu, 107 pp.
- Preisendorfer, R. W., and F. I. González. 1973. Classic Canal Theory. *HIG-73-14, Hawaii Inst. Geophys.*, University of Hawaii, Honolulu, Vol. I, 284 pp; Vol. 2, 433 pp.
- Rao, D. B. 1966. Free Gravitational oscillations in rotating rectangular basins, *J. Fluid Mech.* 25(3): 523-555.

Eigencurves and Eigenmodes

Figures 5 - 72

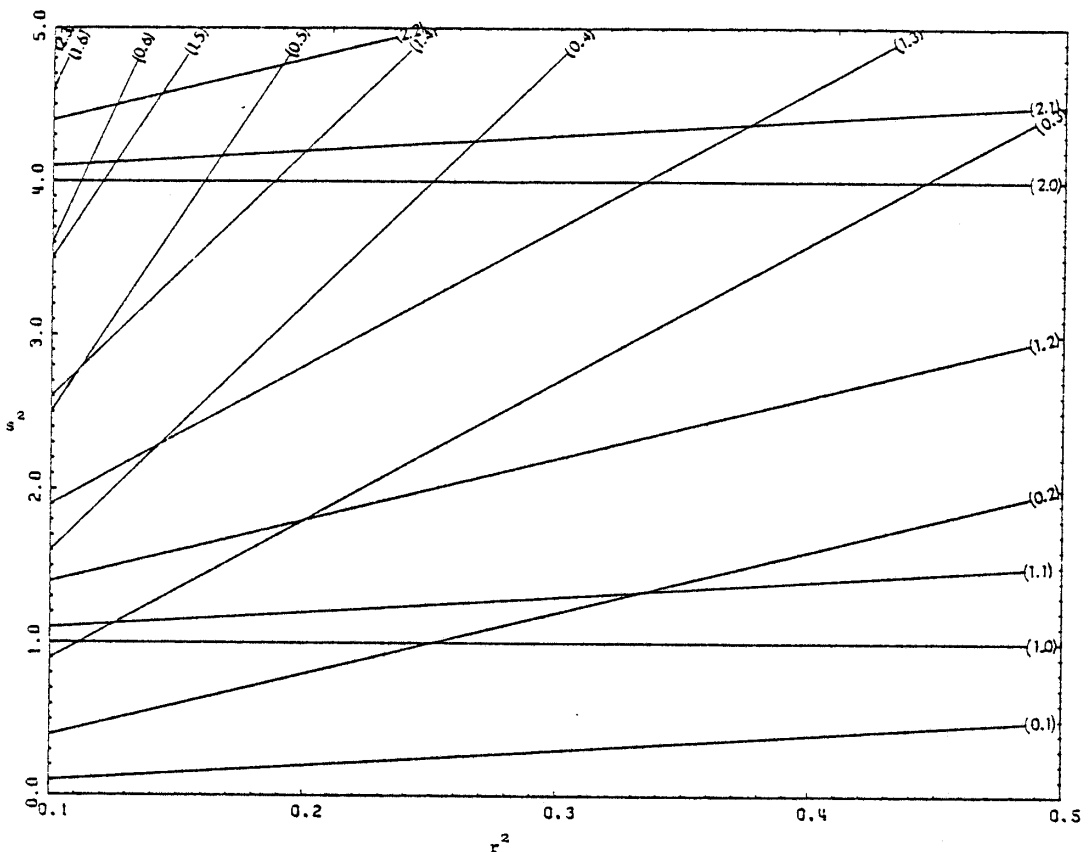


Figure 5. Eigencurves. Rectangular basins, (c,c) and $(0,0)$, $f=0$.

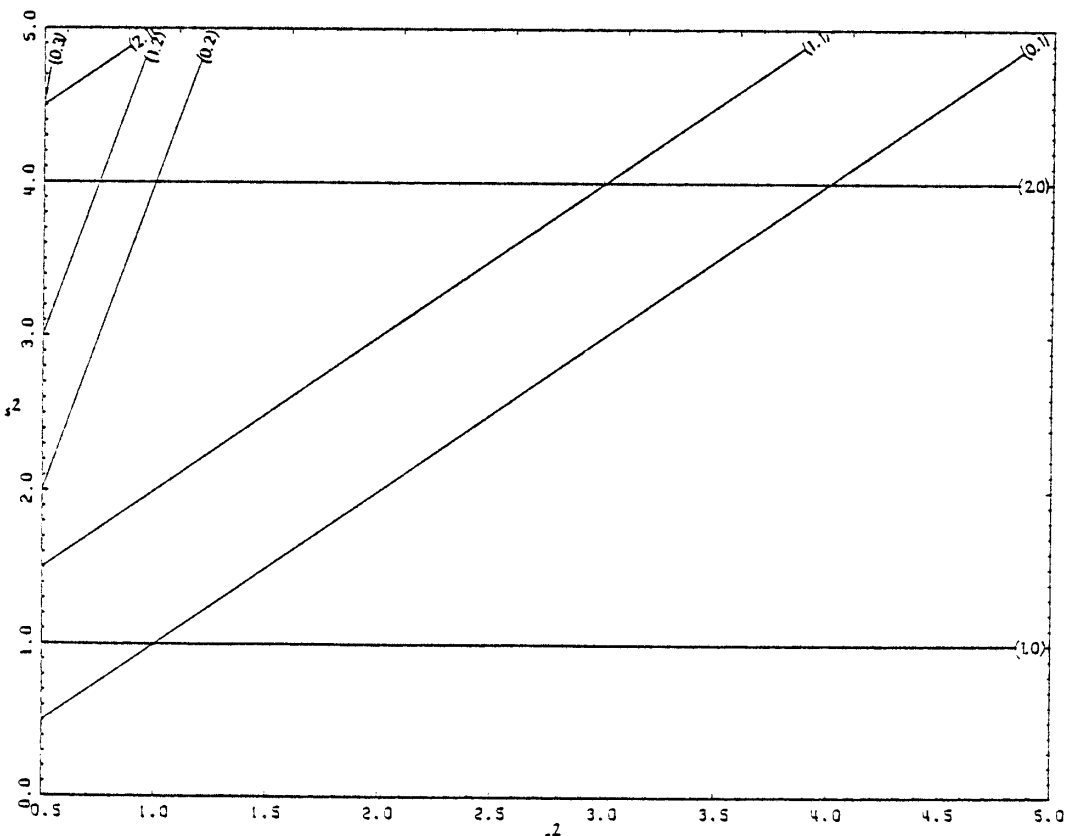


Figure 6. Eigencurves. Rectangular basins, (c,c) and $(0,0)$, $f=0$.

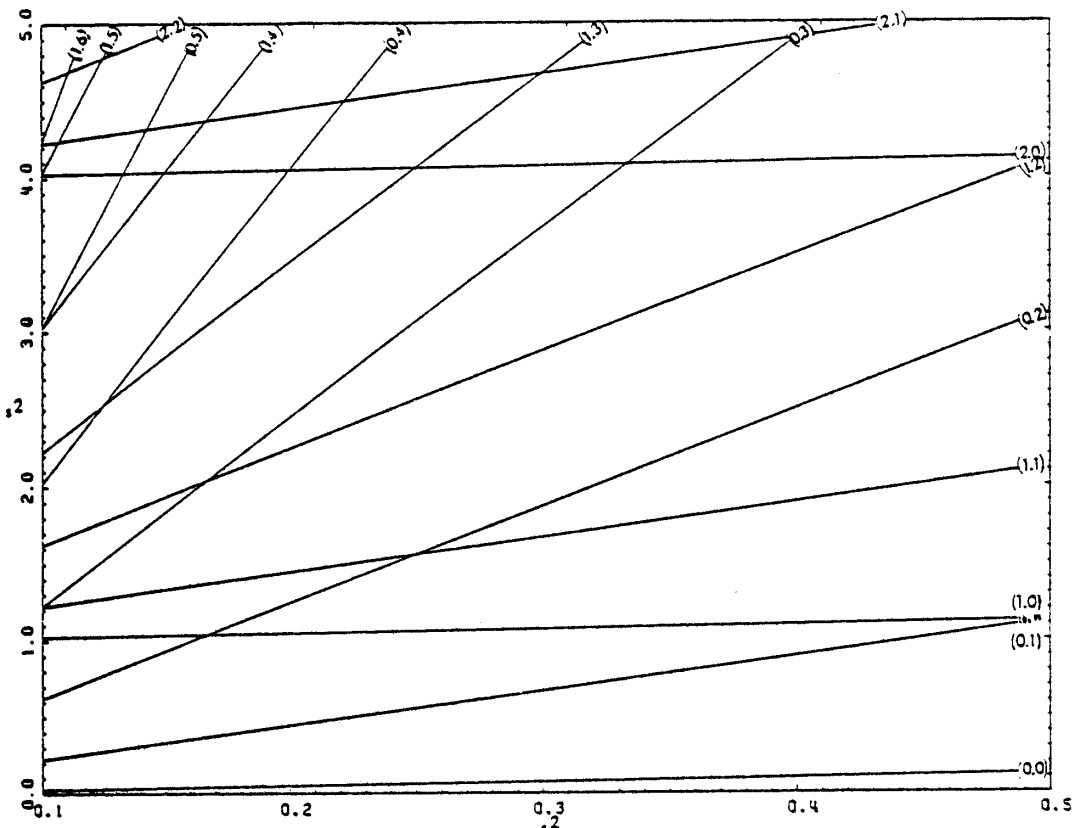


Figure 7. Eigencurves. Rectangular basins, $(c,0)$ and $(0,c)$, $f=0$.

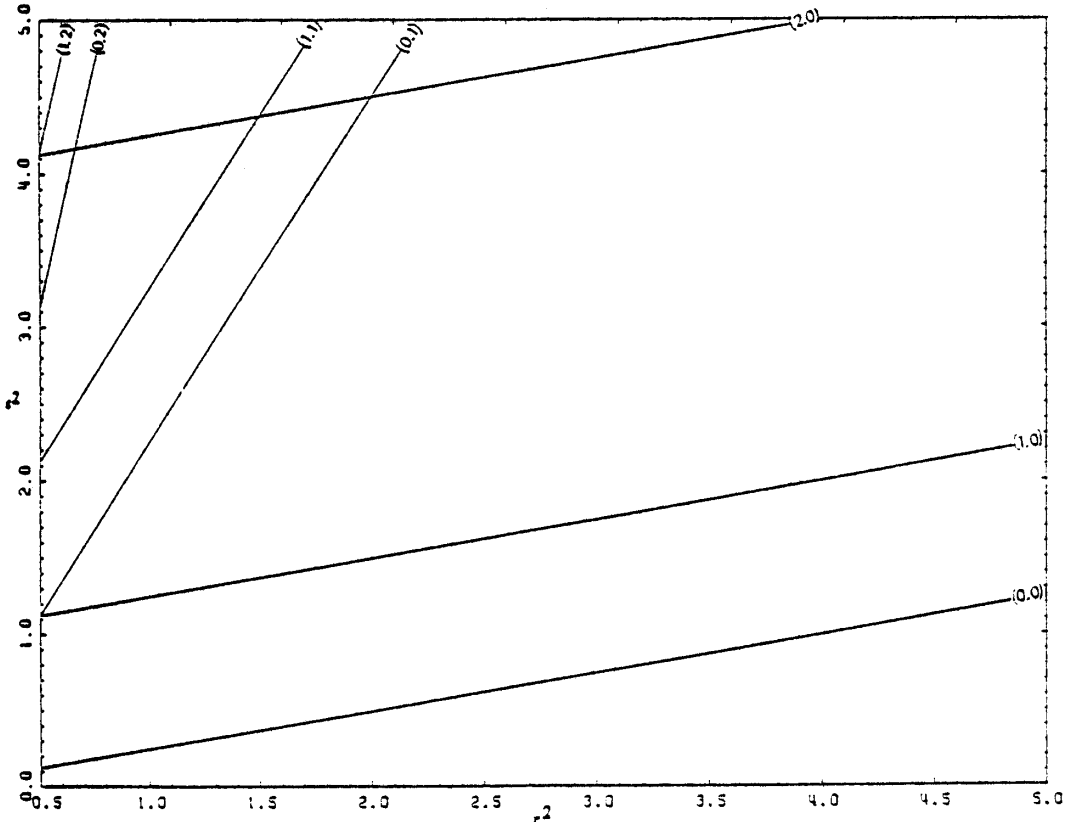


Figure 8. Eigencurves. Rectangular basins, $(c,0)$ and $(0,c)$, $f=0$.

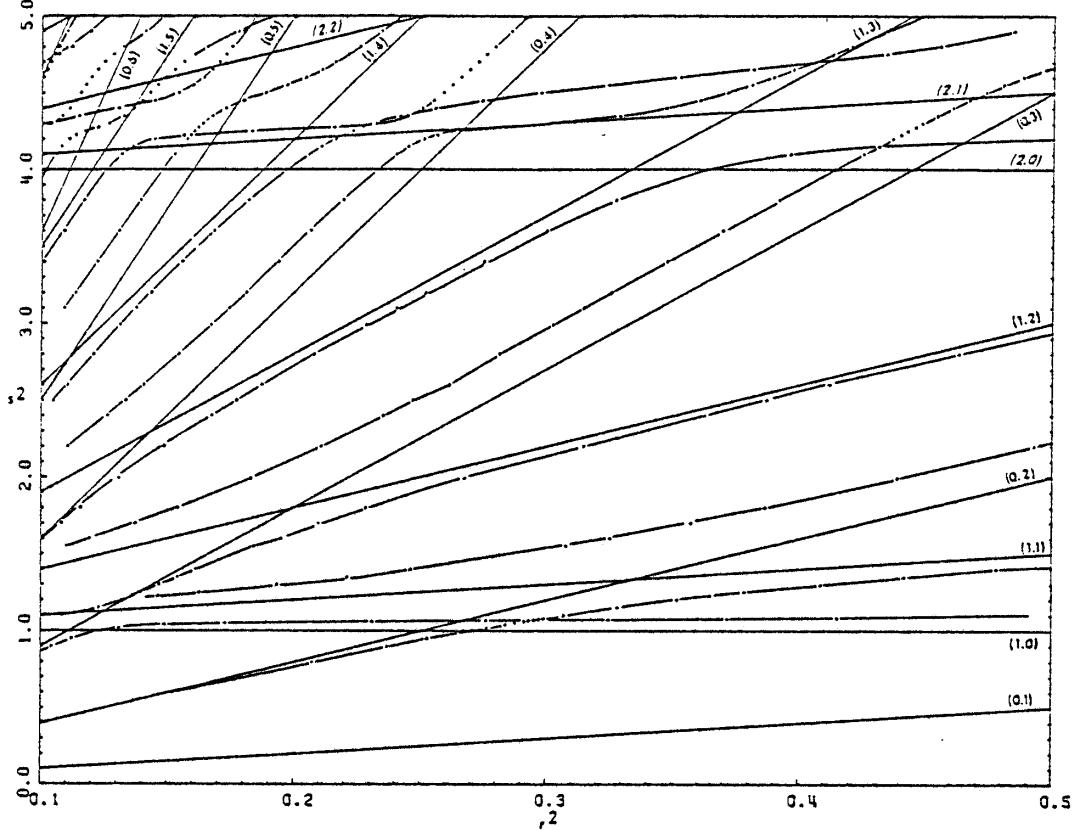


Figure 9. Eigencurves. Rectangular basins, (c, c) , $f=0.25$.

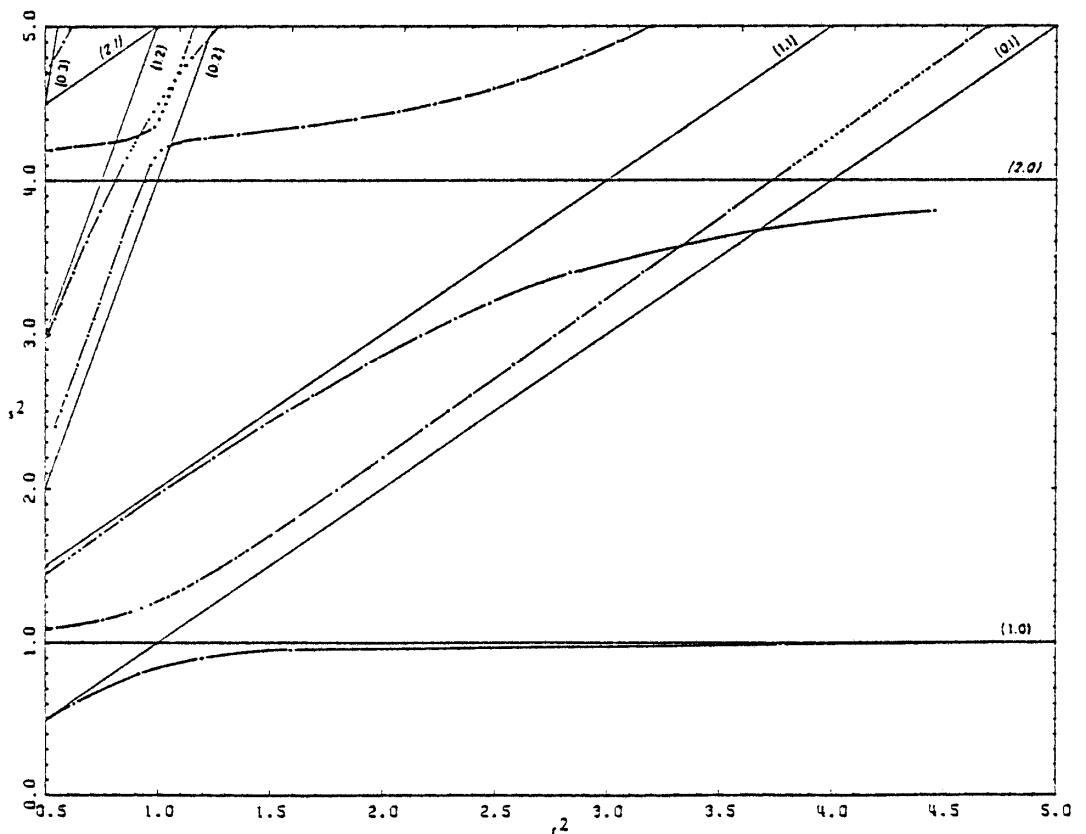


Figure 10. Eigencurves. Rectangular basins, (c, c) , $f=0.25$.

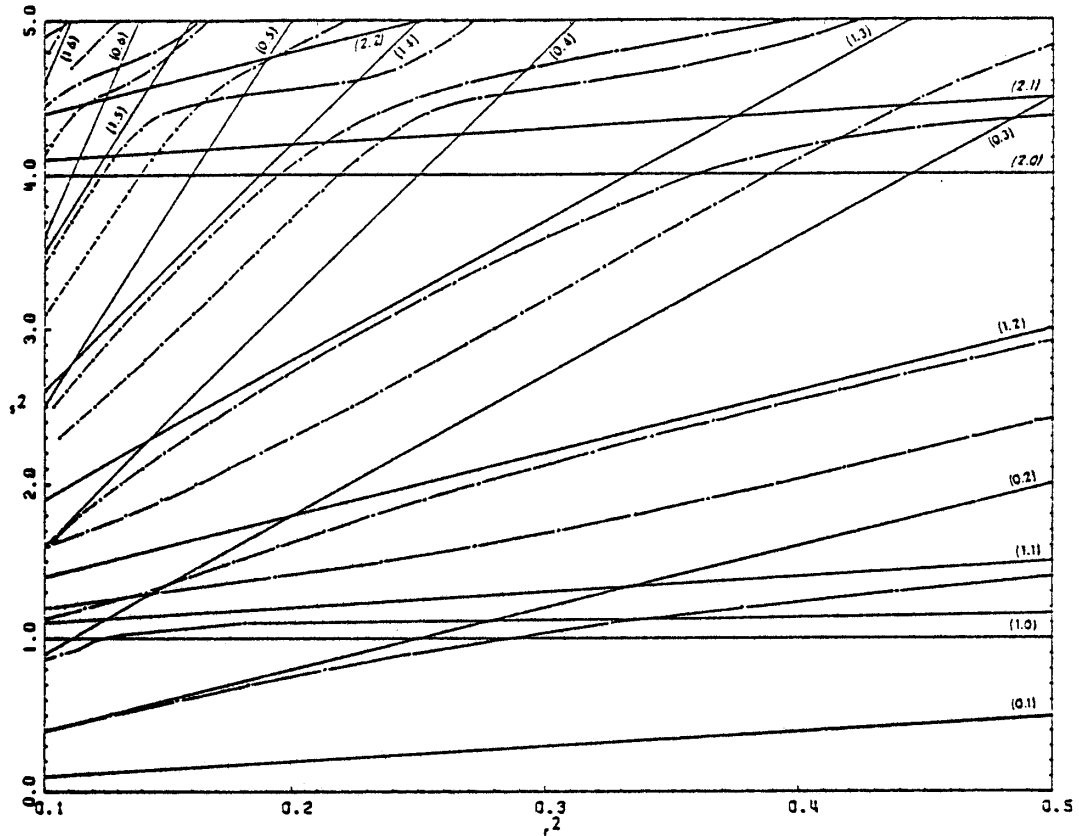


Figure 11. Eigencurves. Rectangular basins, (c, c) , $f=0.35$.

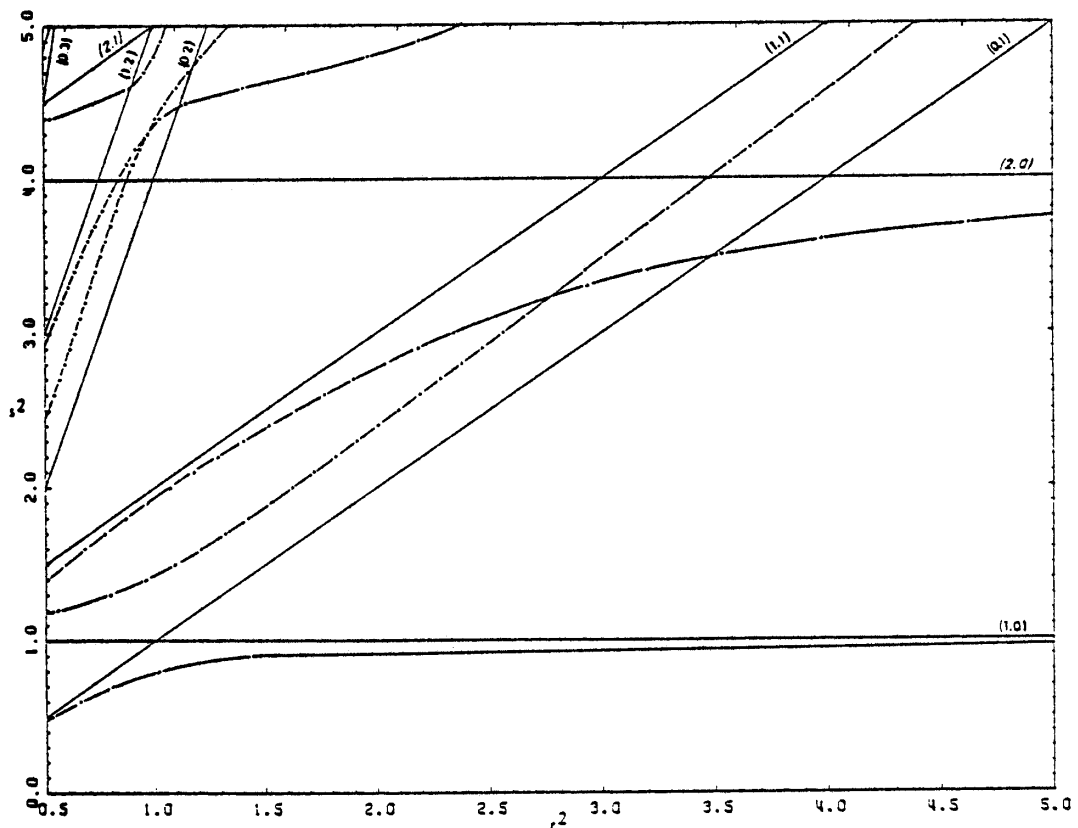


Figure 12. Eigencurves. Rectangular basins, (c, c) , $f=0.35$.

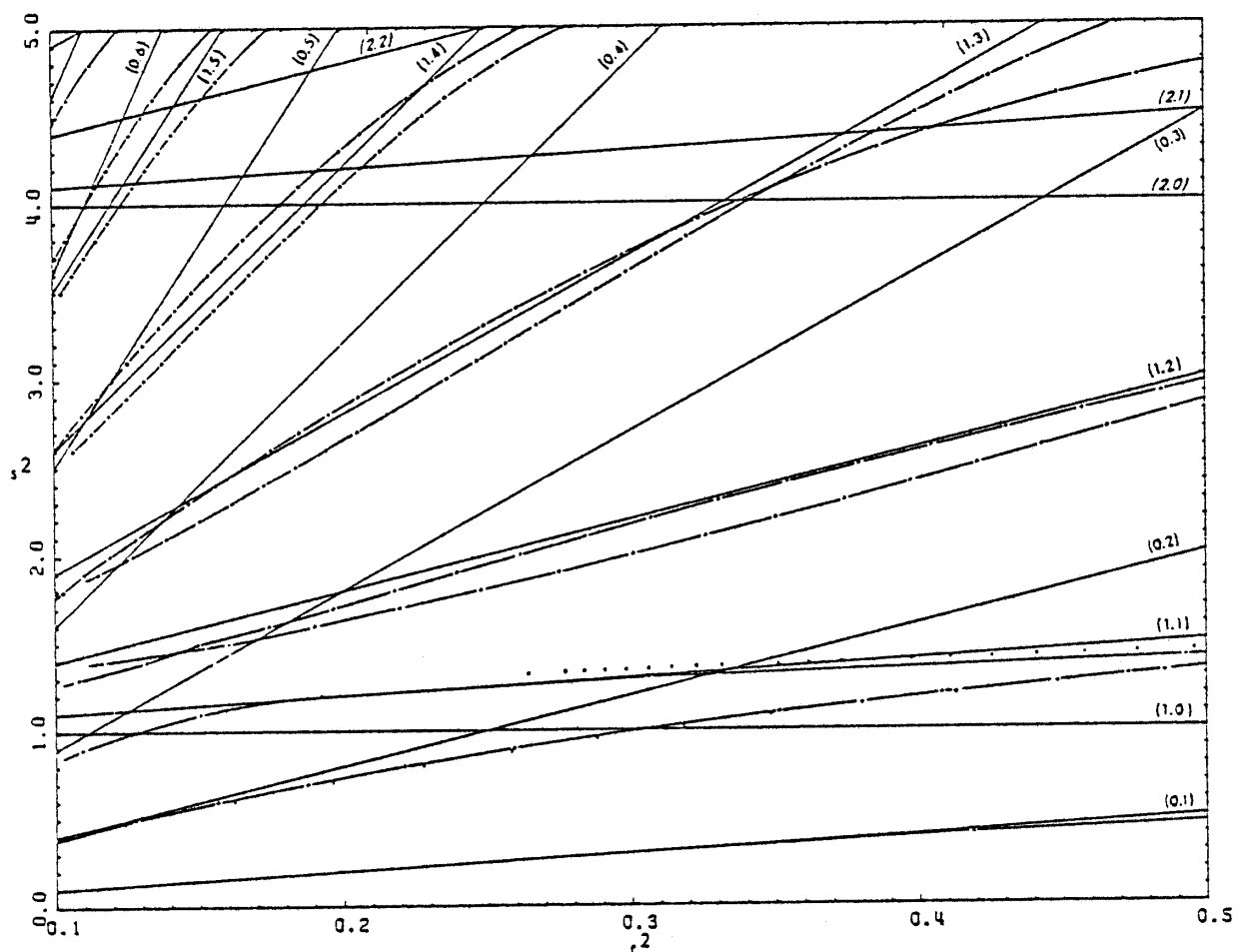


Figure 13. Eigencurves. Rectangular basins, (c, c) , $f=0.5$.

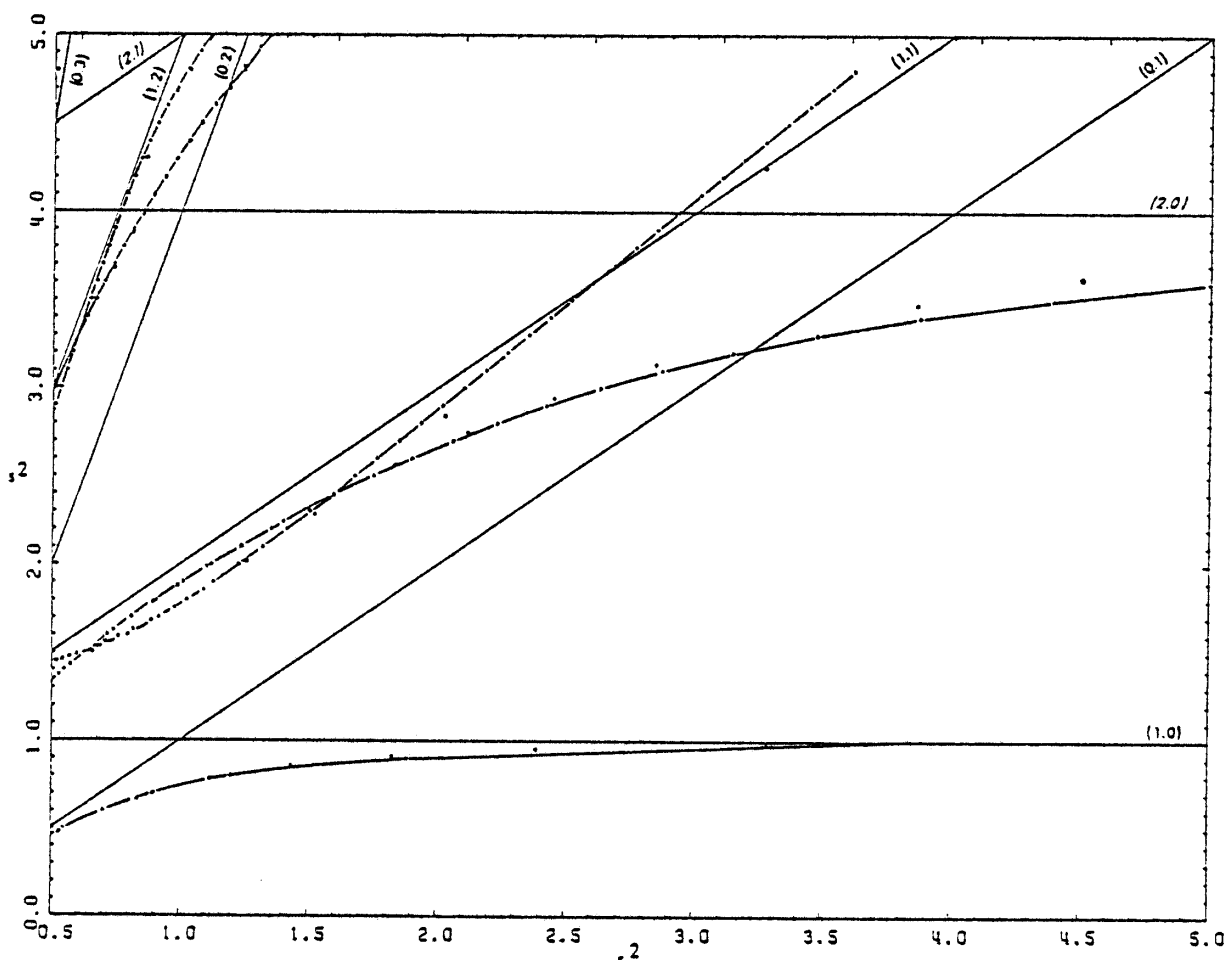


Figure 14. Eigencurves. Rectangular basins, (c,c) , $f=0.5$.

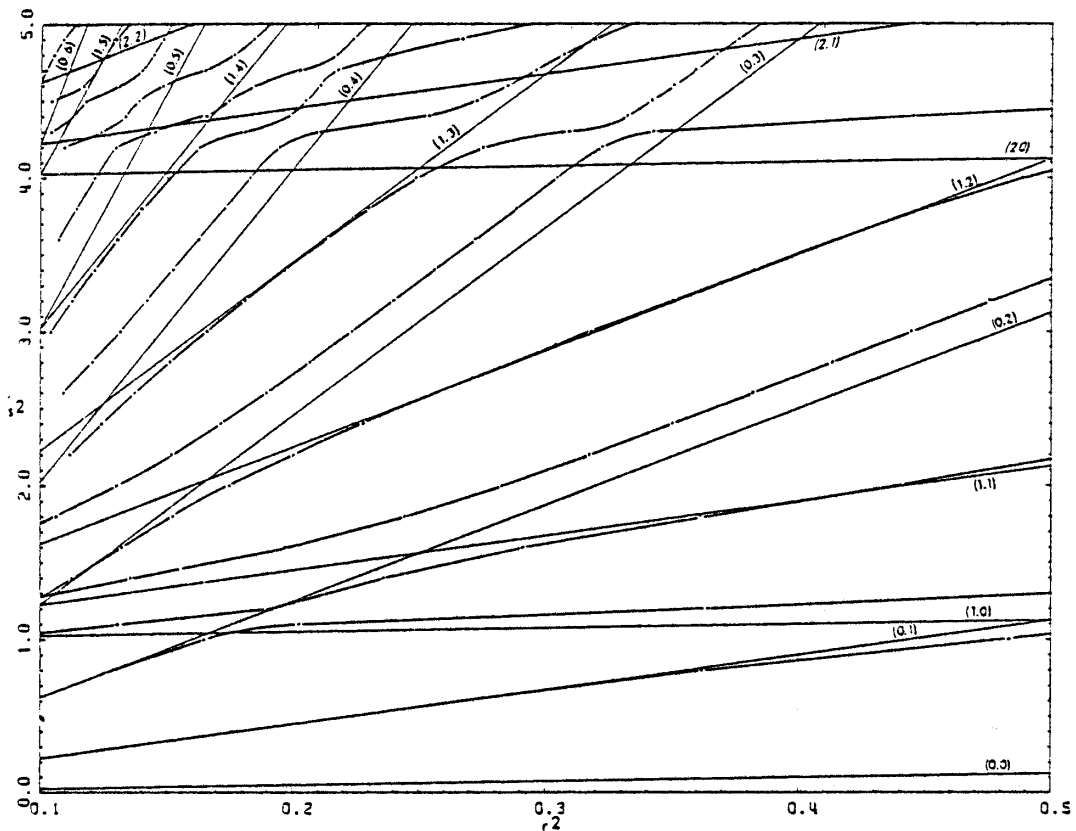


Figure 15. Eigencurves. Rectangular basins, $(c, 0)$. $f=0.25$.

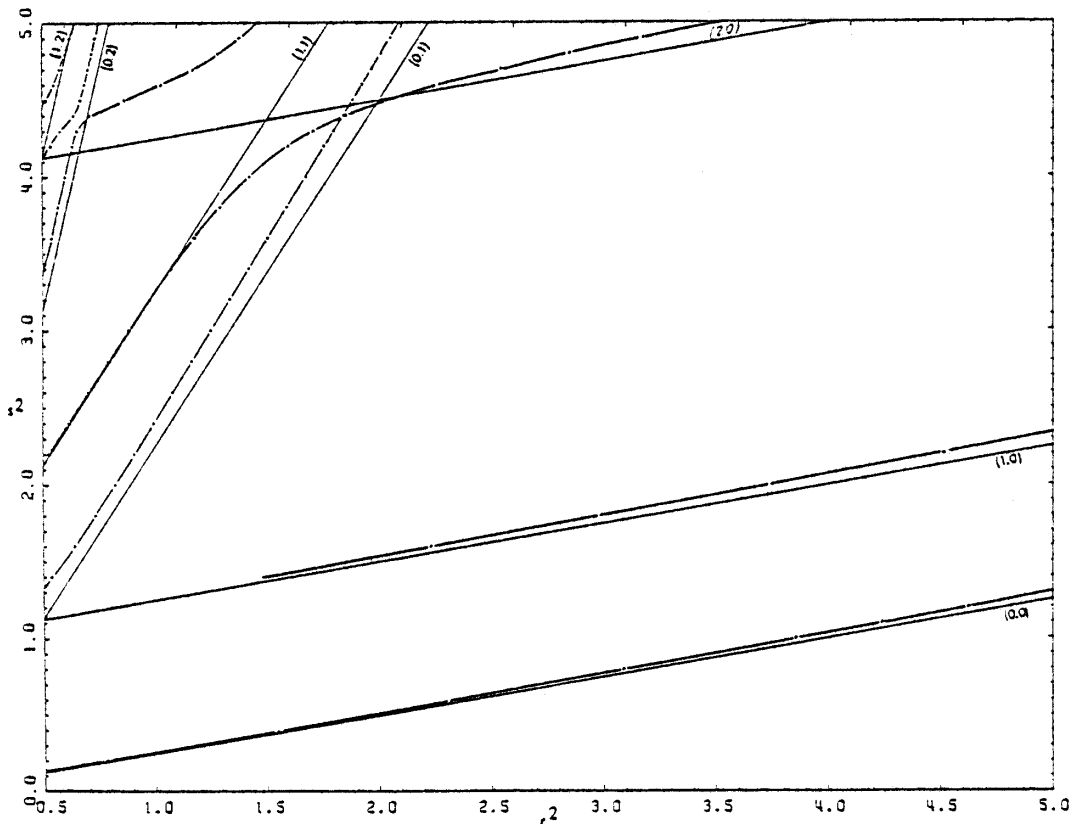


Figure 16. Eigencurves. Rectangular basins, $(c,)$, $f=0.25$.

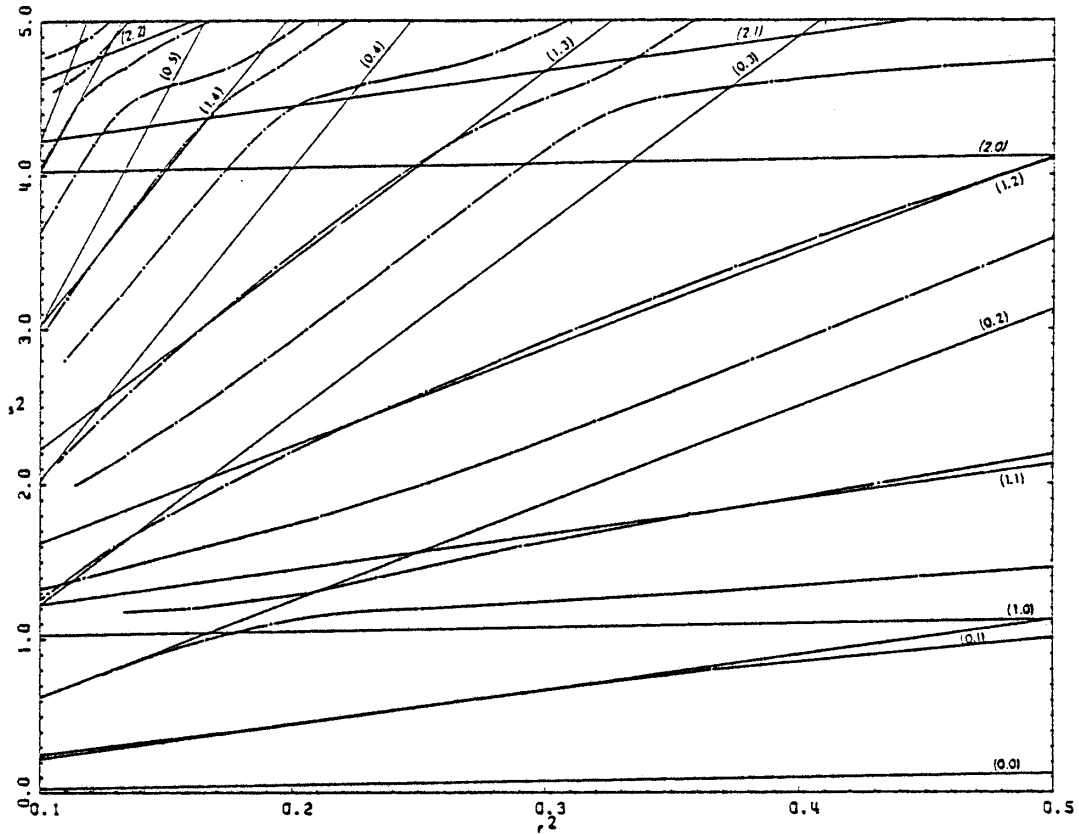


Figure 17. Eigencurves. Rectangular basins, $(c,0)$, $f=0.35$.

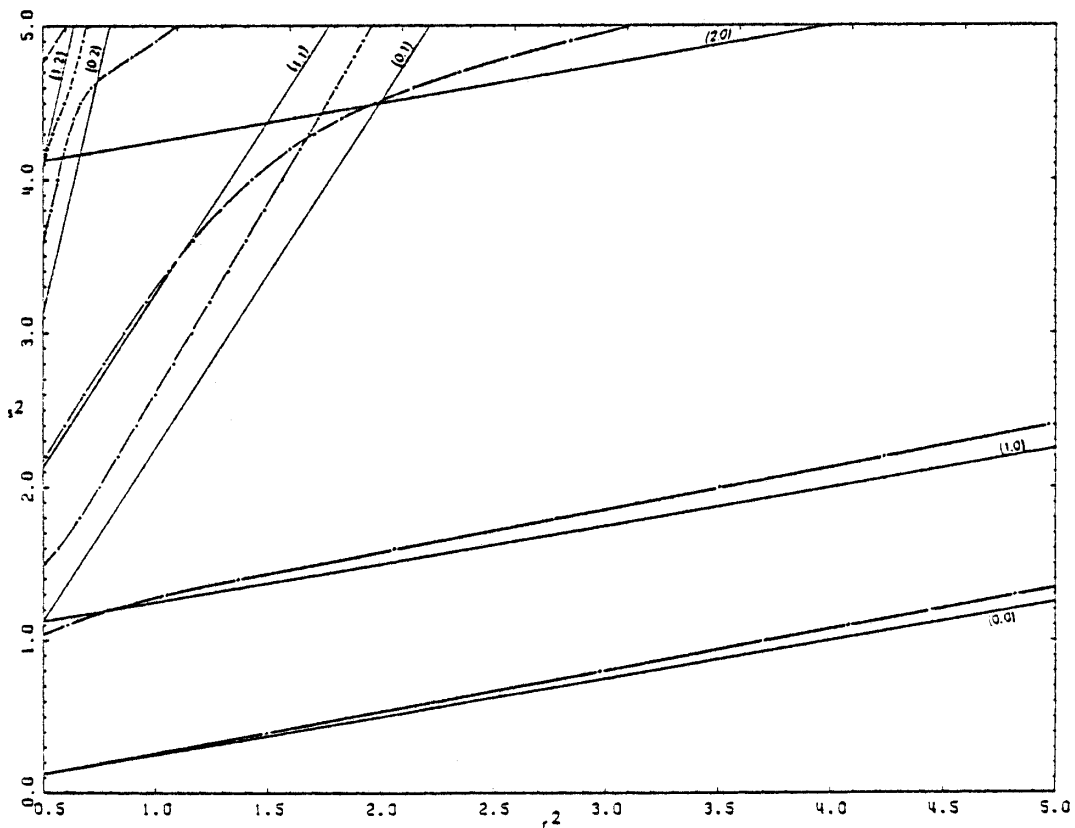


Figure 18. Eigencurves. Rectangular basins, $(c,0)$, $f=0.35$.

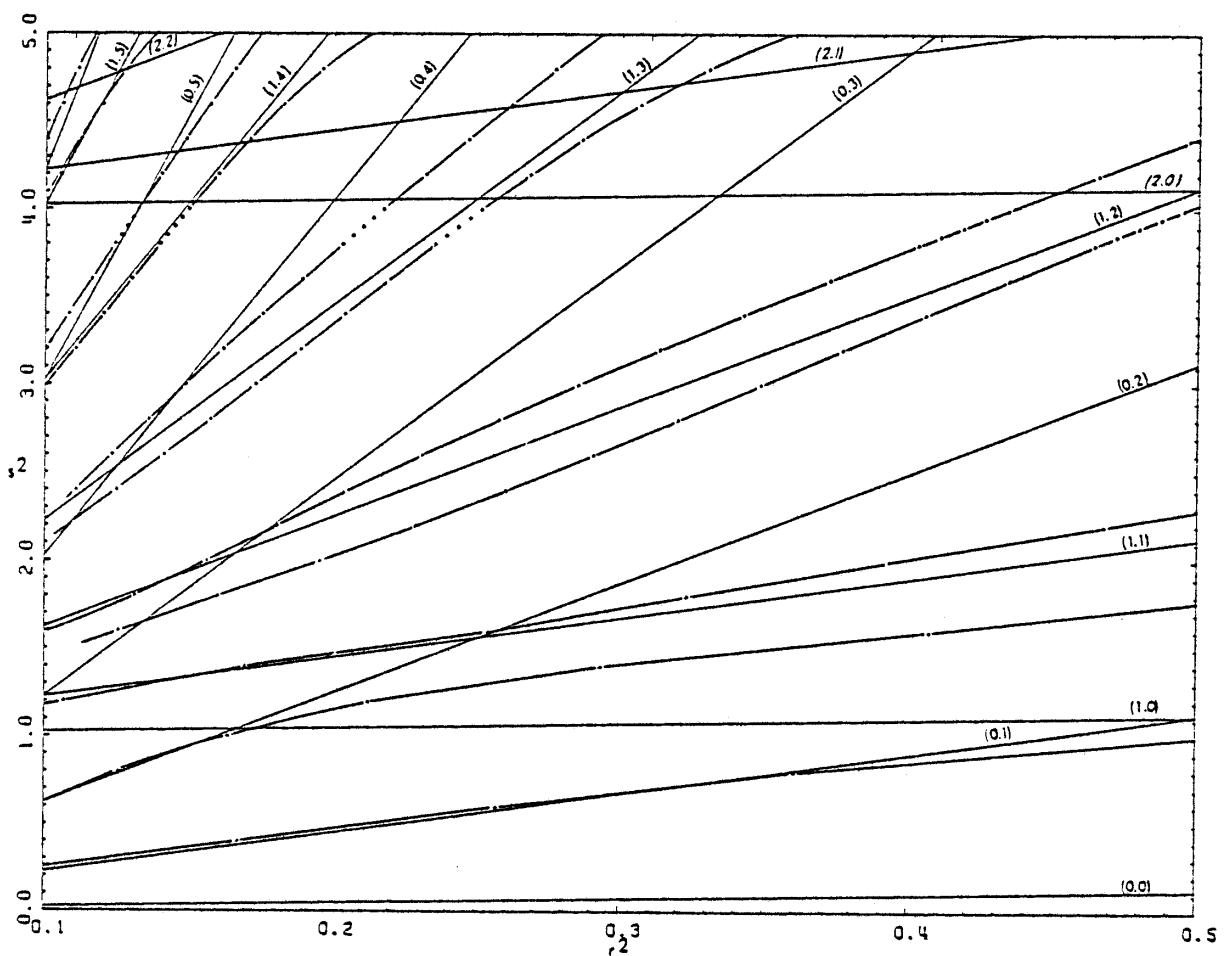


Figure 19. Eigencurves. Rectangular basins, $(c, 0)$, $f=0.5$.

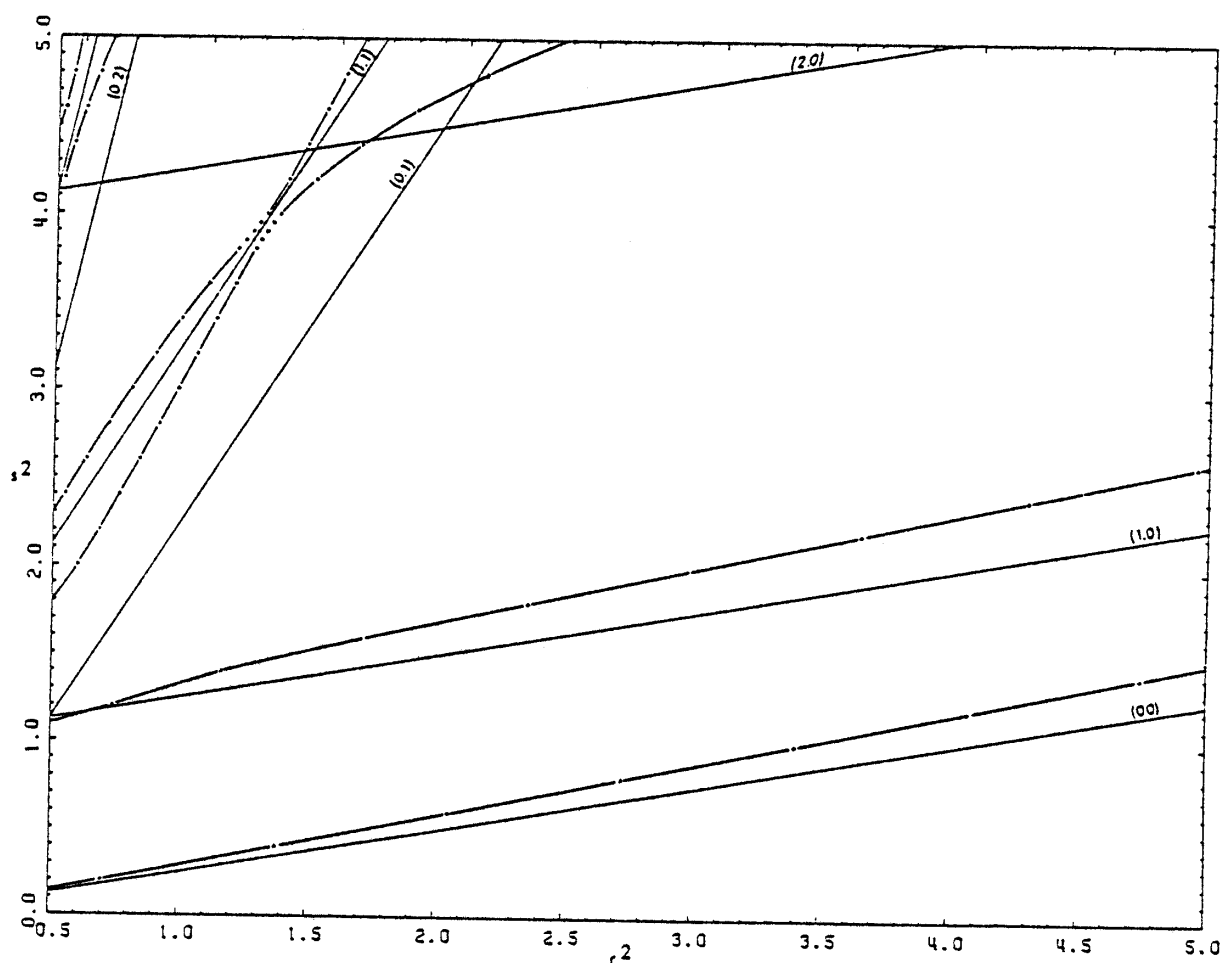


Figure 20. Eigencurves. Rectangular basins, $(c, 0)$, $f=0.5$.

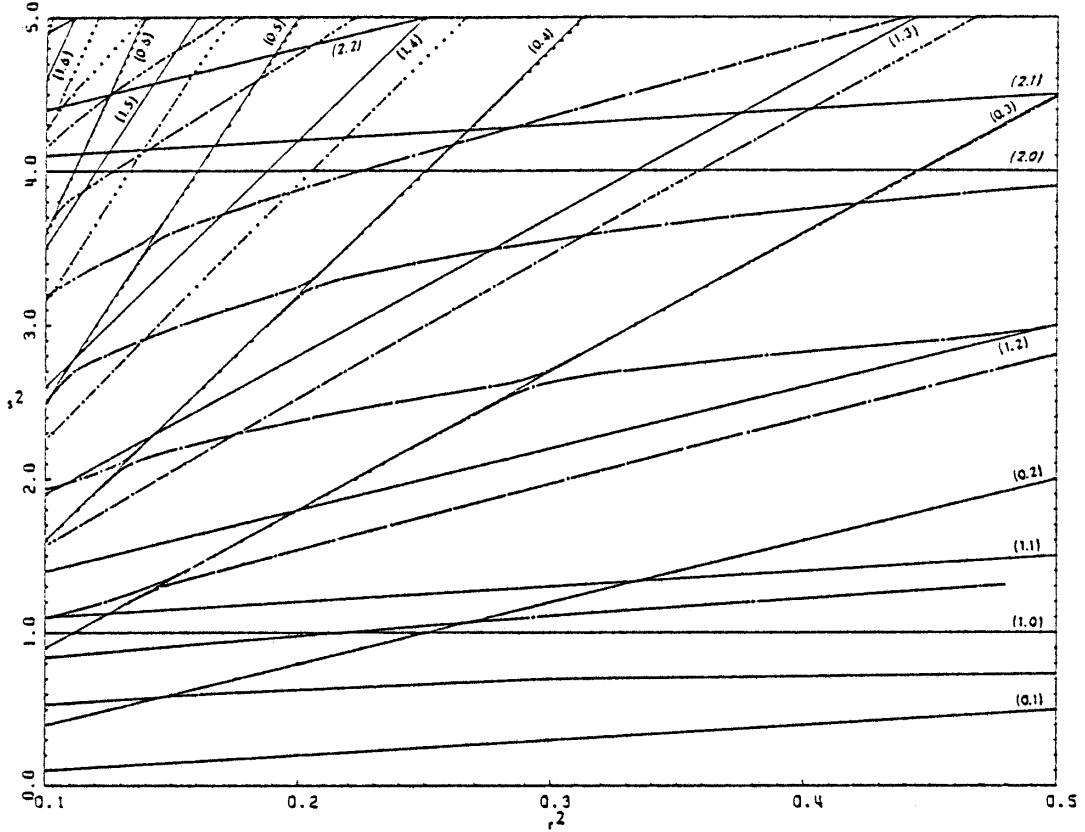


Figure 21. Eigencurves. Trapezoidal basins, (c,c) , $\gamma=2.5^\circ$, $f=0$.

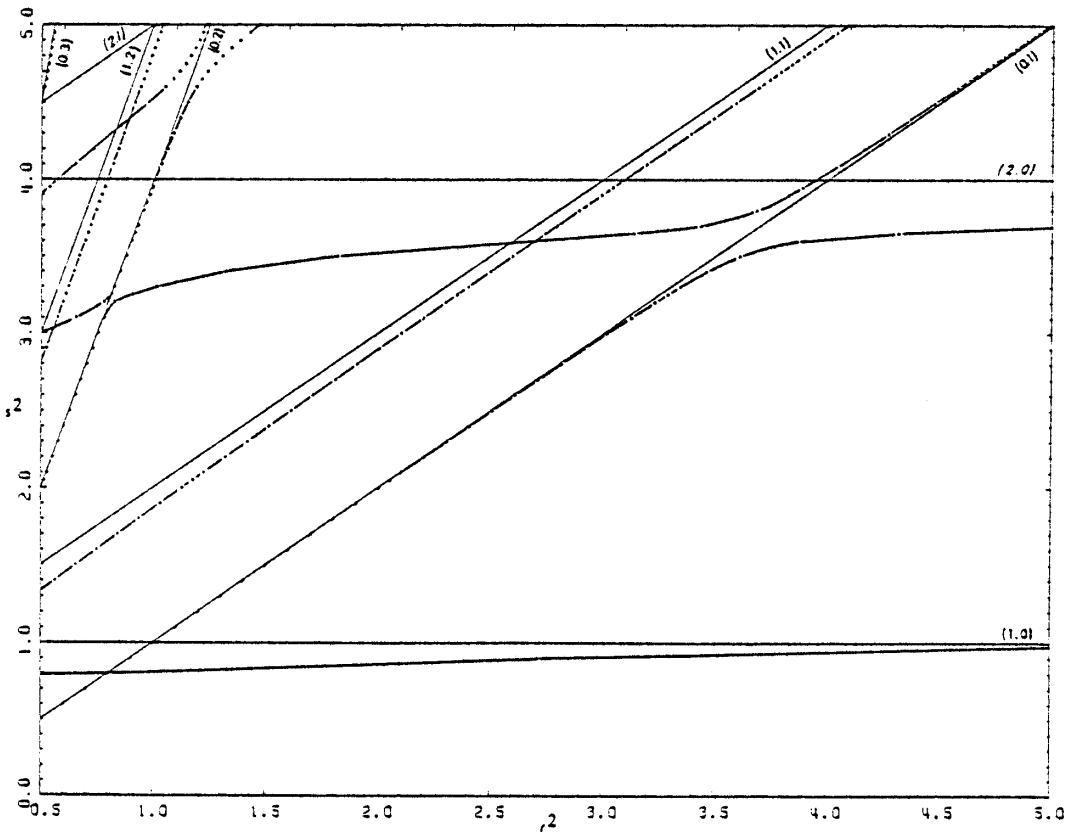


Figure 22. Eigencurves. Trapezoidal basins, (c,c) , $\gamma=2.5^\circ$, $f=0$.

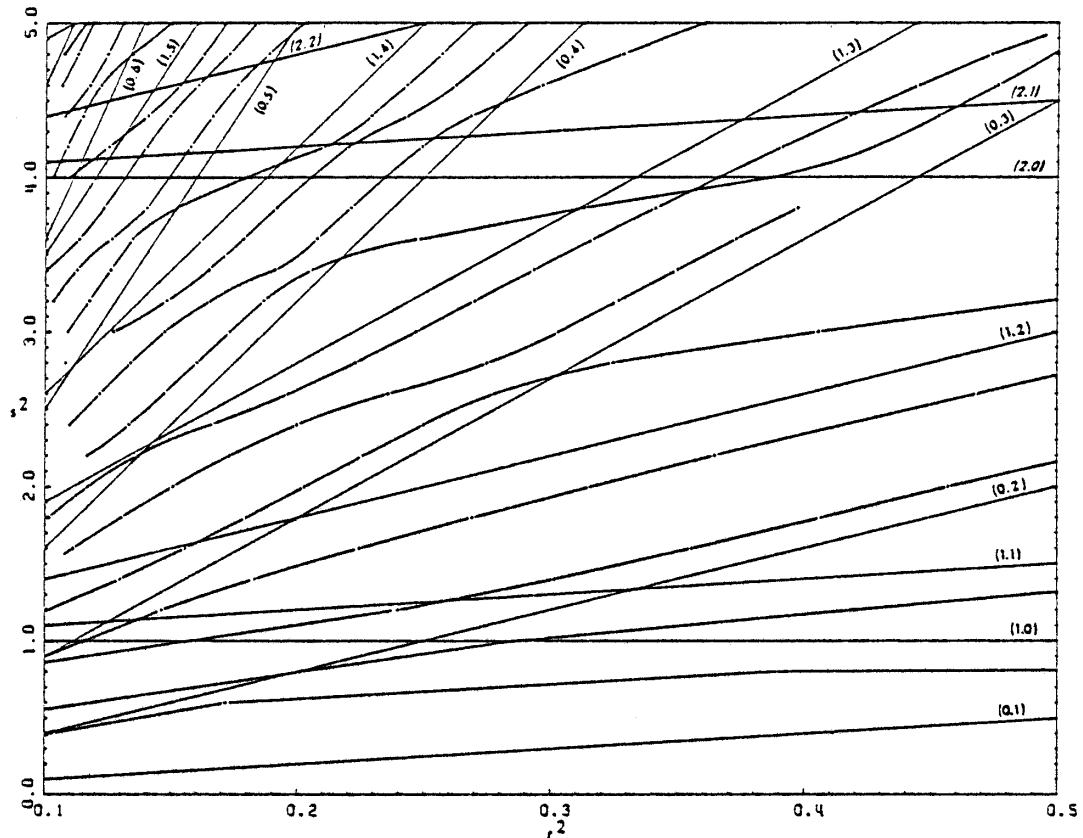


Figure 23. Eigencurves. Trapezoidal basins, (c,c) , $\gamma=2.5^\circ$, $f=0.25$.

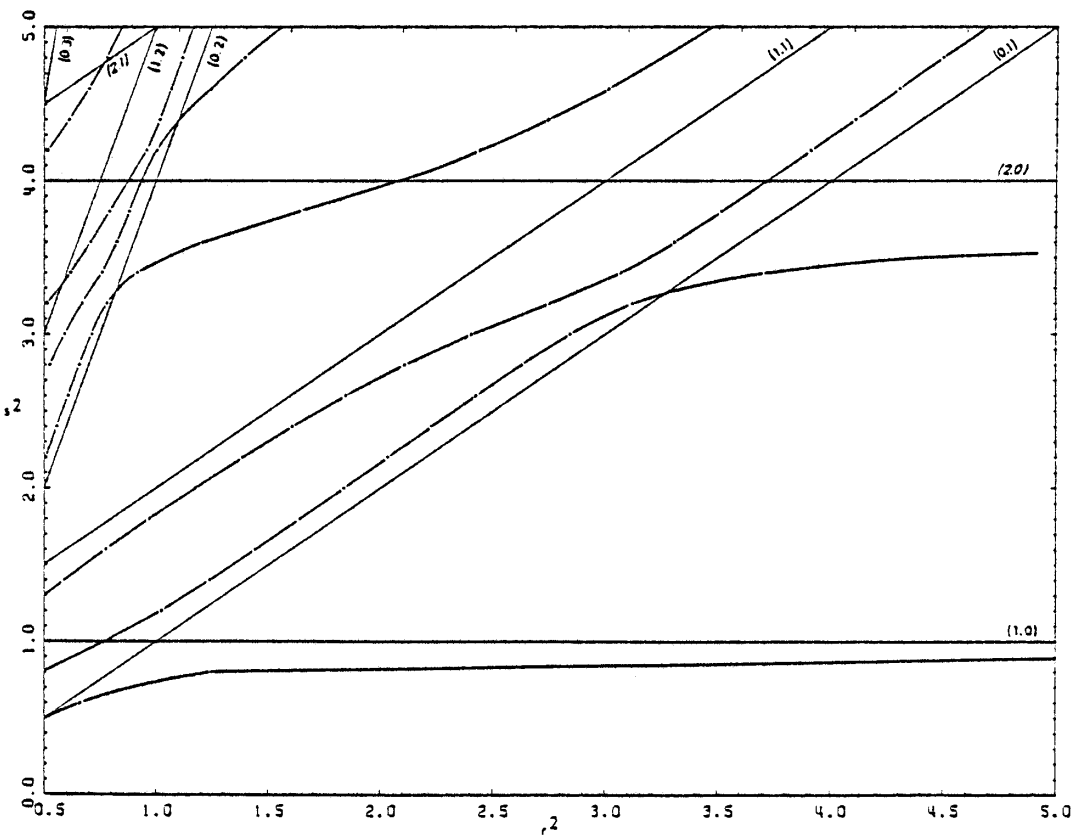


Figure 24. Eigencurves. Trapezoidal basins, (c,c) , $\gamma=2.5^\circ$, $f=0.25$.

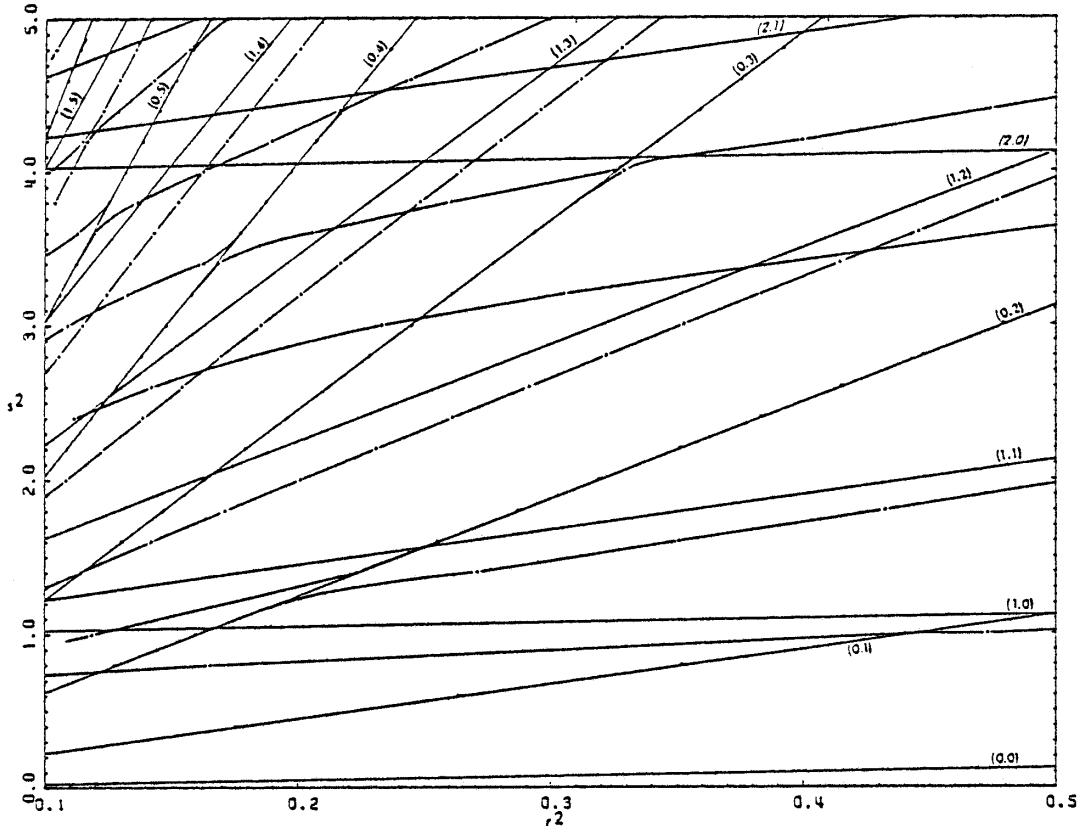


Figure 25. Eigencurves. Trapezoidal basins, $(c, 0)$, $\gamma=2.5^\circ$, $f=0$.

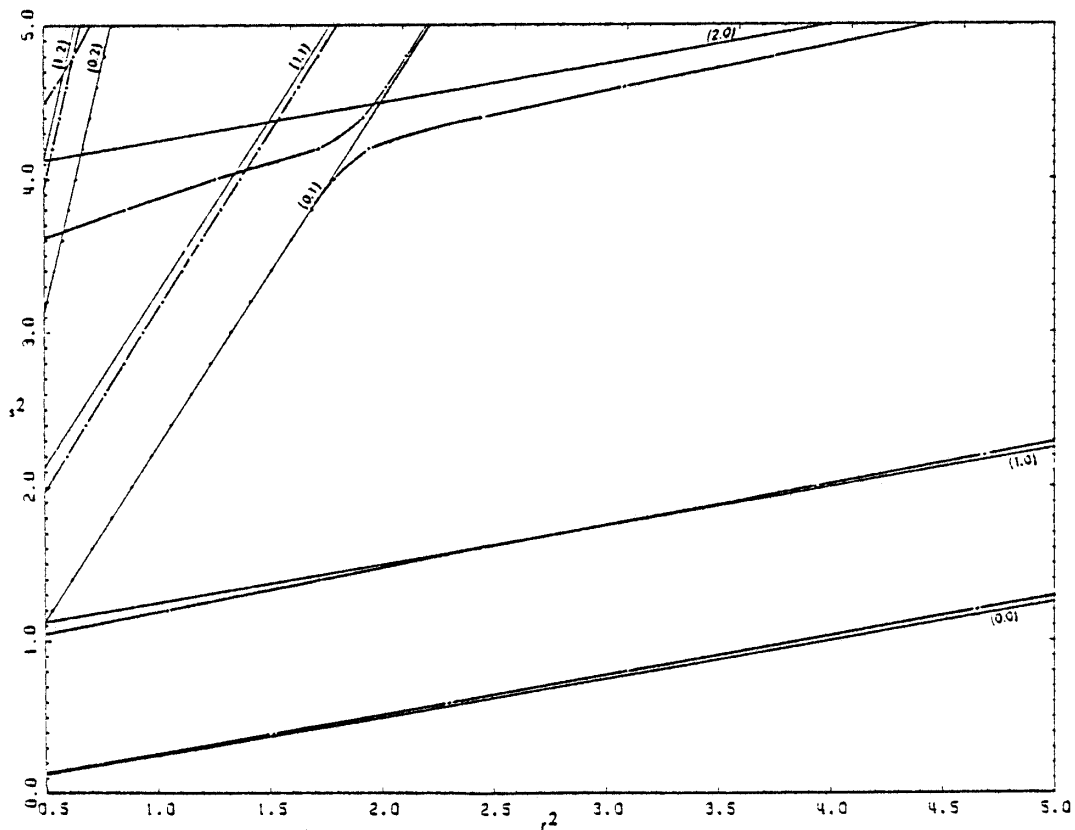


Figure 26. Eigencurves. Trapezoidal basins, $(c, 0)$, $\gamma=2.5^\circ$, $f=0$.

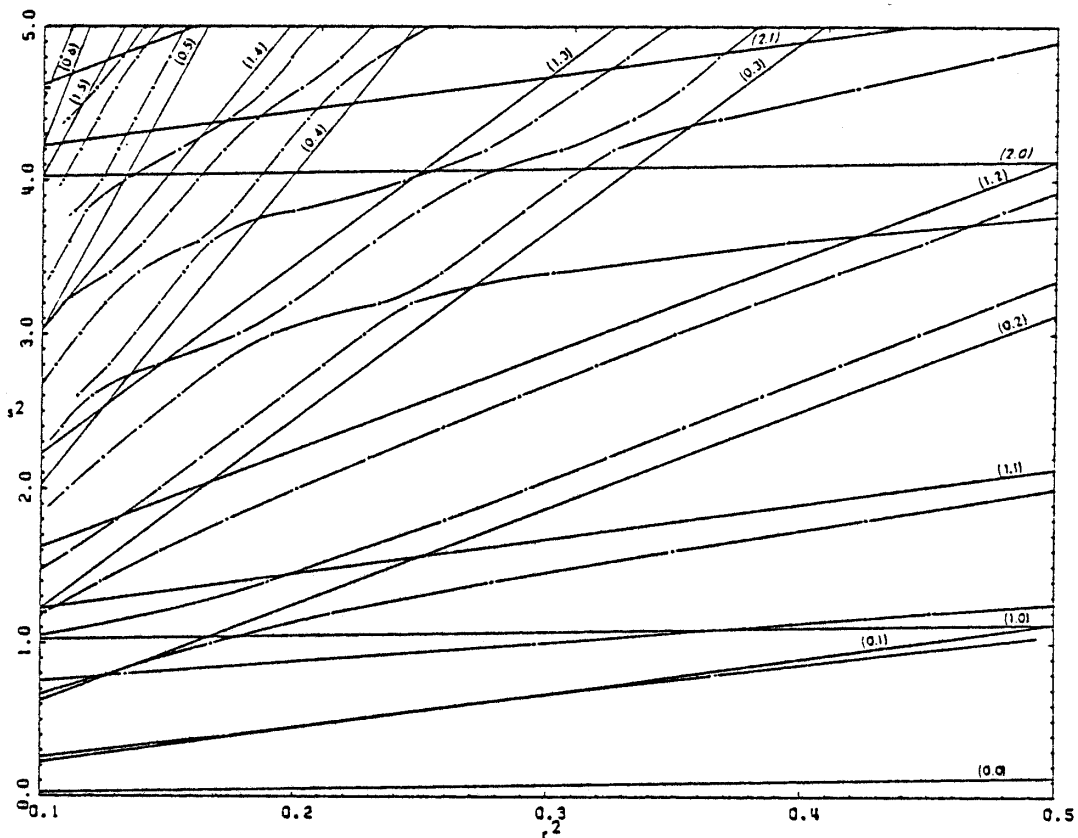


Figure 27. Eigencurves. Trapezoidal basins, $(c, 0)$, $\gamma = 2.5^\circ$, $f = 0.2.5$.

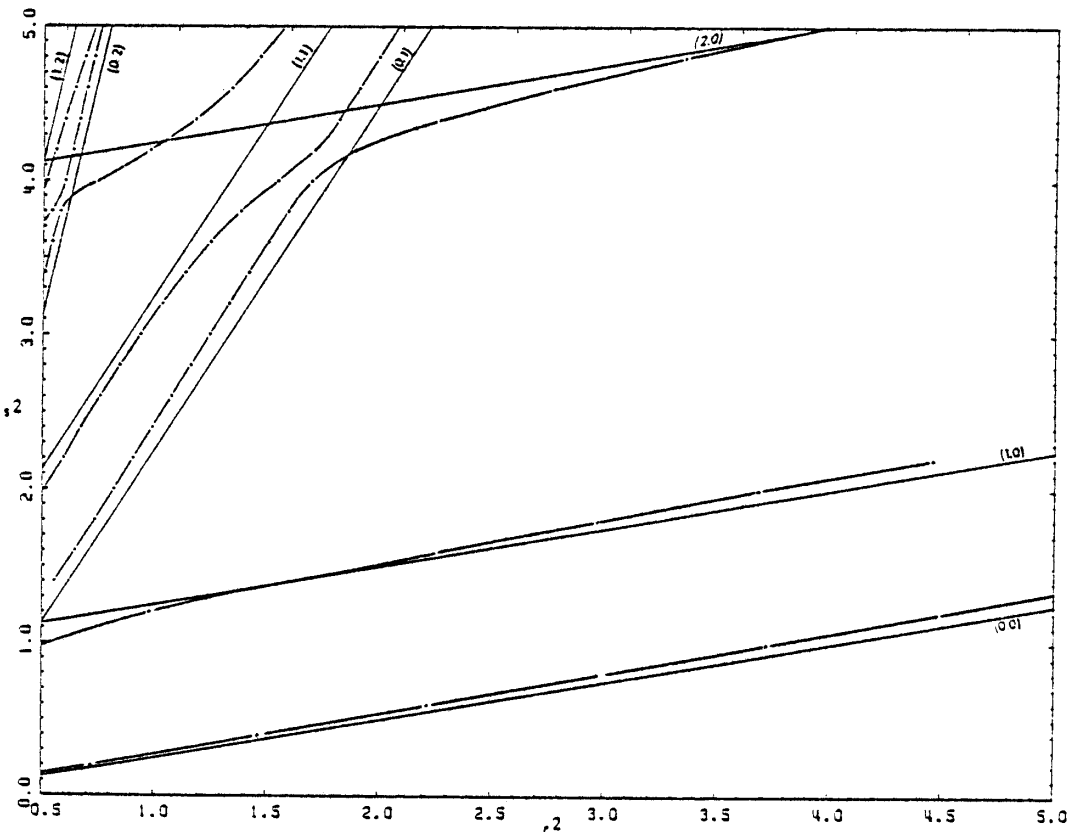


Figure 28. Eigencurves. Trapezoidal basins. $(c,0)$, $\gamma=2.5^\circ$, $f=0.25$.

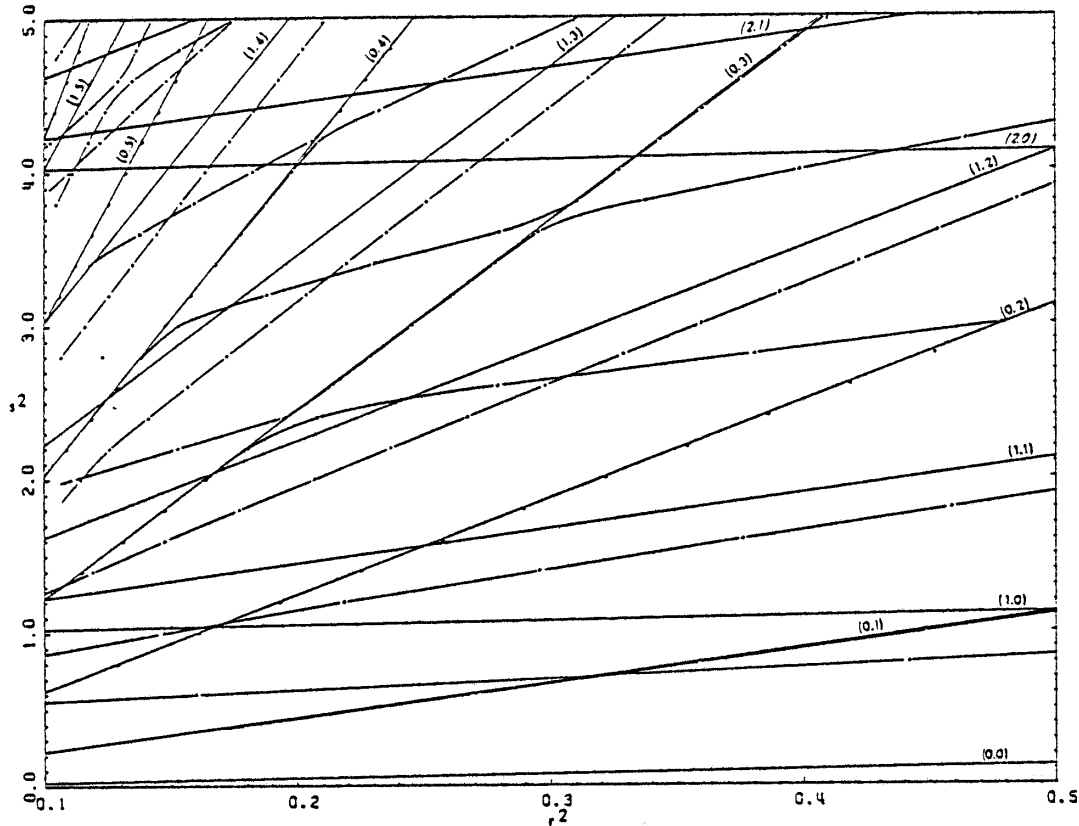


Figure 29. Eigencurves. Trapezoidal basins. $(0,c)$, $\gamma=2.5^\circ$, $f=0$.

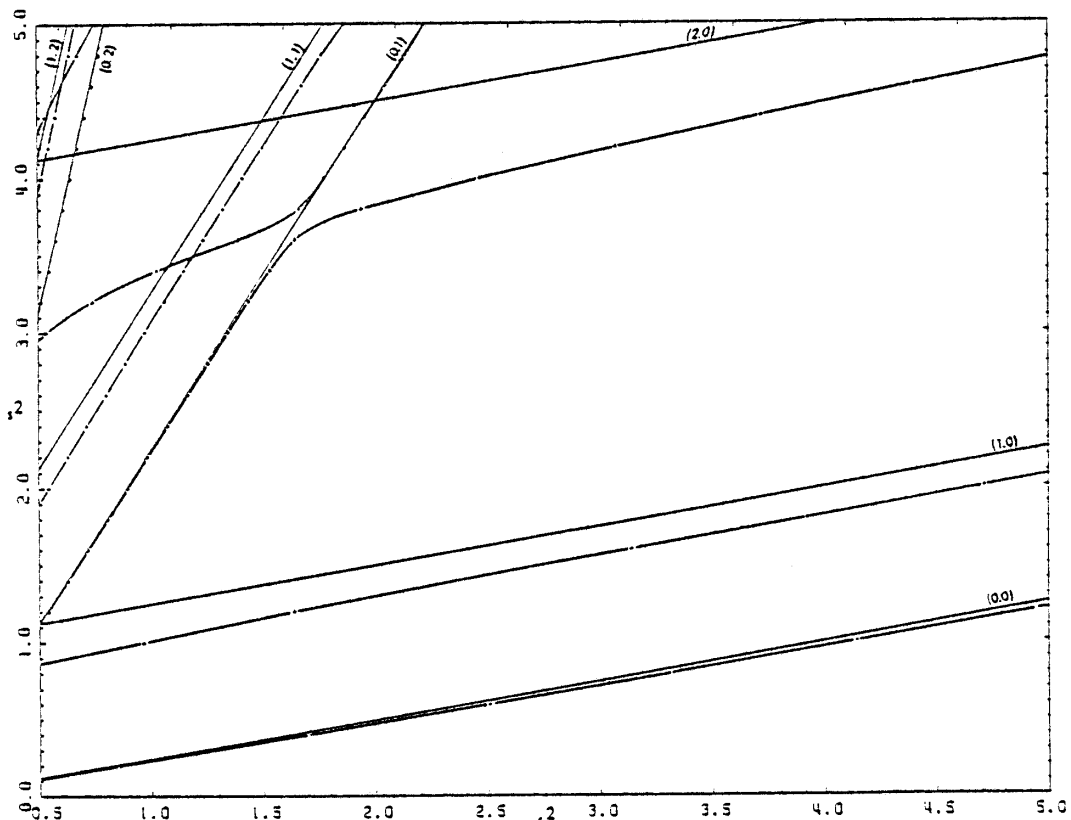


Figure 30. Eigencurves. Trapezoidal basins. $(0,c)$, $\gamma=2.5^\circ$, $f=0$.

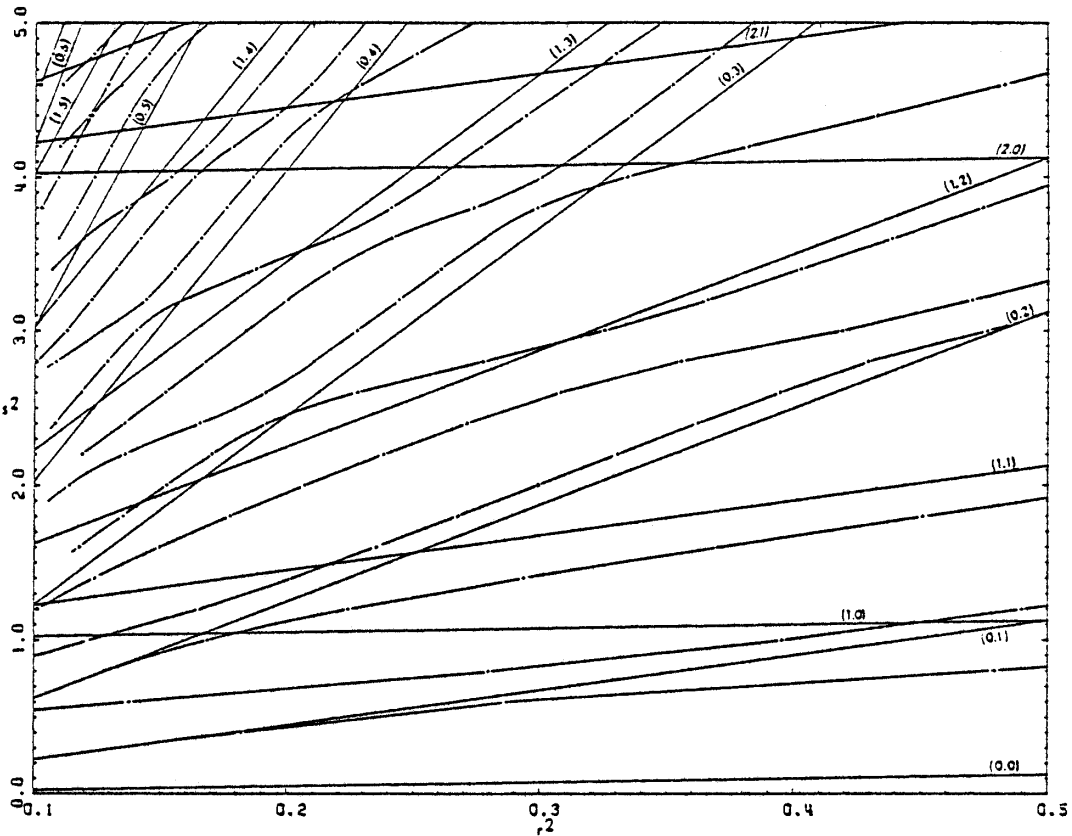


Figure 31. Eigencurves. Trapezoidal basins. $(0,c)$, $\gamma=2.5^\circ$, $f=0.25$.

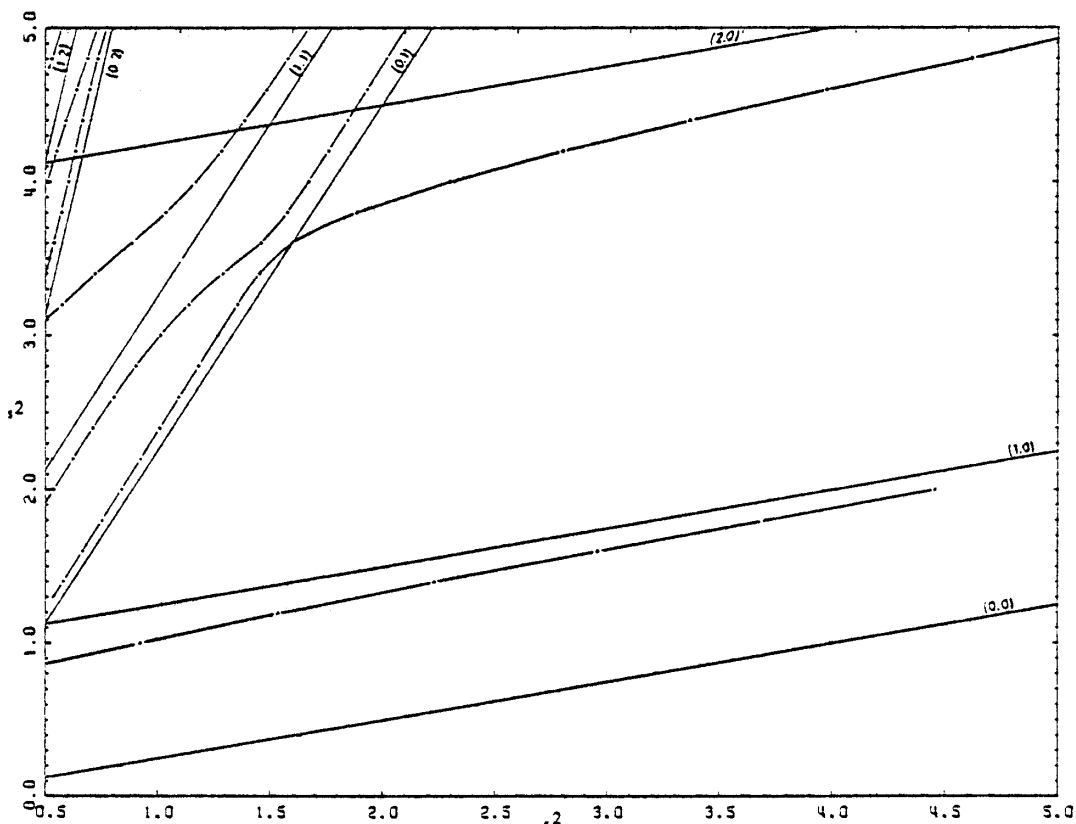


Figure 32. Eigencurves. Trapezoidal basins. $(0,c)$, $\gamma=2.5^\circ$, $f=0.25$.

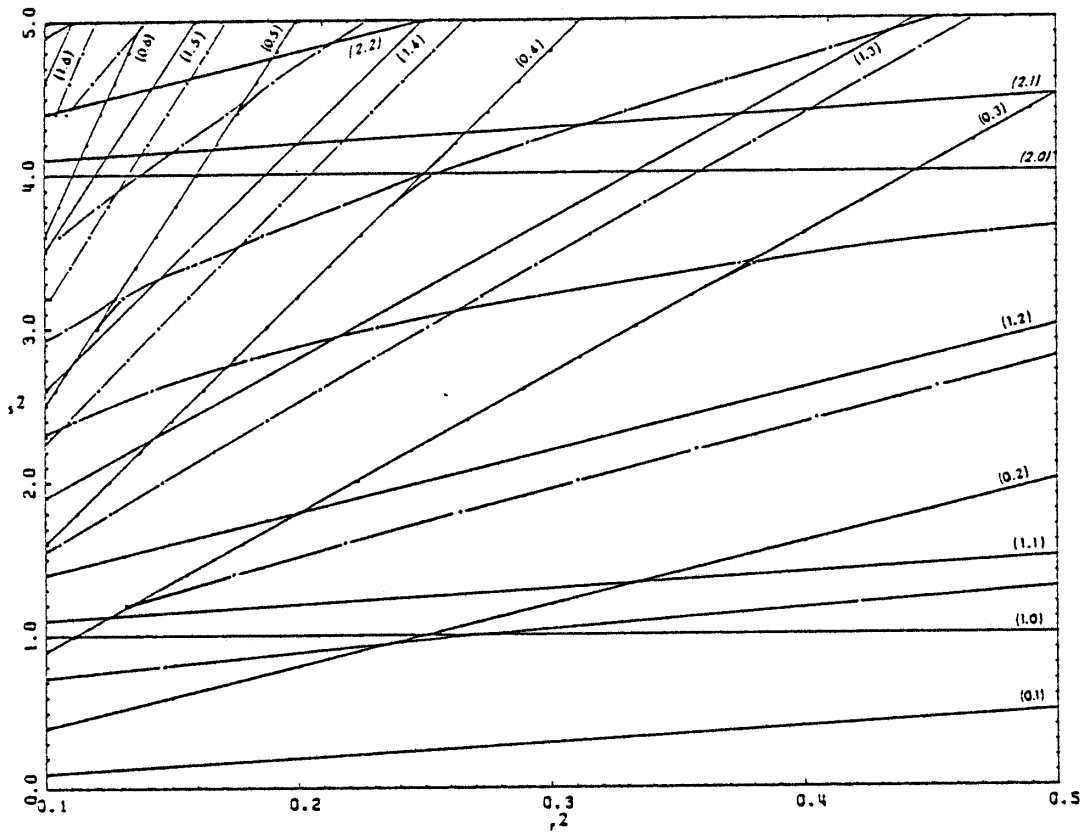


Figure 33. Eigencurves. Trapezoidal basins. $(0,0)$. $\gamma=2.5^\circ$, $f=0$.

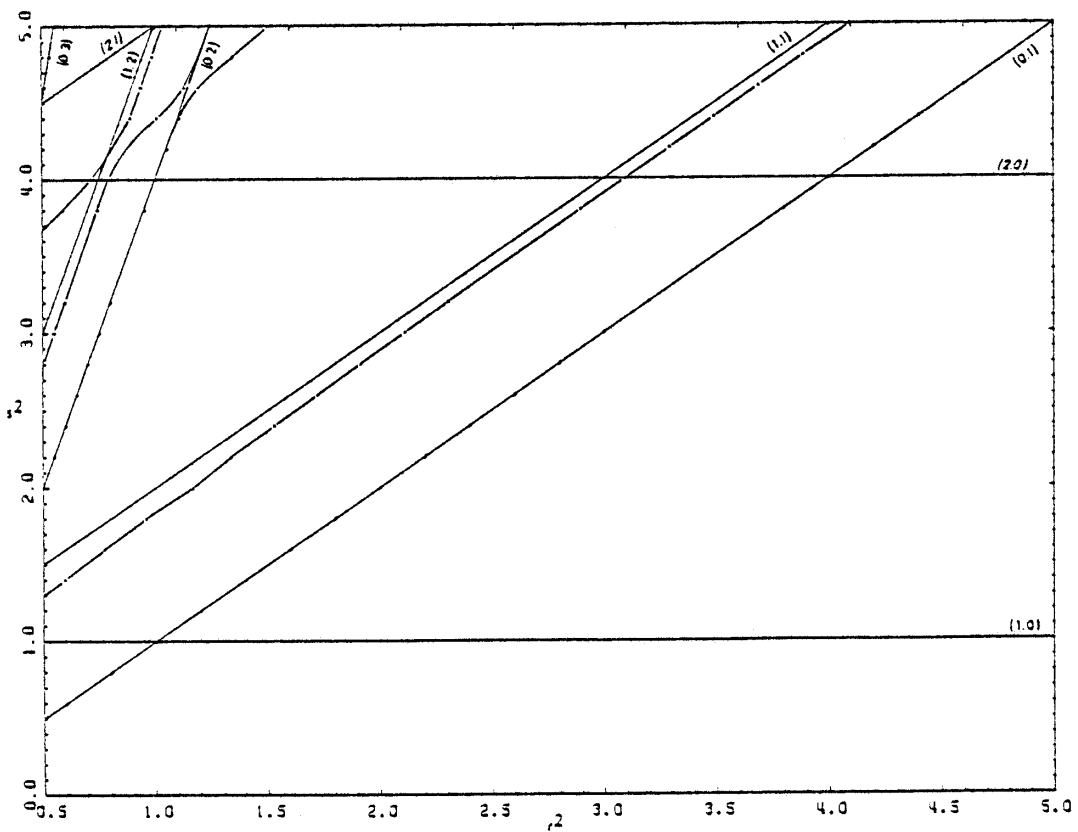


Figure 34. Eigencurves. Trapezoidal basins. $(0,0)$, $\gamma=2.5^\circ$, $f=0$.

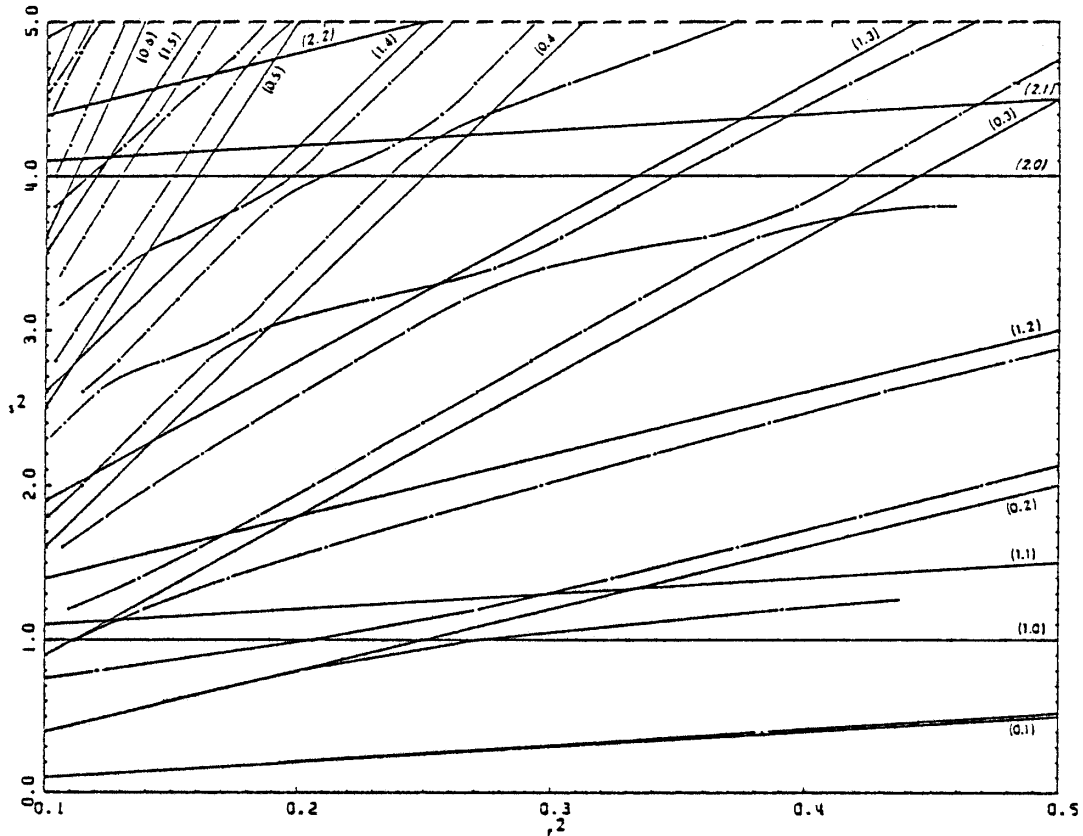


Figure 35. Eigencurves. Trapezoidal basins. (0.0), $\gamma=2.5^\circ$, $f=0.25$.

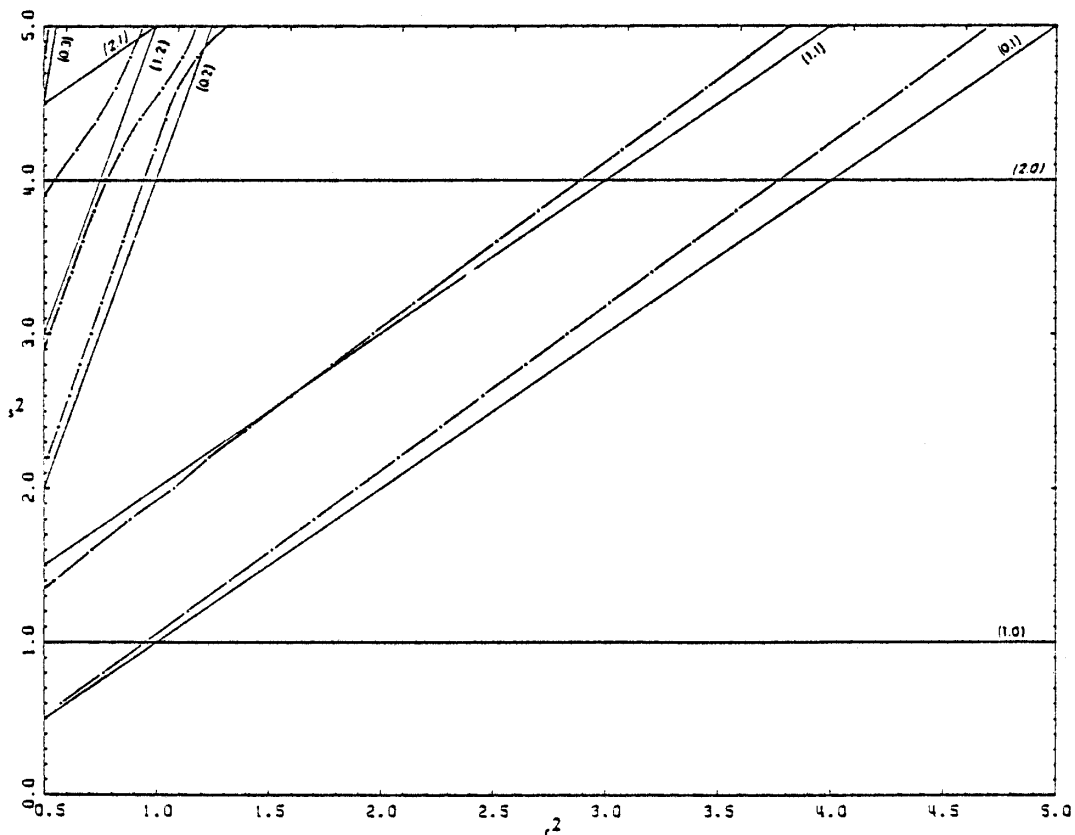


Figure 36. Eigencurves. Trapezoidal basins. (0.0), $\gamma=2.5^\circ$, $f=0.25$.

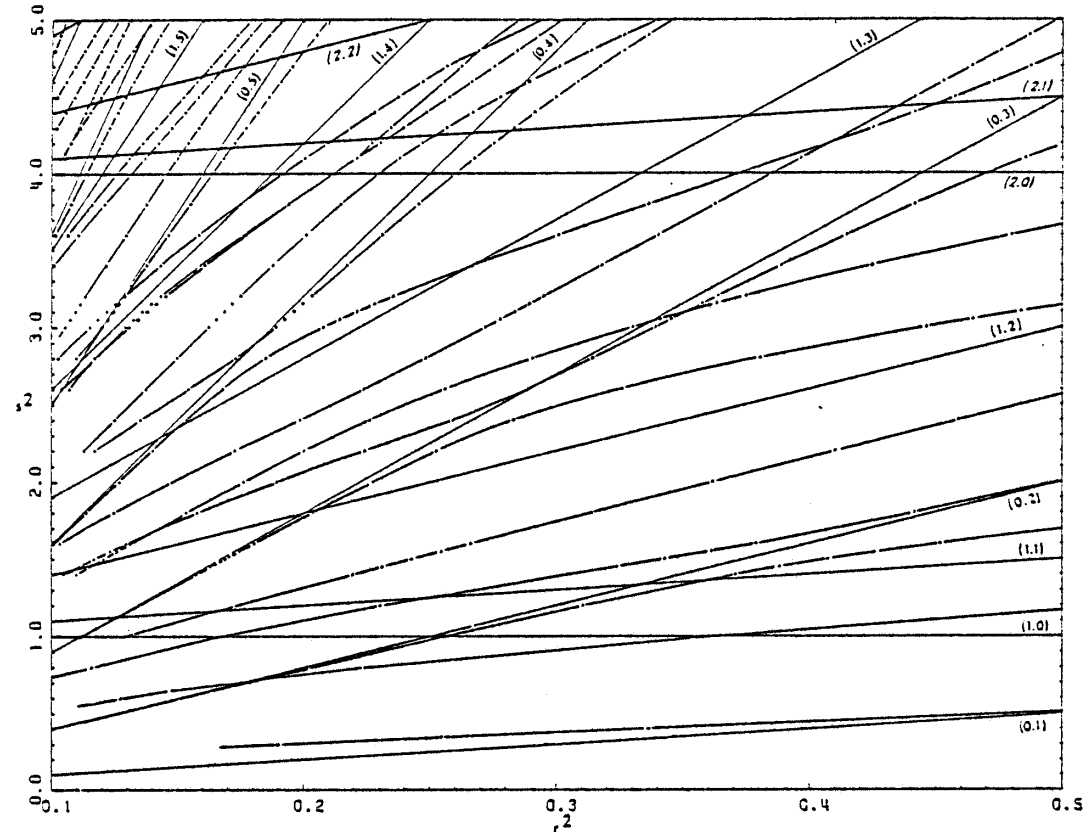


Figure 37. Eigencurves. Trapezoidal basins. (c,c) , $\gamma=7.5^\circ$, $f=0$.

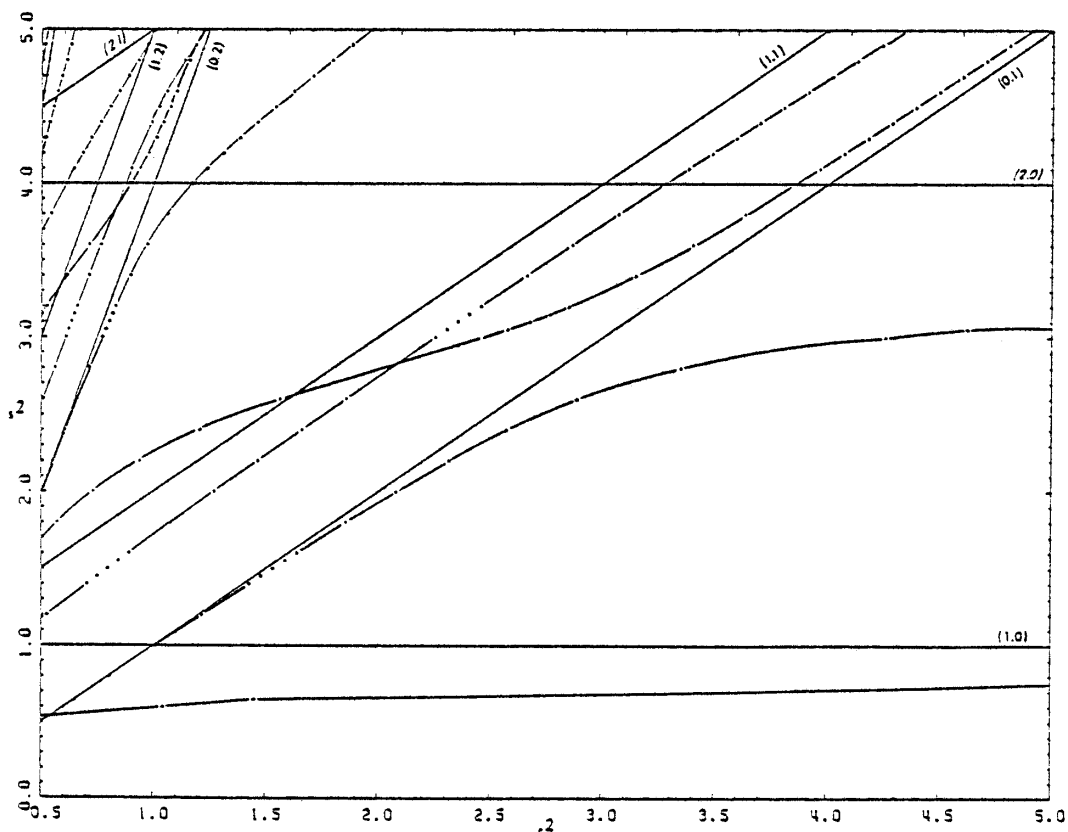


Figure 38. Eigencurves. Trapezoidal basins. (c,c) , $\gamma=7.5^\circ$, $f=0$.

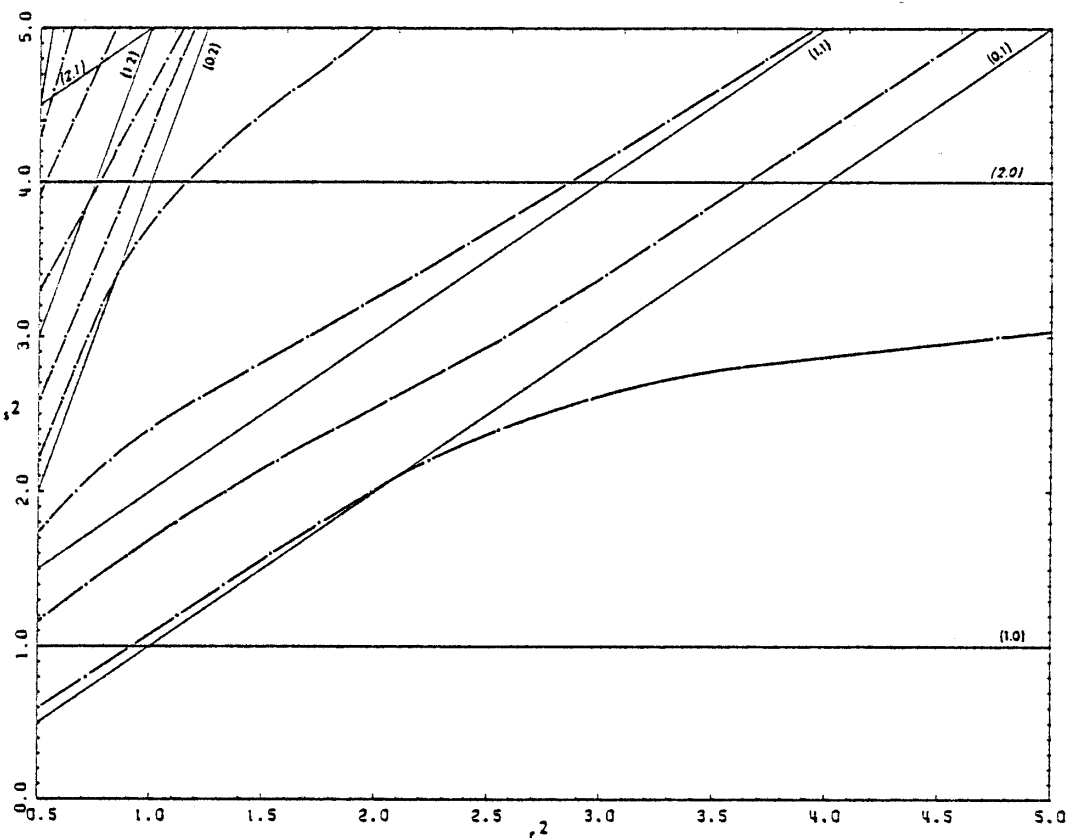


Figure 39. Eigencurves. Trapezoidal basins. (c,c) , $\gamma=7.5^\circ$, $f=0.25$.

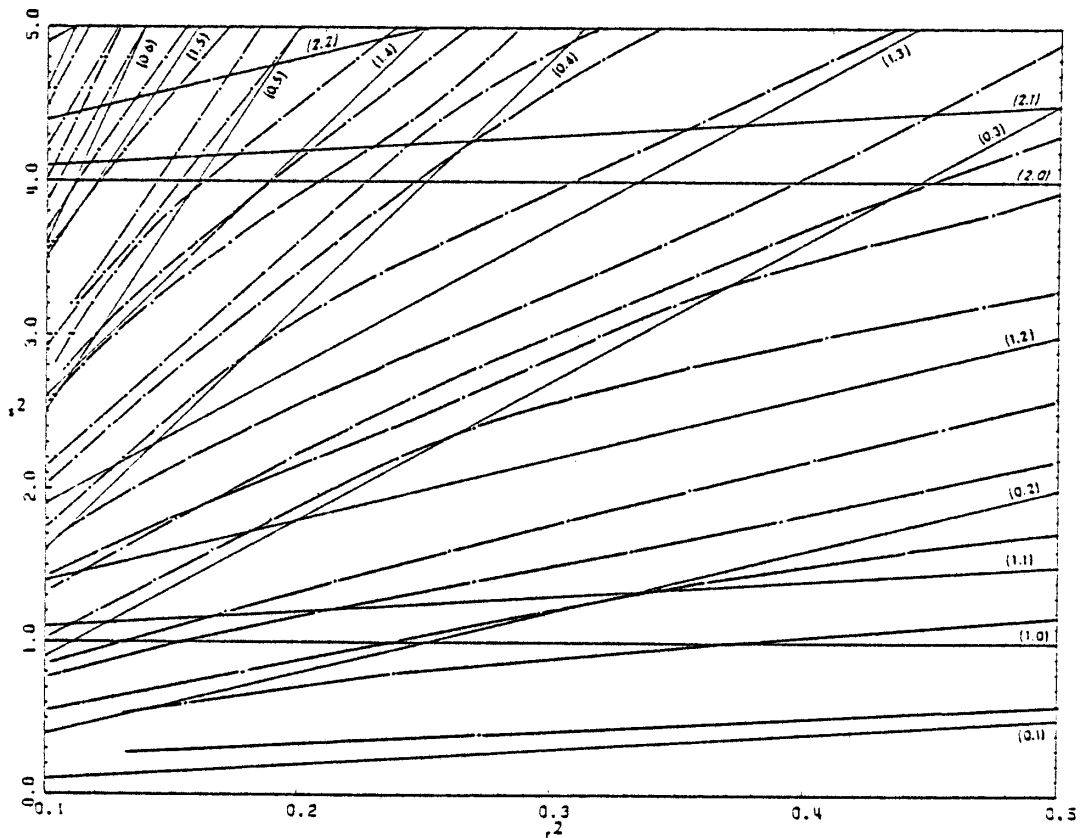


Figure 40. Eigencurves. Trapezoidal basins, (c,c) , $\gamma=7.5^\circ$, $f=0.25$.

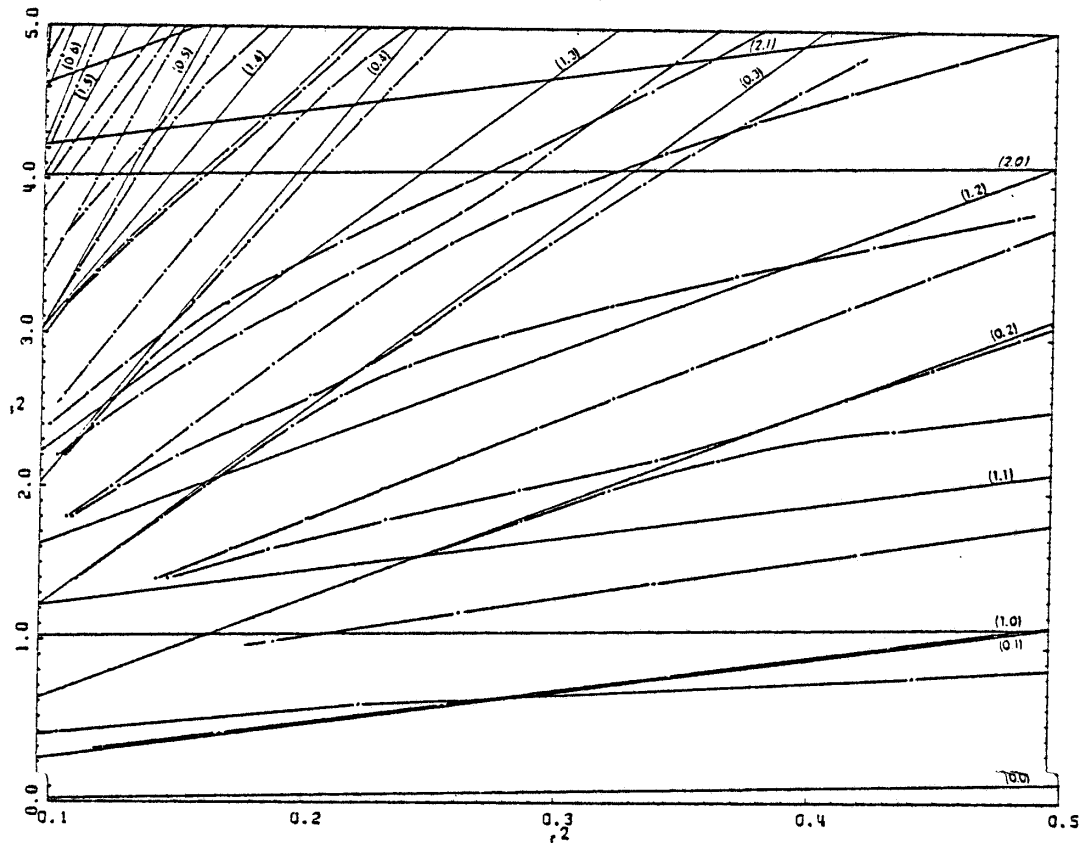


Figure 41. Eigencurves. Trapezoidal basins, $(c,0)$, $\gamma=7.5^\circ$, $f=0$.

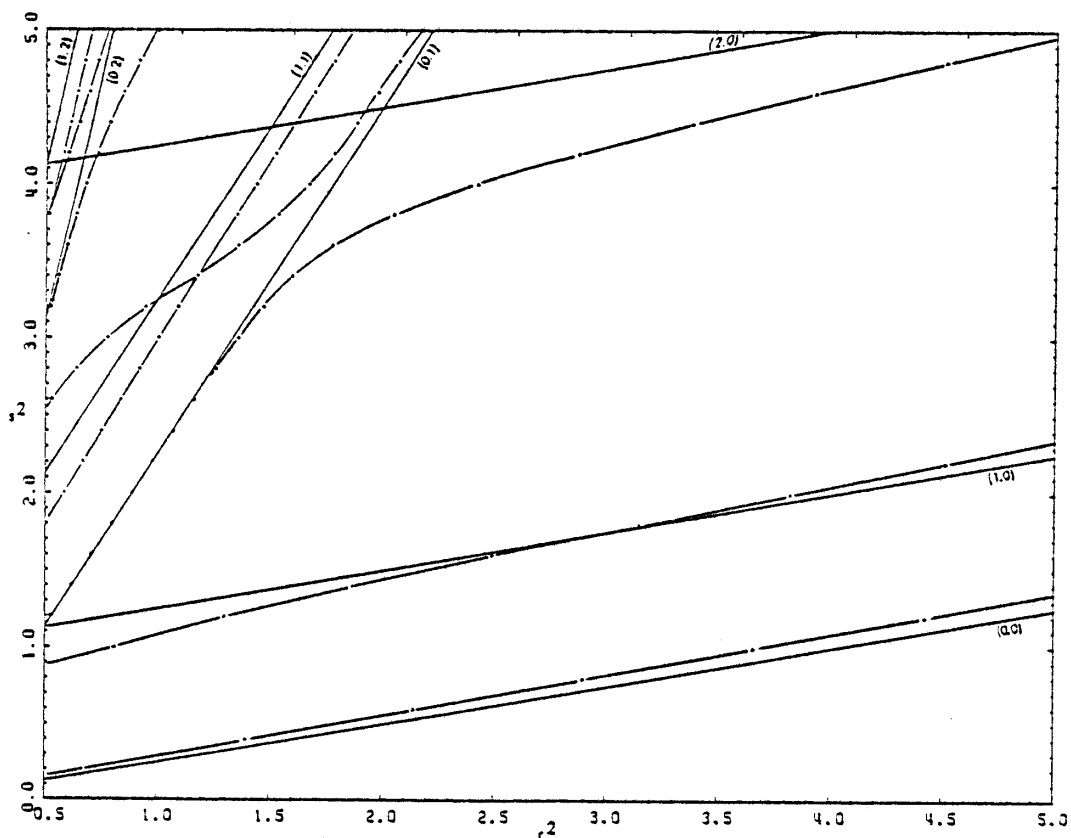


Figure 42. Eigencurves. Trapezoidal basins, $(c,0)$, $\gamma=7.5^\circ$, $f=0$.

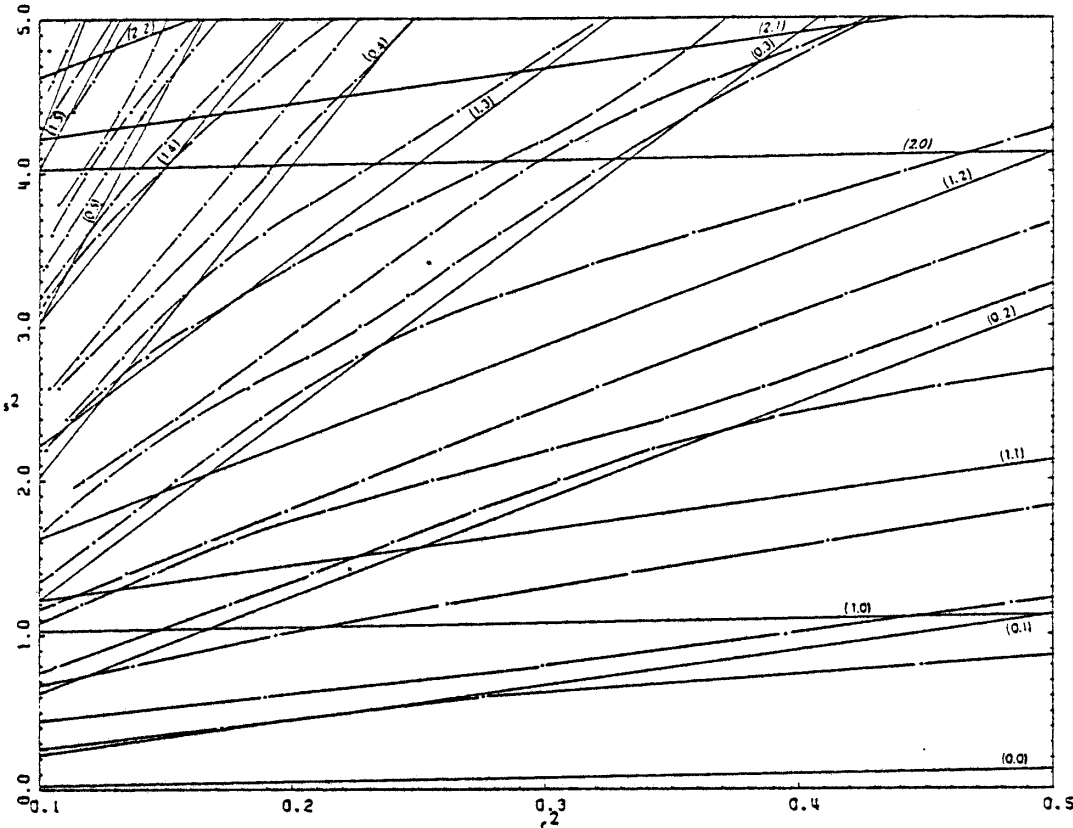


Figure 43. Eigencurves. Trapezoidal basins, $(c, 0)$, $\gamma = 7.5^\circ$, $f = 0.25$.

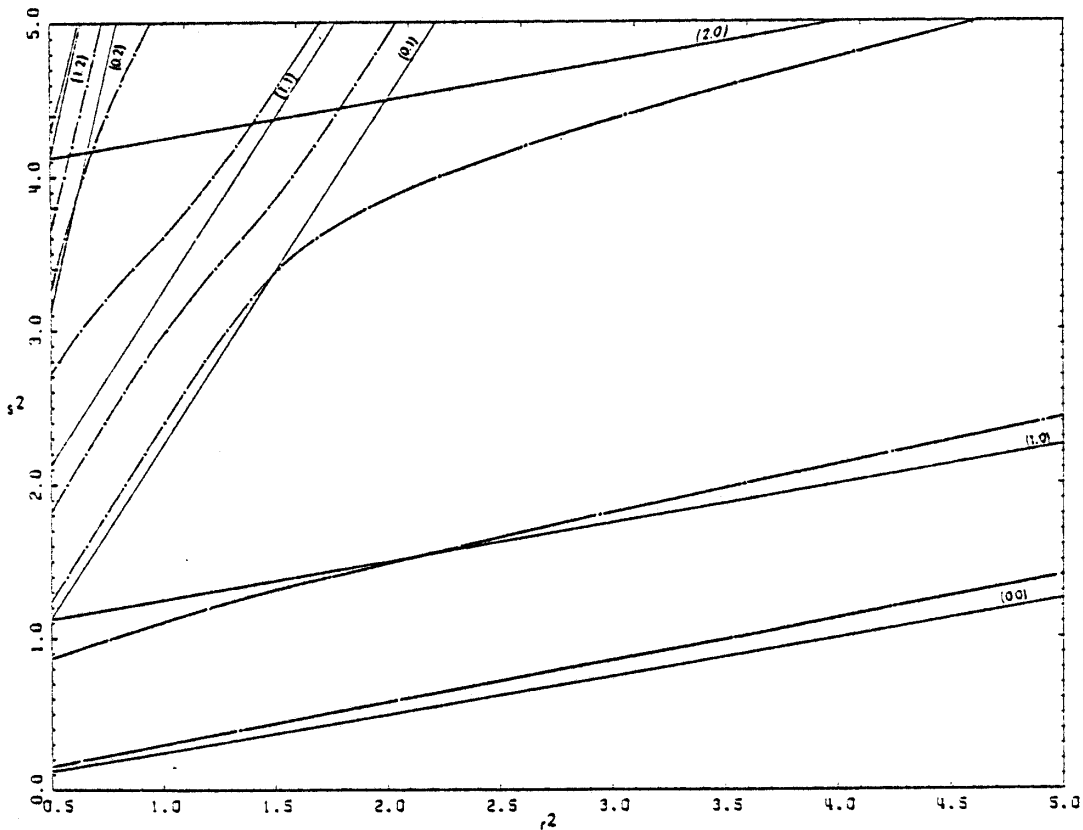


Figure 44. Eigencurves. Trapezoidal basins, $(c, 0)$, $\gamma = 7.5^\circ$, $f = 0.25$.

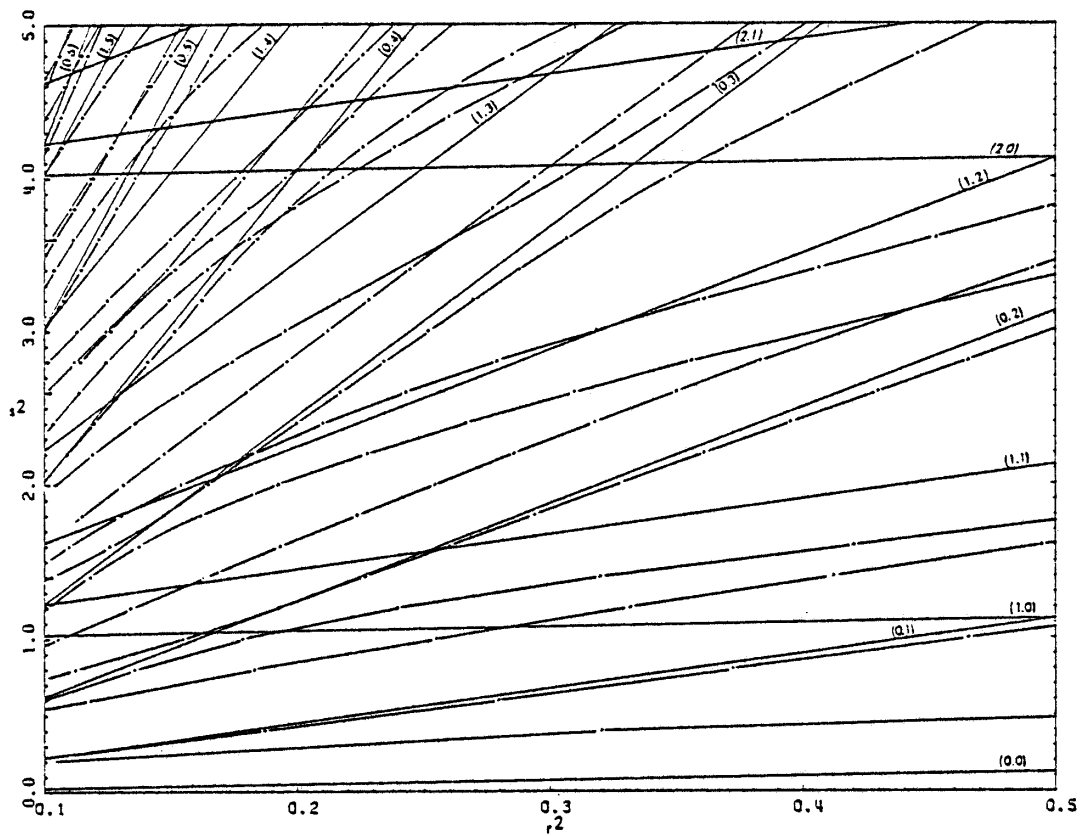


Figure 45. Eigencurves. Trapezoidal basins. $(0, c)$, $\gamma=7.5^\circ$, $f=0$.

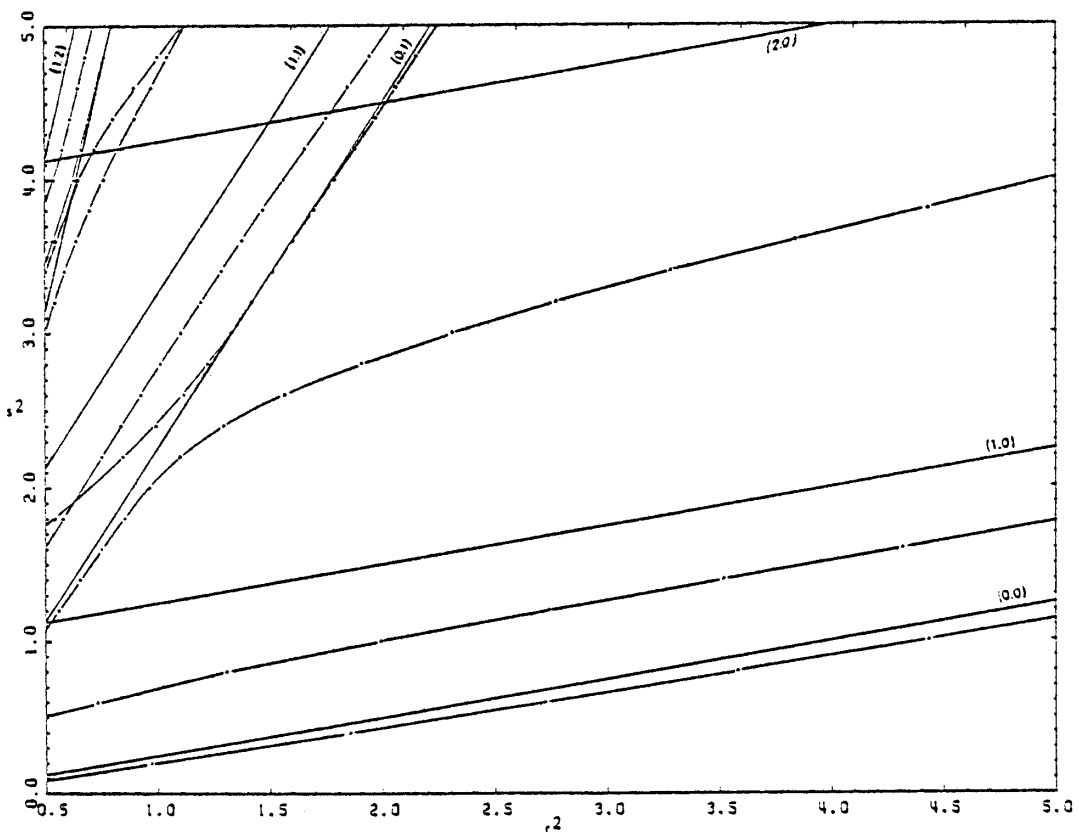


Figure 46. Eigencurves. Trapezoidal basins. $(0, c)$, $\gamma=7.5^\circ$, $f=0$.

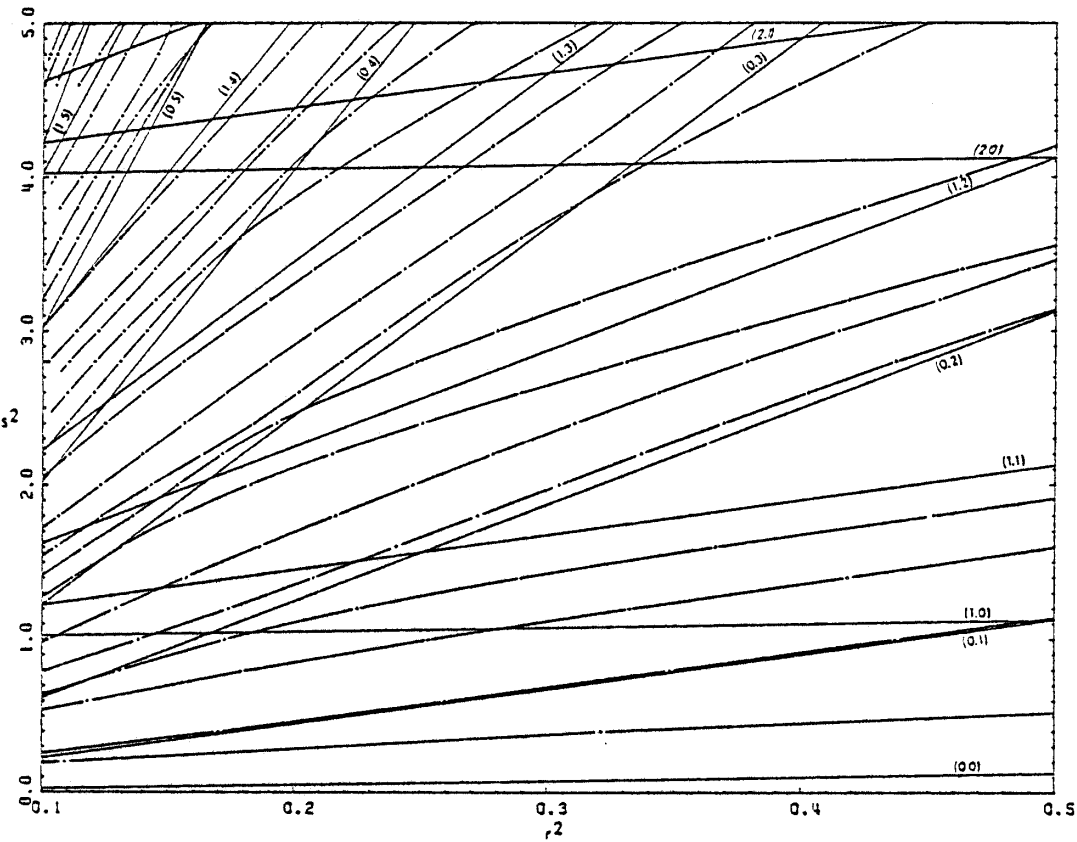


Figure 47. Eigencurves. Trapezoidal basins, $(0,c)$, $\gamma=7.5^\circ$, $f=0.25$.

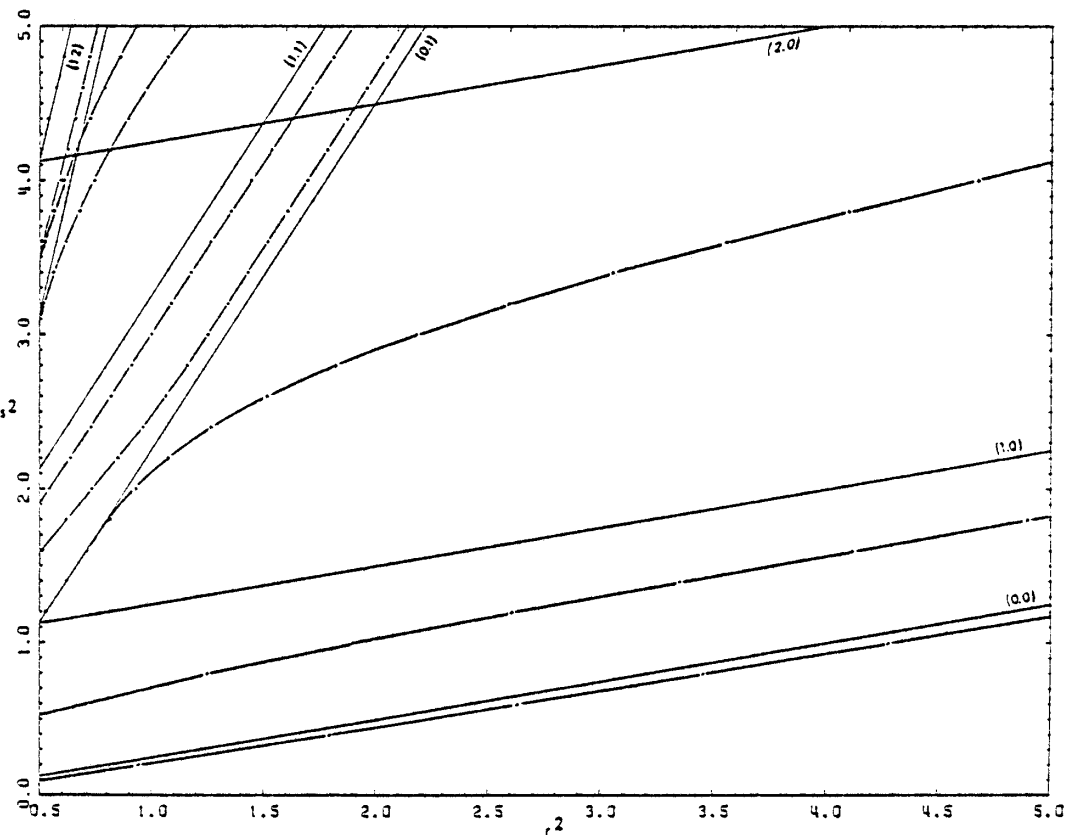


Figure 48. Eigencurves. Trapezoidal basins, $(0,c)$ $\gamma=7.5^\circ$, $f=0.25$.

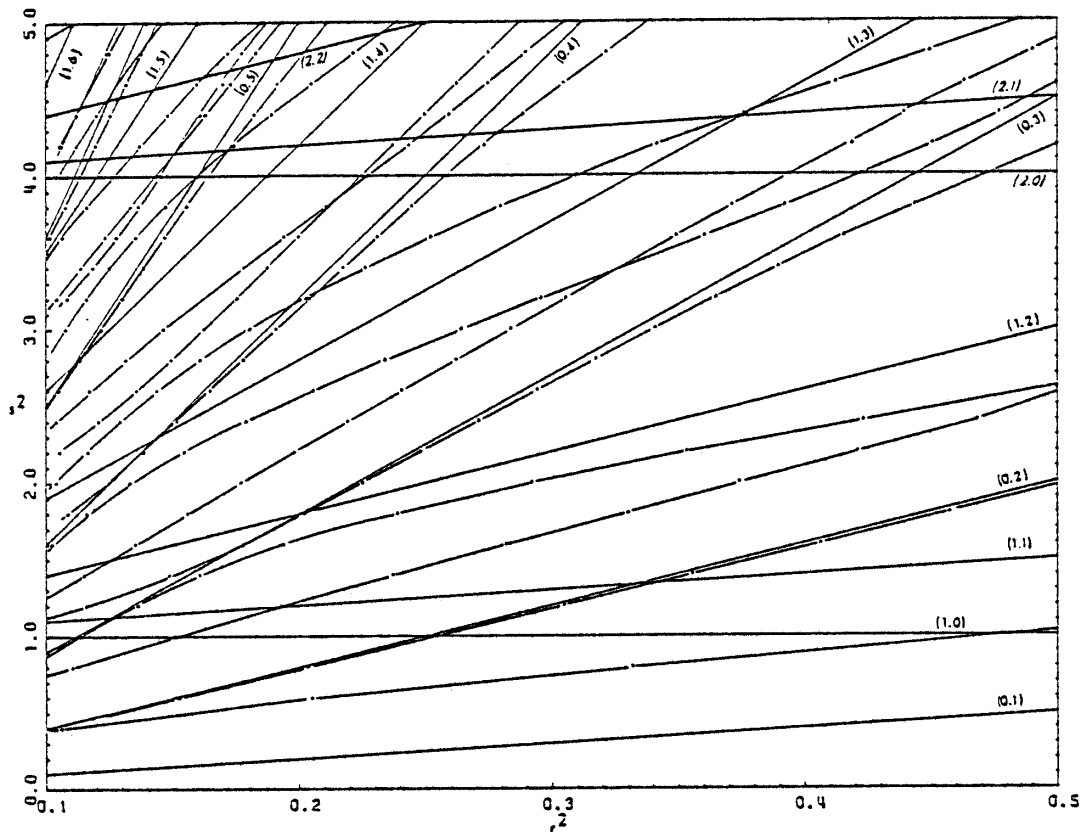


Figure 49. Eigencurves. Trapezoidal basins, $(0,0)$, $\gamma=7.5^\circ$, $f=0$.

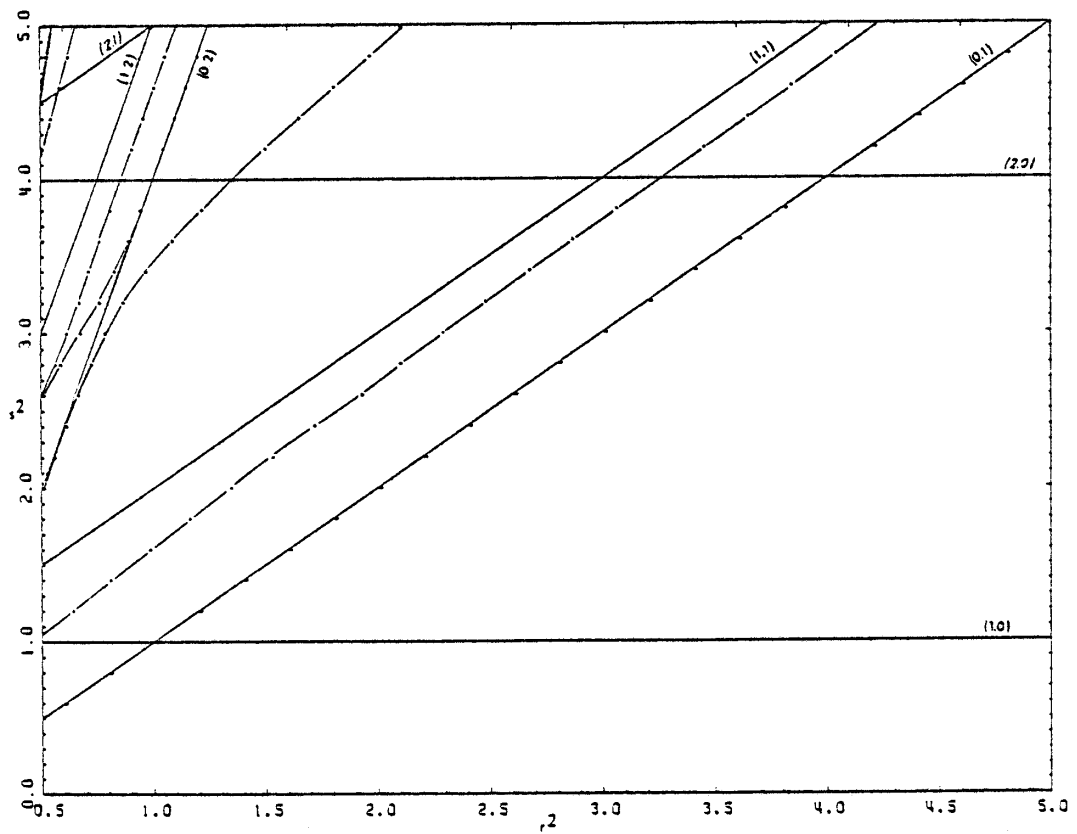


Figure 50. Eigencurves. Trapezoidal basins, $(0,0)$, $\gamma=7.5^\circ$, $f=0$.

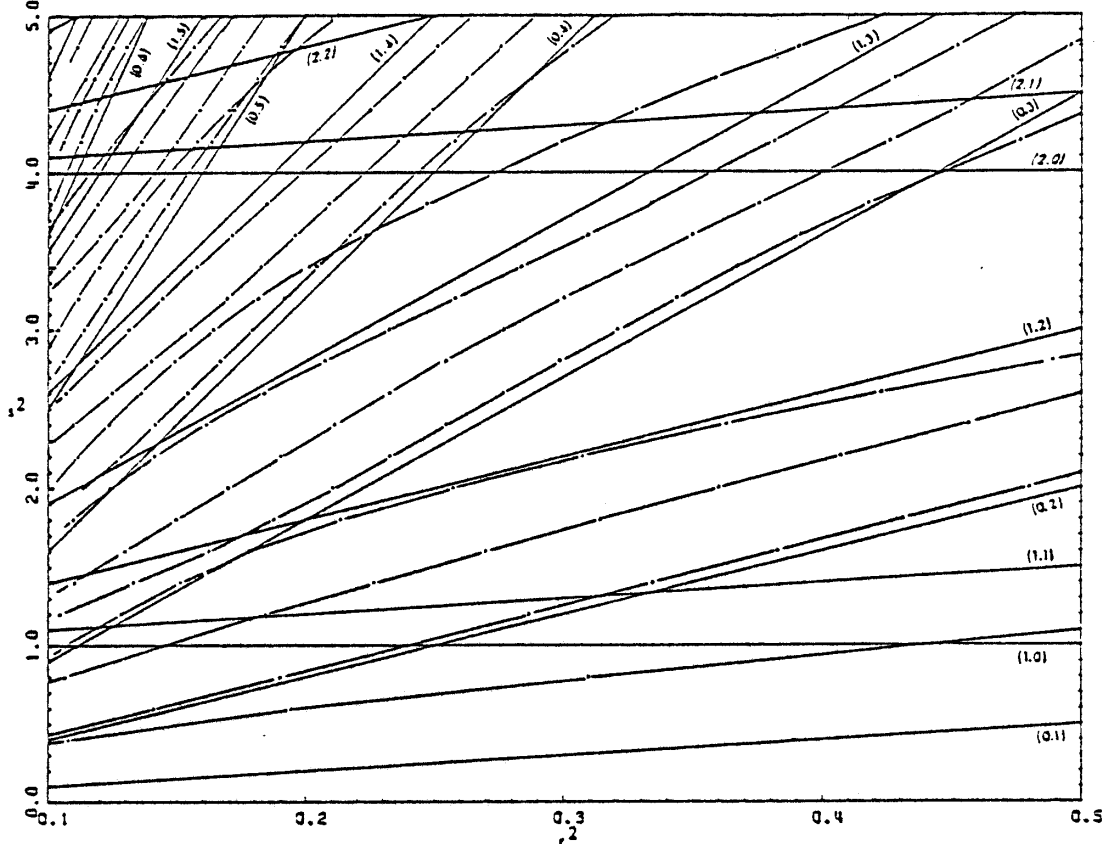


Figure 51. Eigencurves. Trapezoidal basins, $(0,0)$, $\gamma=7.5^\circ$, $f=0.25$.

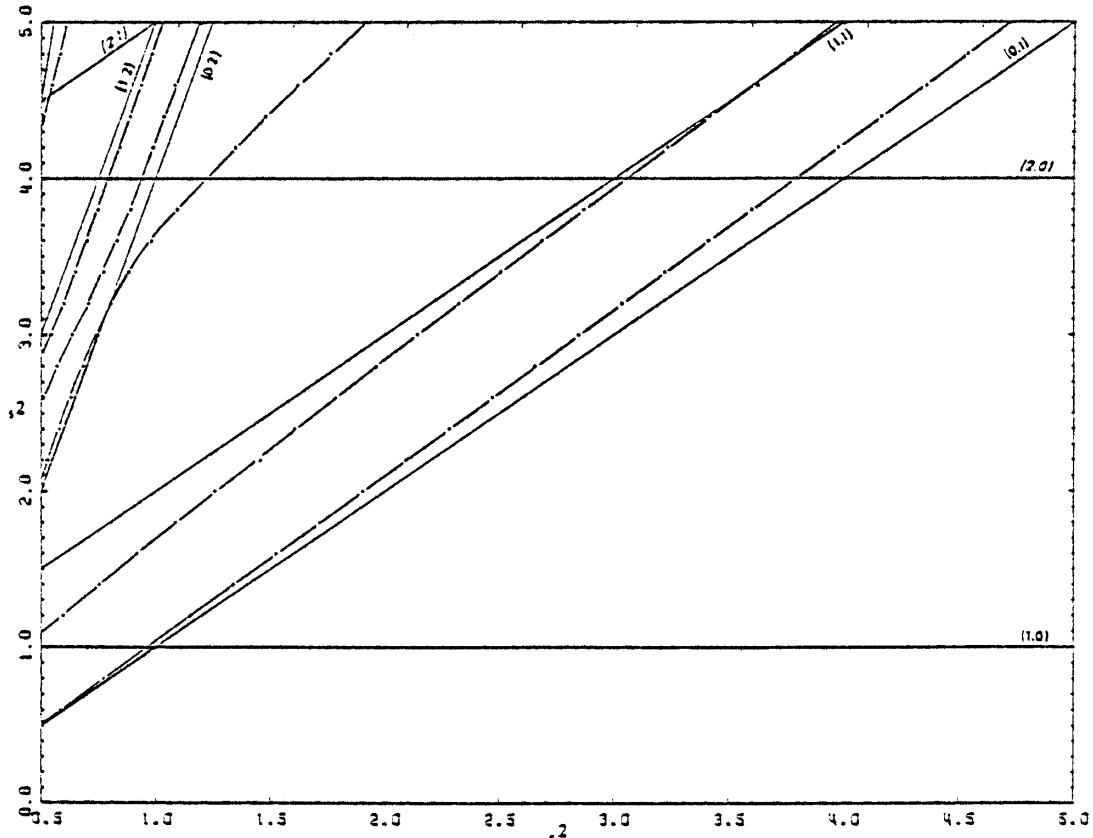


Figure 52. Eigencurves. Trapezoidal basins, $(0,0)$, $\gamma=7.5^\circ$, $f=0.25$.

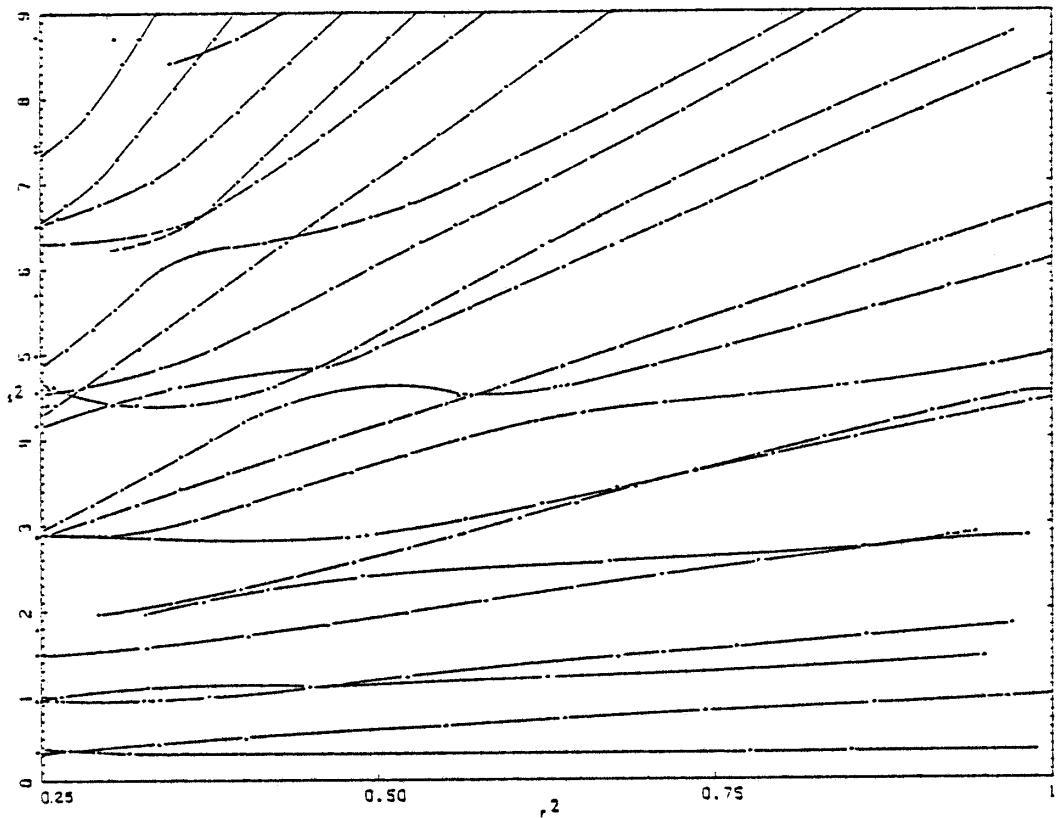


Figure 53. Eigencurves. Circular segment basins, (c,c) , $f=0$.

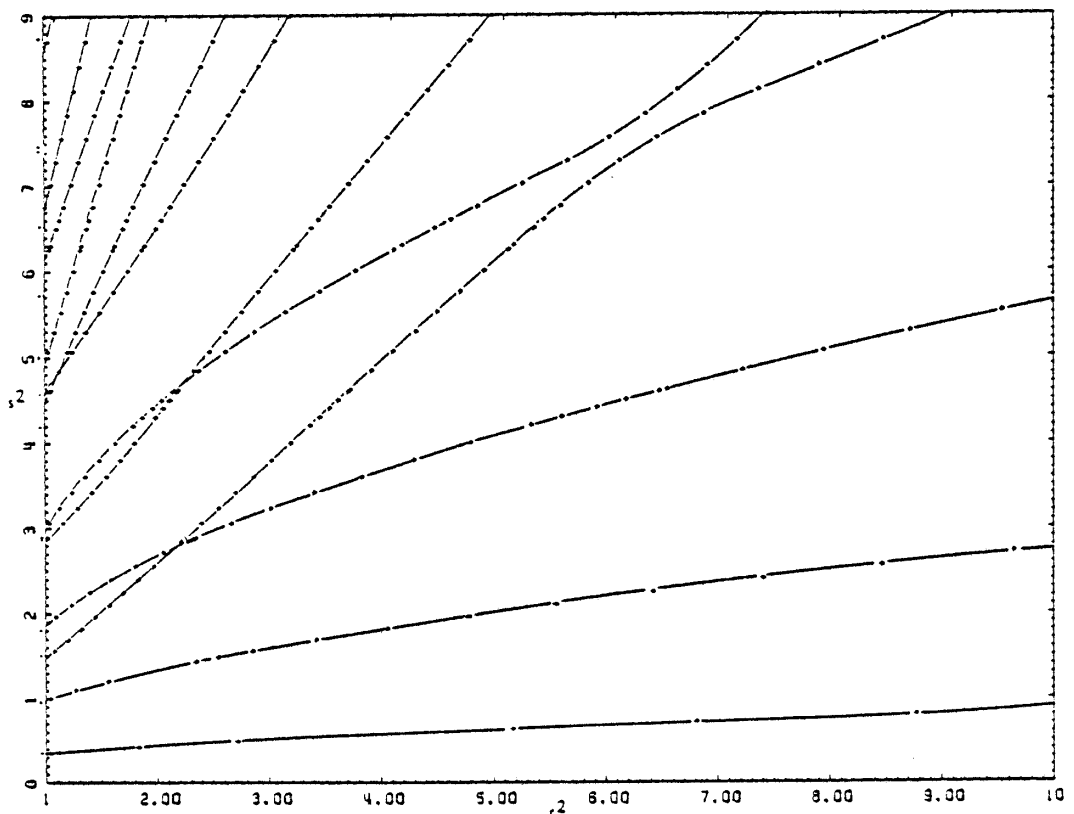


Figure 54. Eigencurves. Circular segment basins, (c,c) , $f=0$.

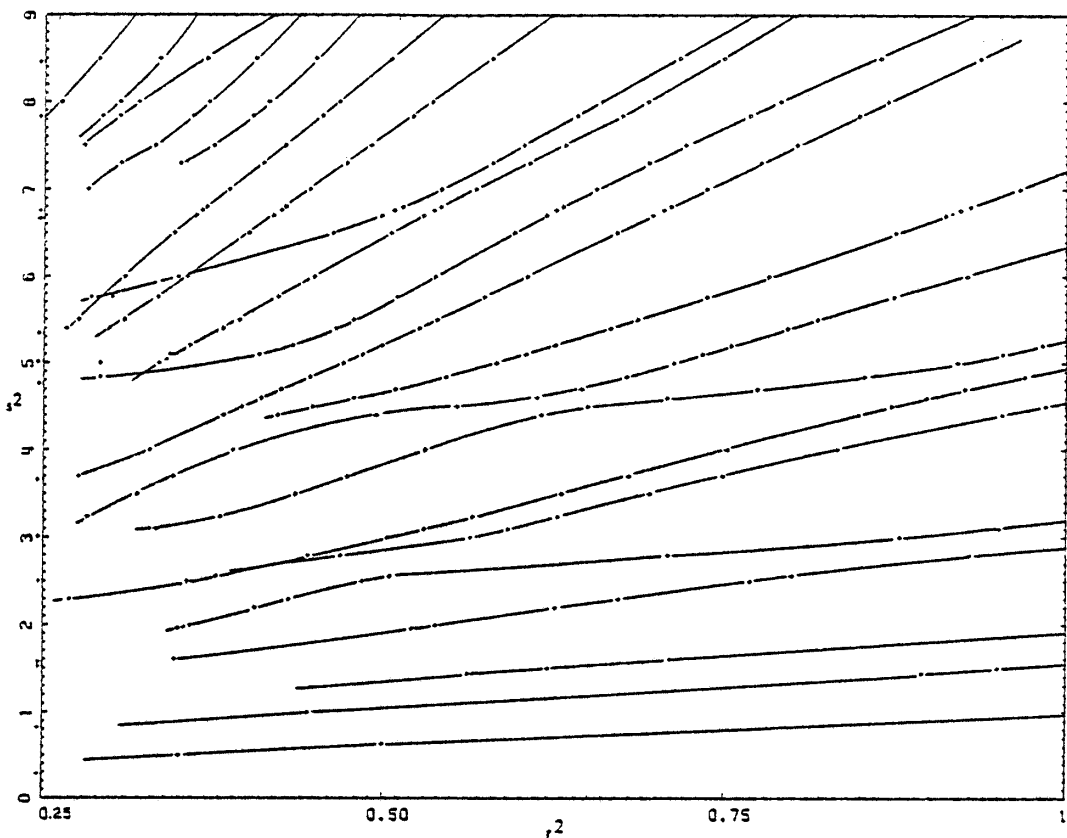


Figure 55. Eigencurves. Circular segment basins, (c,c) , $f=0.25$.

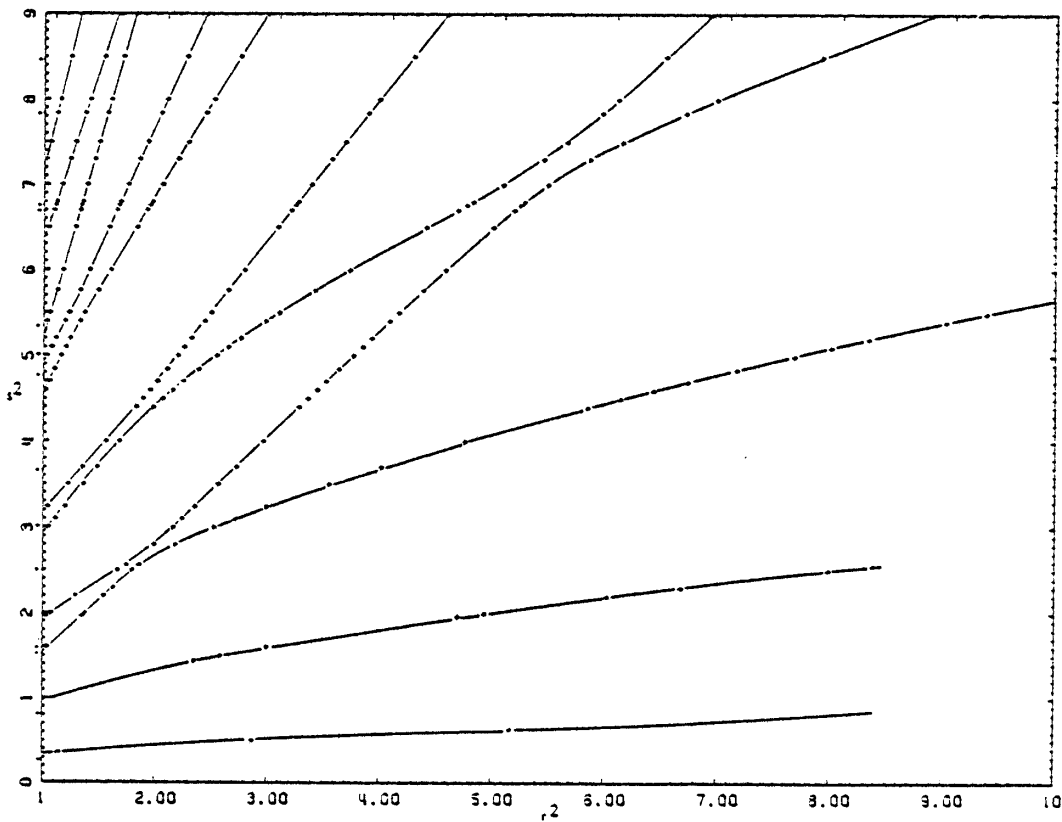


Figure 56. Eigencurves. Circular segment basins, (c,c) , $f=0.25$.

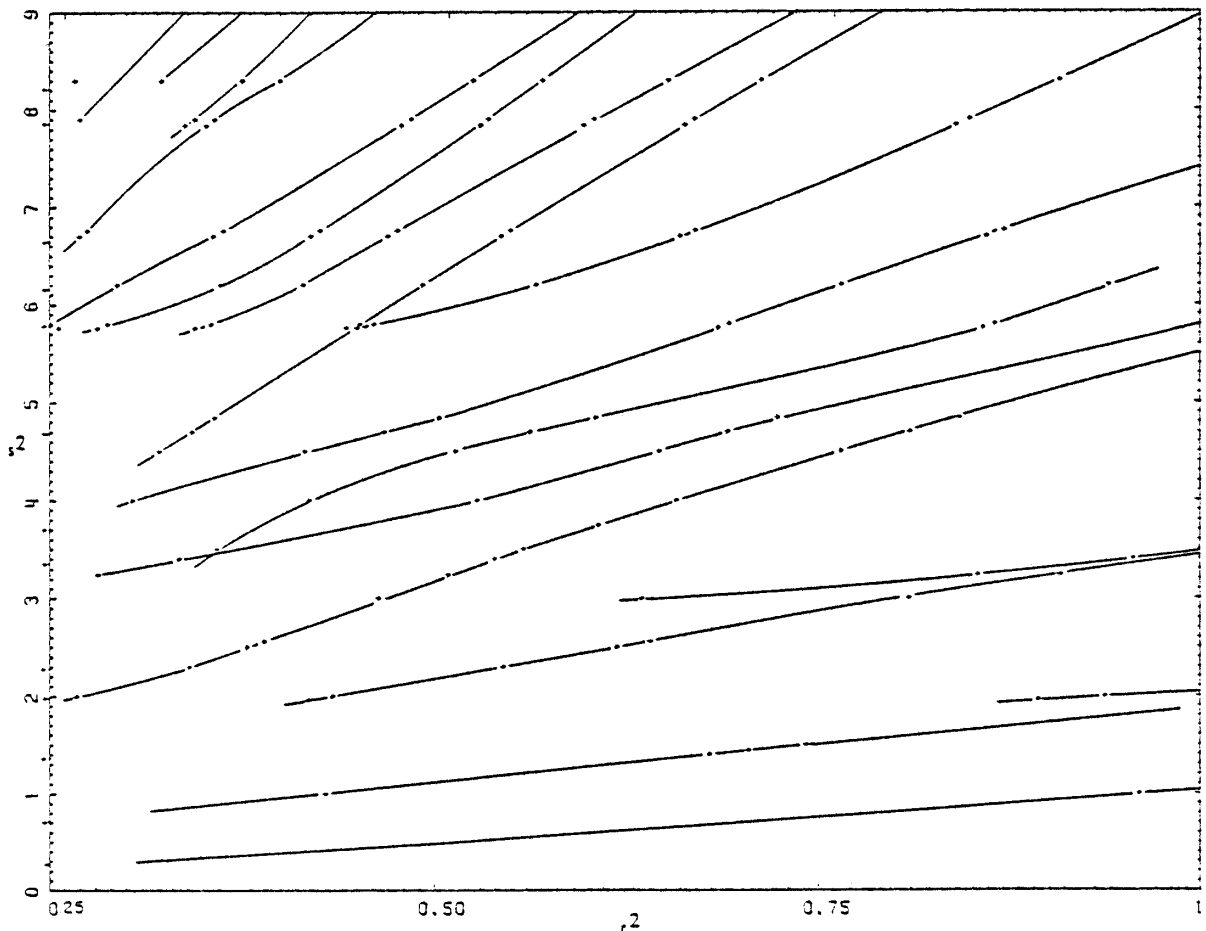


Figure 57. Eigencurves. Circular segment basins, (c,c) , $f=0.5$.

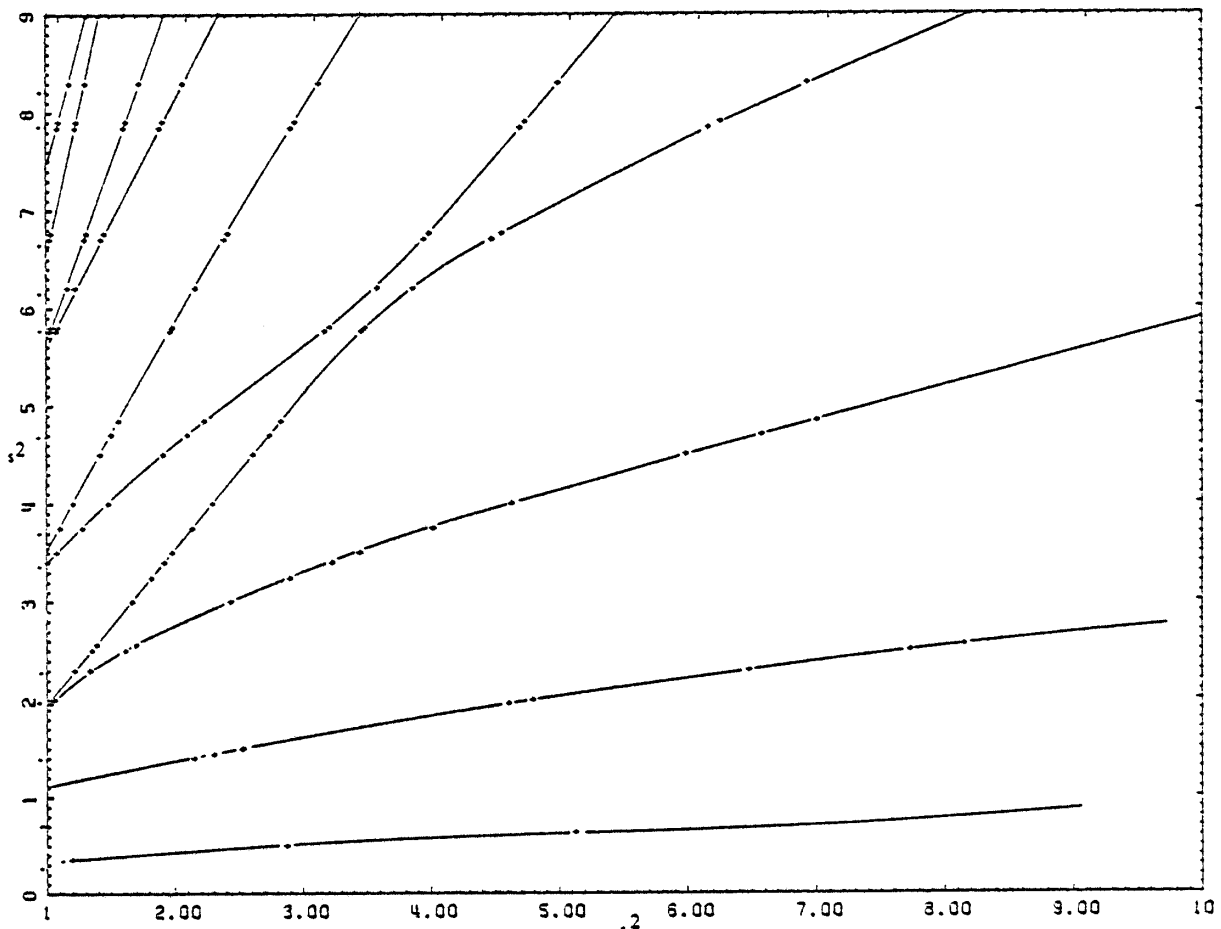


Figure 58. Eigencurves. Circular segment basins, (c,c) , $f=0.5$.

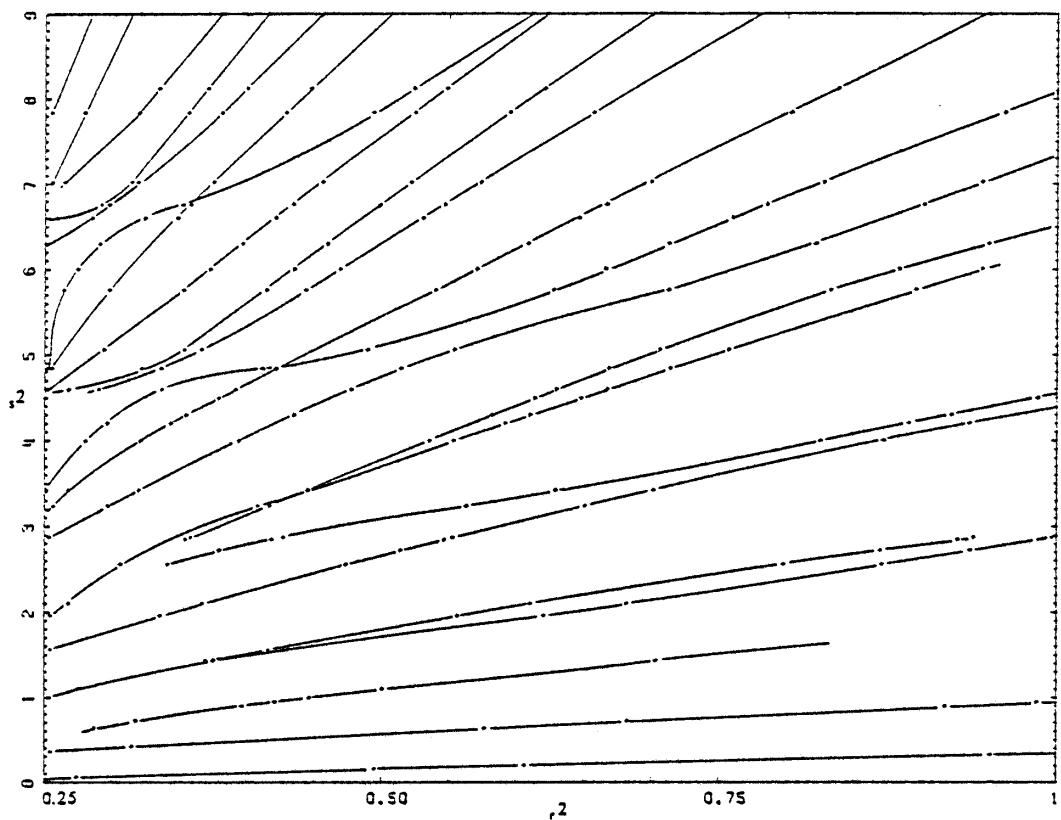


Figure 59. Eigencurves. Circular segment basins, $(c, 0)$, $f=0$.

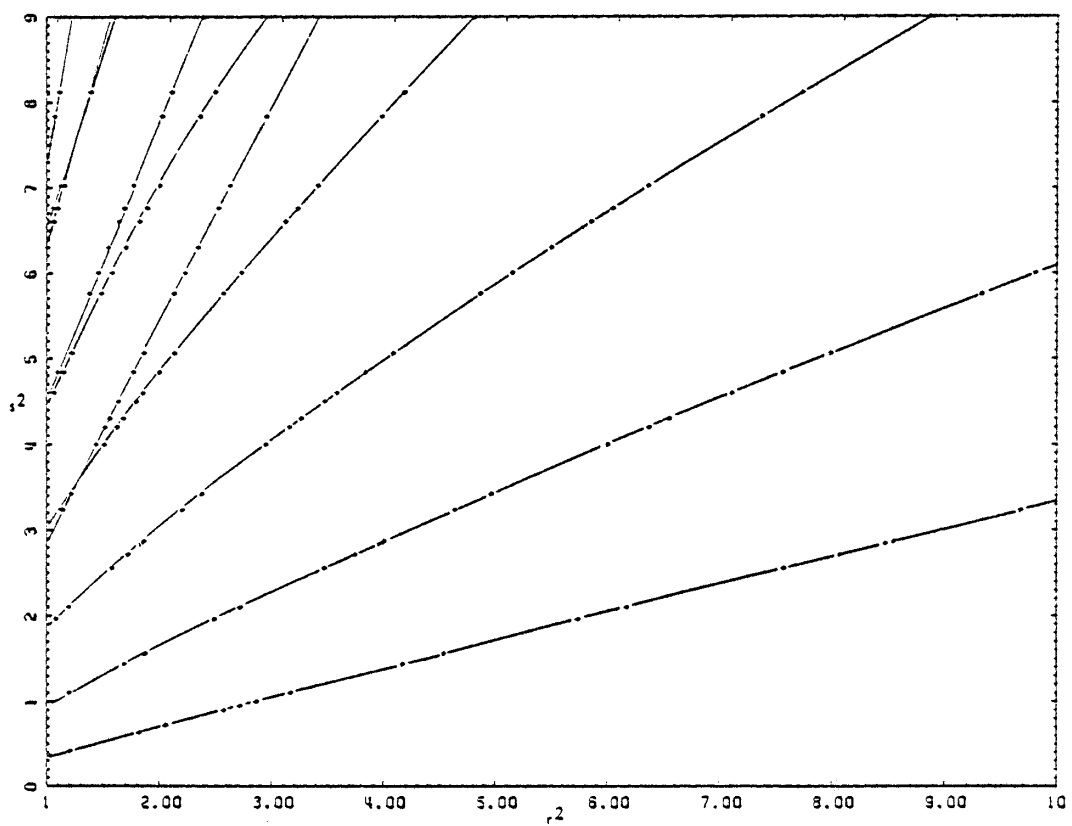


Figure 60. Eigencurves. Circular segment basins, $(c, 0)$, $f=0$.

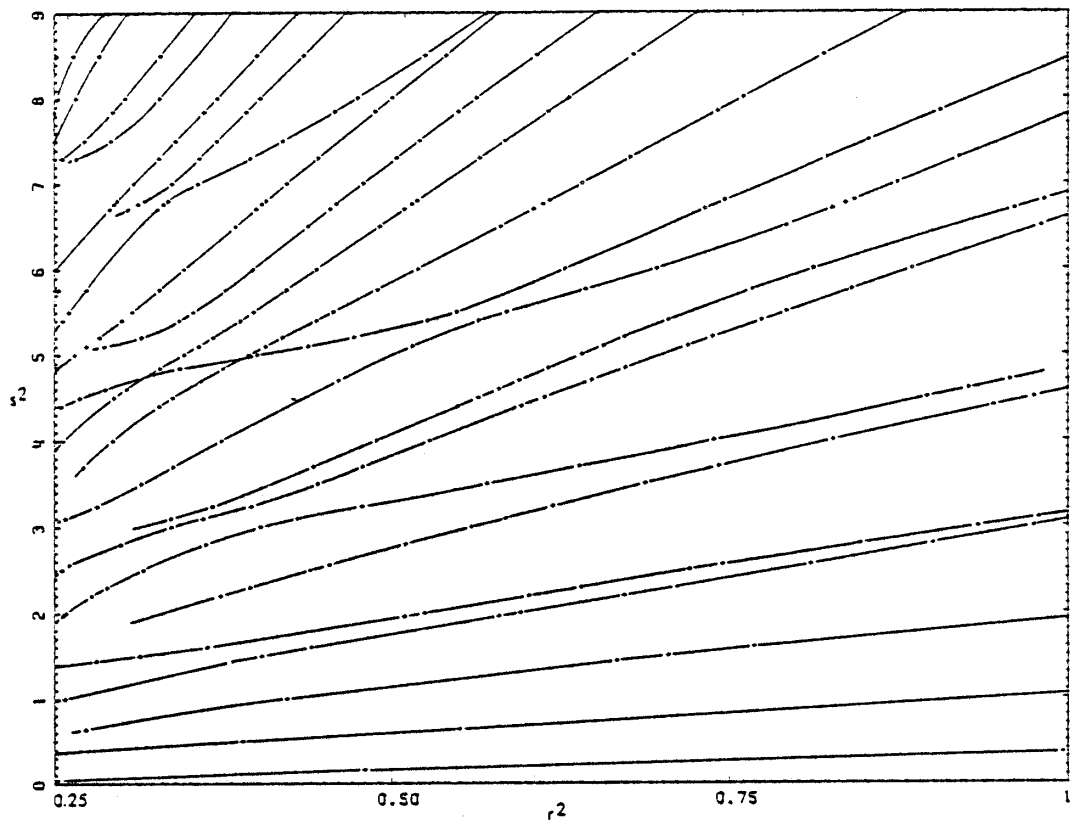


Figure 61. Eigencurves. Circular segment basins, $(c, 0)$, $f=0.25$.

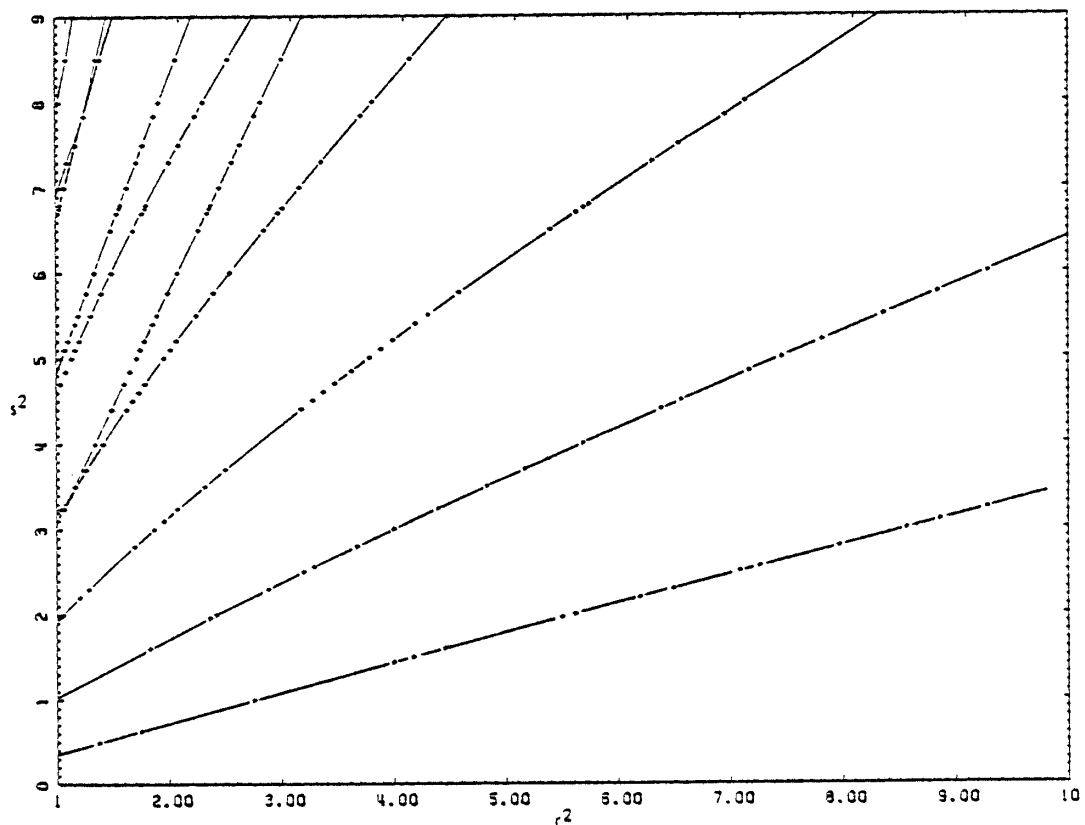


Figure 62. Eigencurves. Circular segment basins, $(c, 0)$, $f=0.25$.

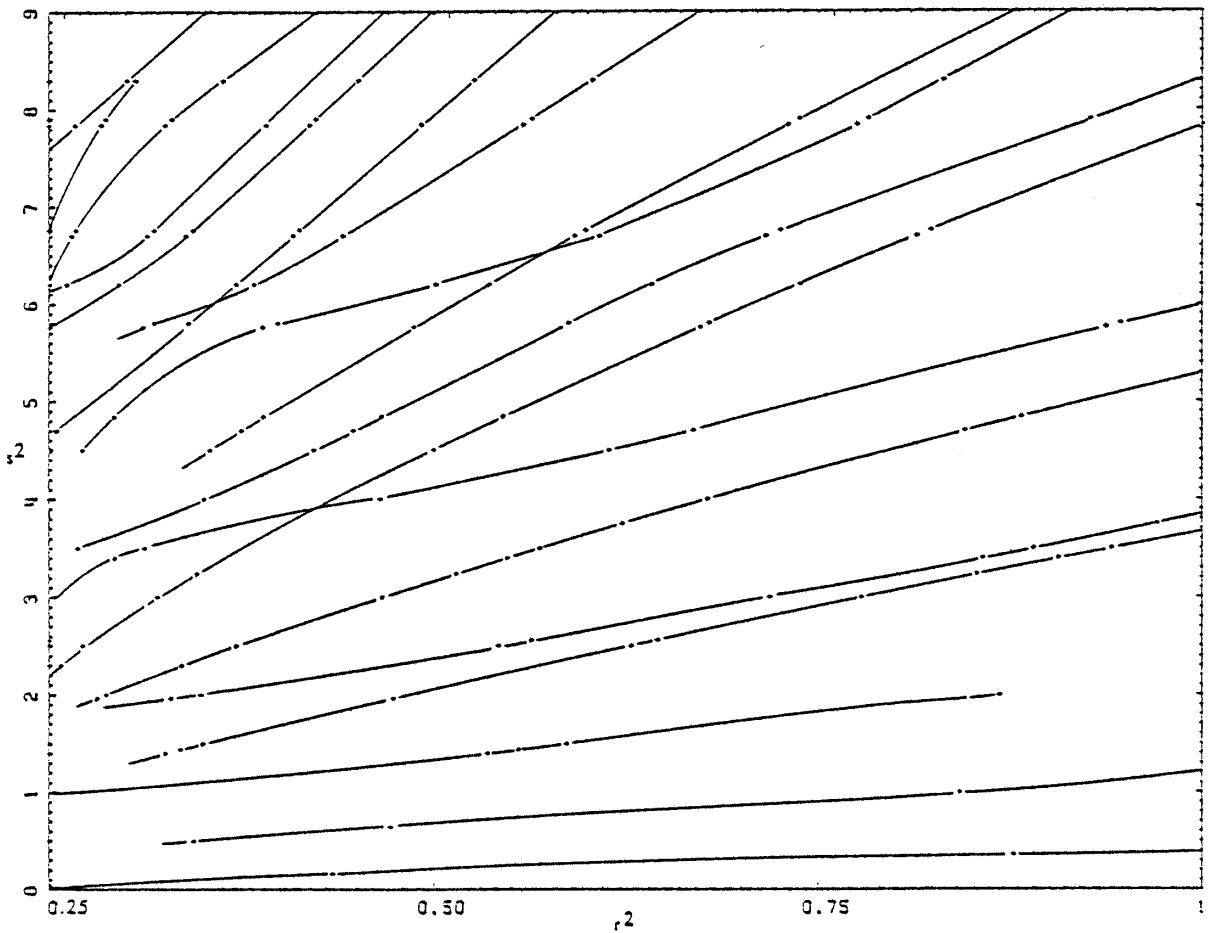


Figure 63. Eigencurves. Circular segment basins, $(c, 0)$, $f=0.5$.

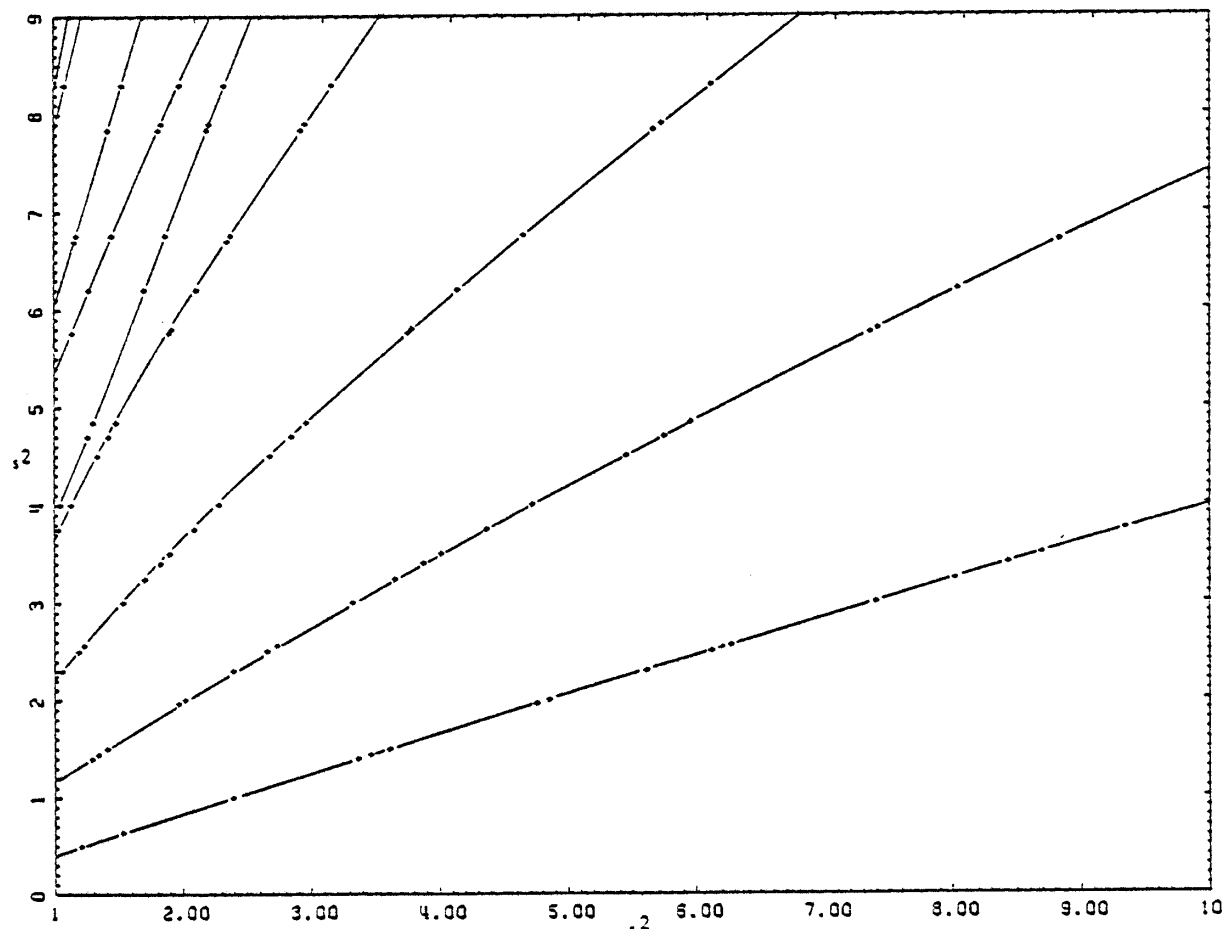


Figure 64. Eigencurves. Circular segment basins, $(c, 0)$, $f=0.5$.

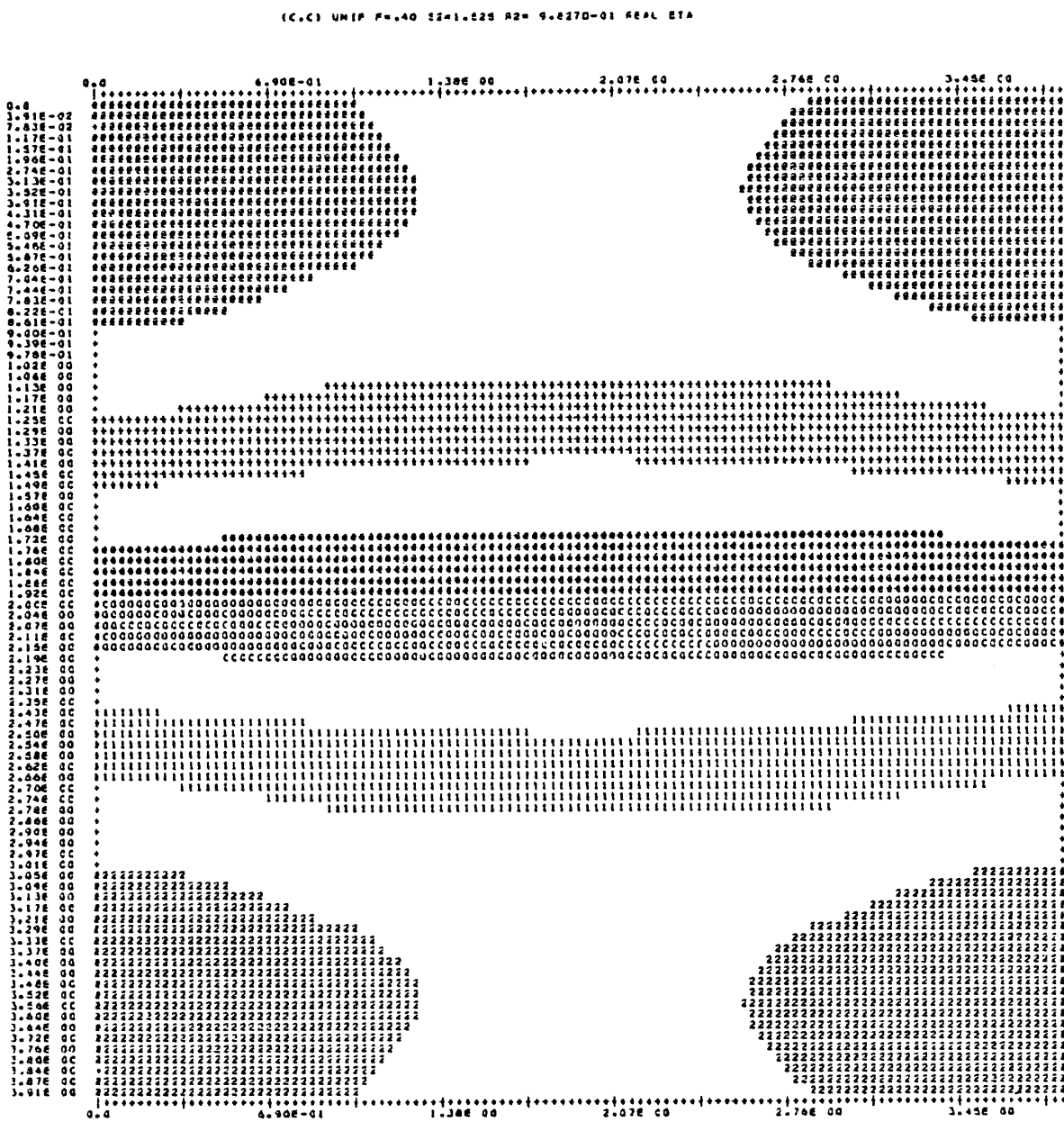


Figure 65. Eigenmode for rectangular (uniform) basins.

$$(r^2, s^2) = (0.983, 1.53), f = 0.40.$$

(C,C) UNIF P=AC S2=1.525 R2= 9.8270-01 IMAG ETA

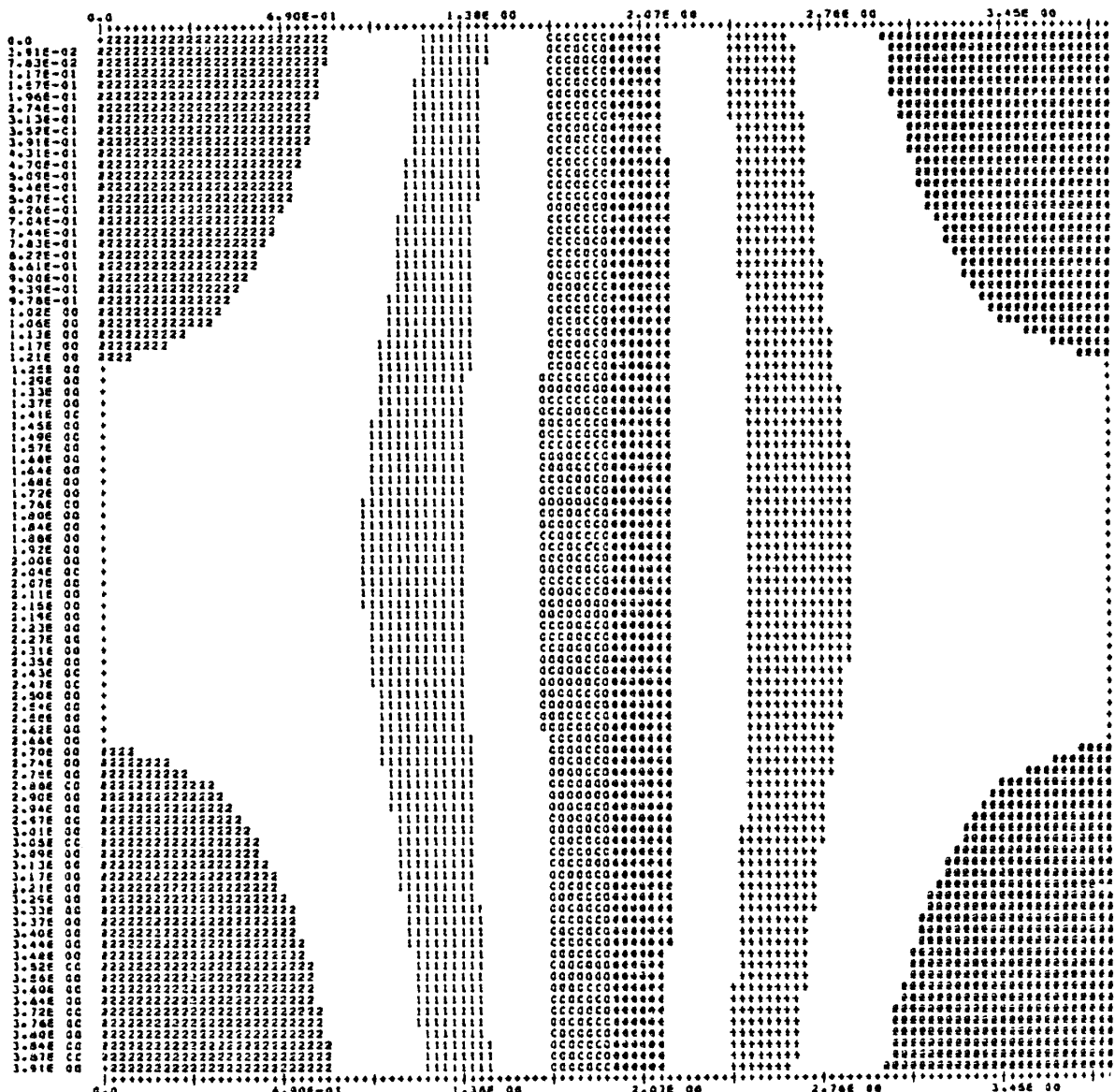


Figure 65. (cont.)

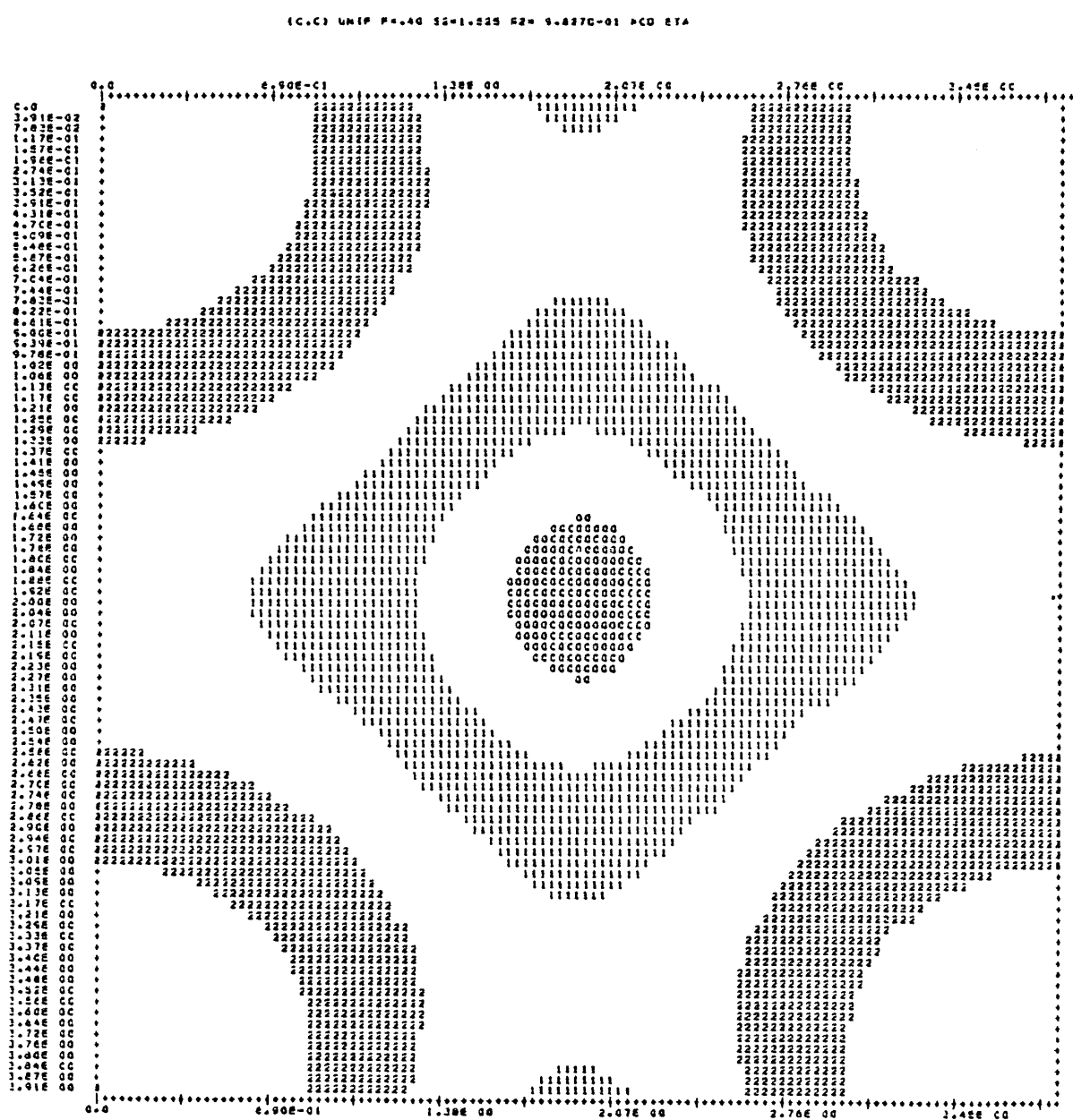


Figure 65. (cont.)

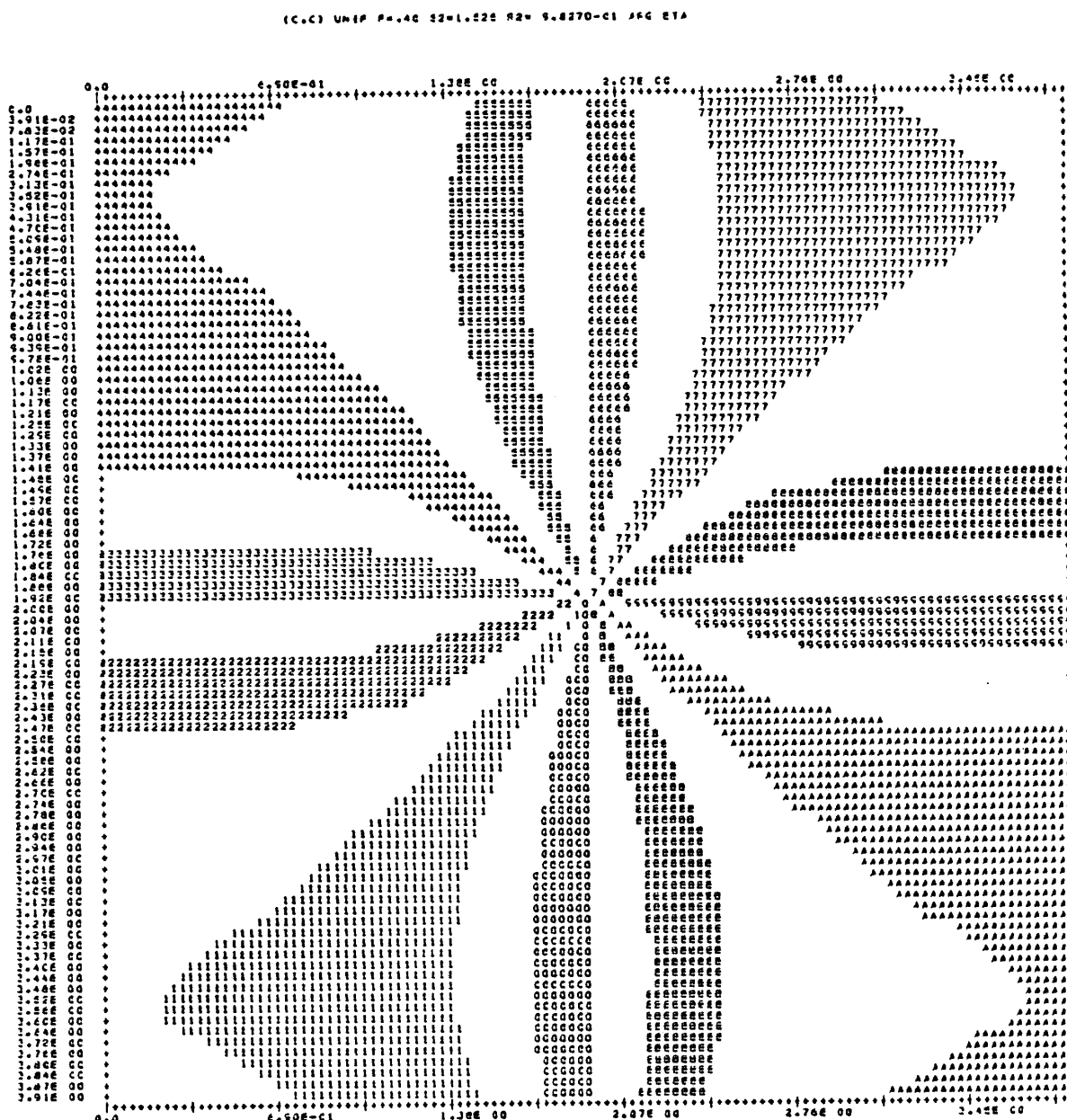


Figure 65. (cont.)

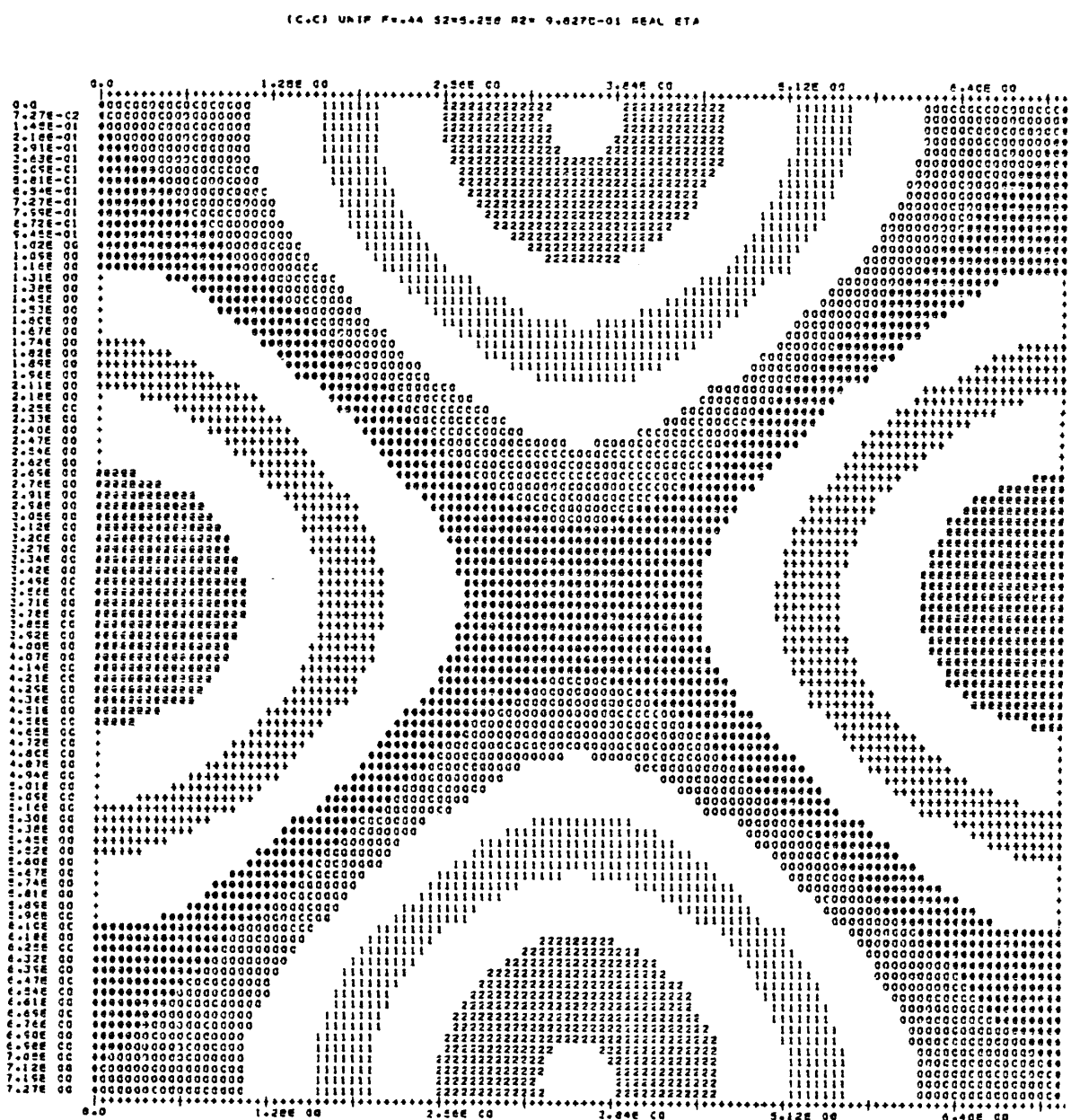


Figure 66. Eigenmode for rectangular (uniform) basins.

$$(r^2, s^2) = (0.983, 5.26), f = 0.44.$$

(C,C) UNIF F=.44 S2=5.256 R2= 9.8270-01 IMAG ETP

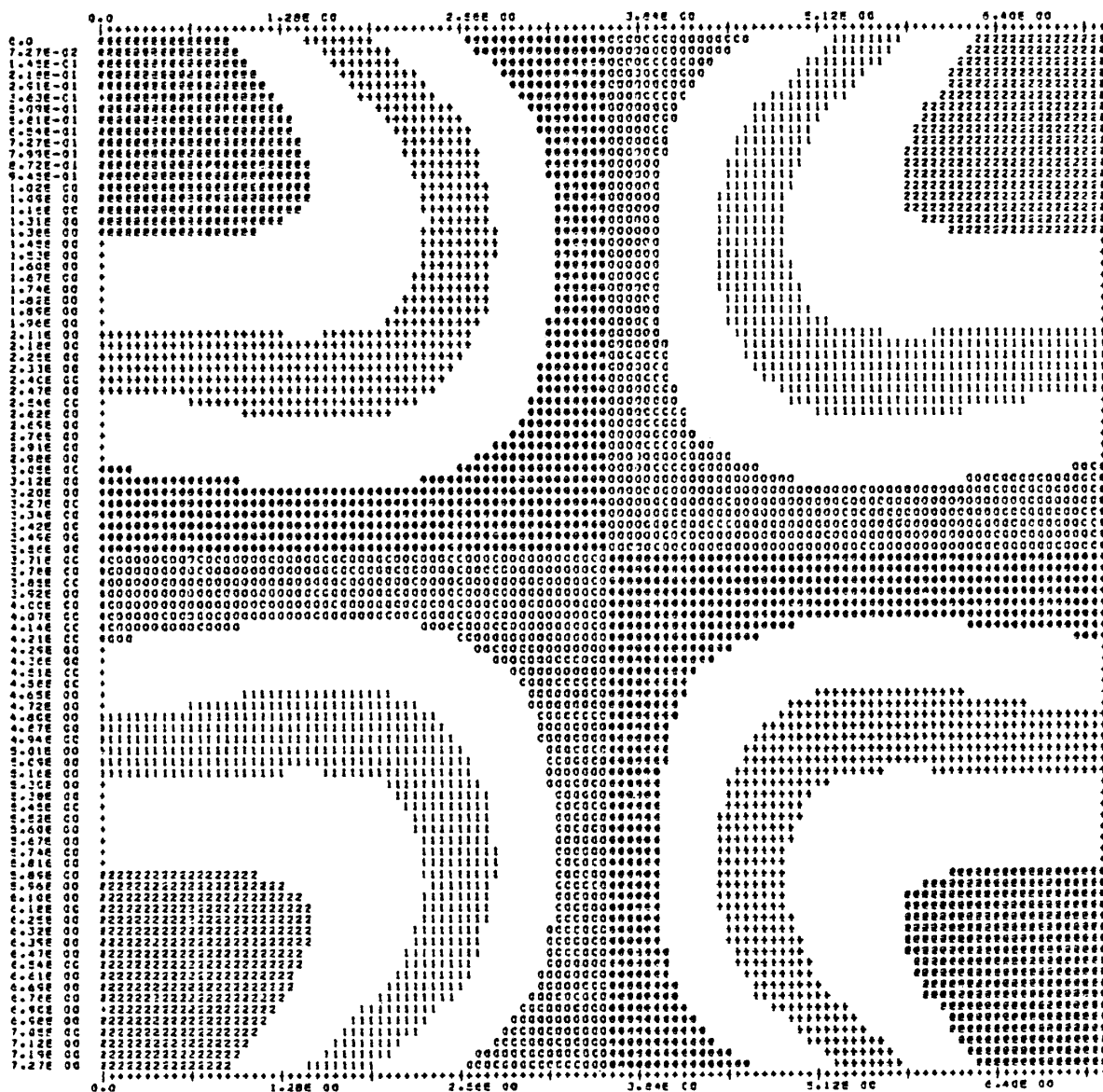


Figure 66. (cont.)

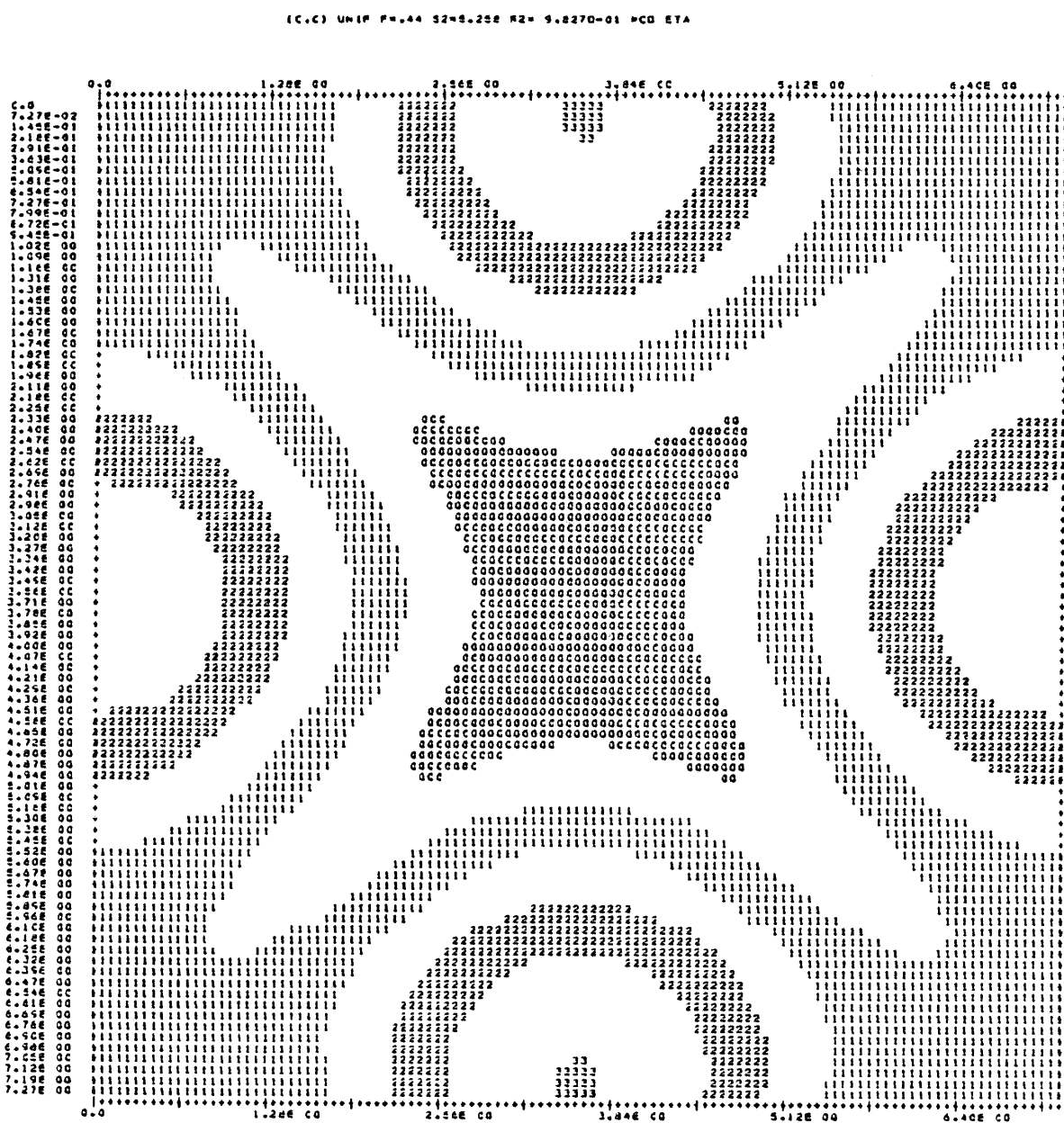


Figure 66. (cont.)

(C,C) UNIF F=44 S3=S.25E R2= S.227C-01 AEG ETA

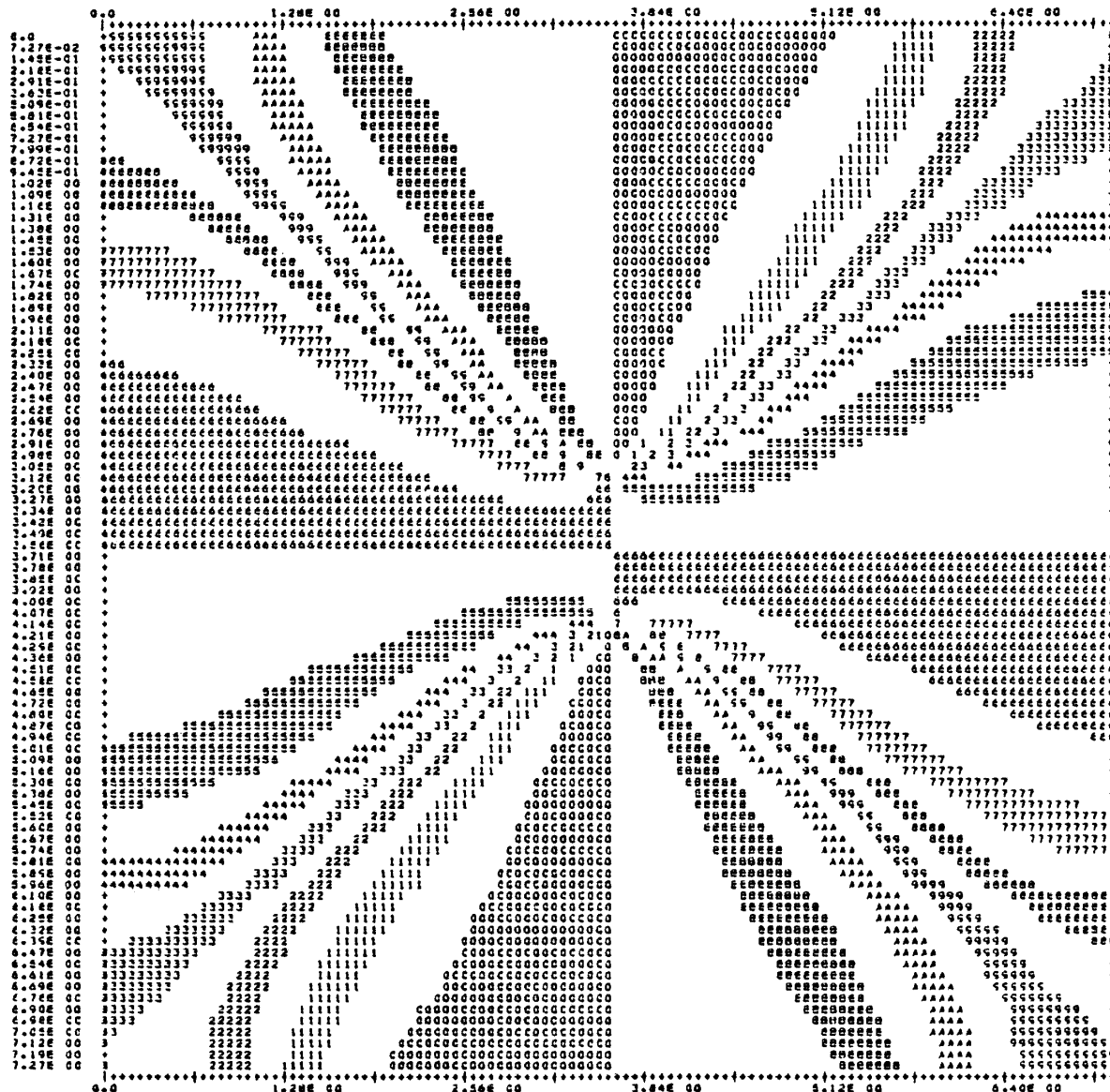


Figure 66. (cont.)

(C,C) UNIF F=.40 S2=1.596 R2= 2.4550-C1 REAL ETA

(C,C) UNIF F=.40 S2=1.596 R2= 2.4550-C1 IMAG ETA

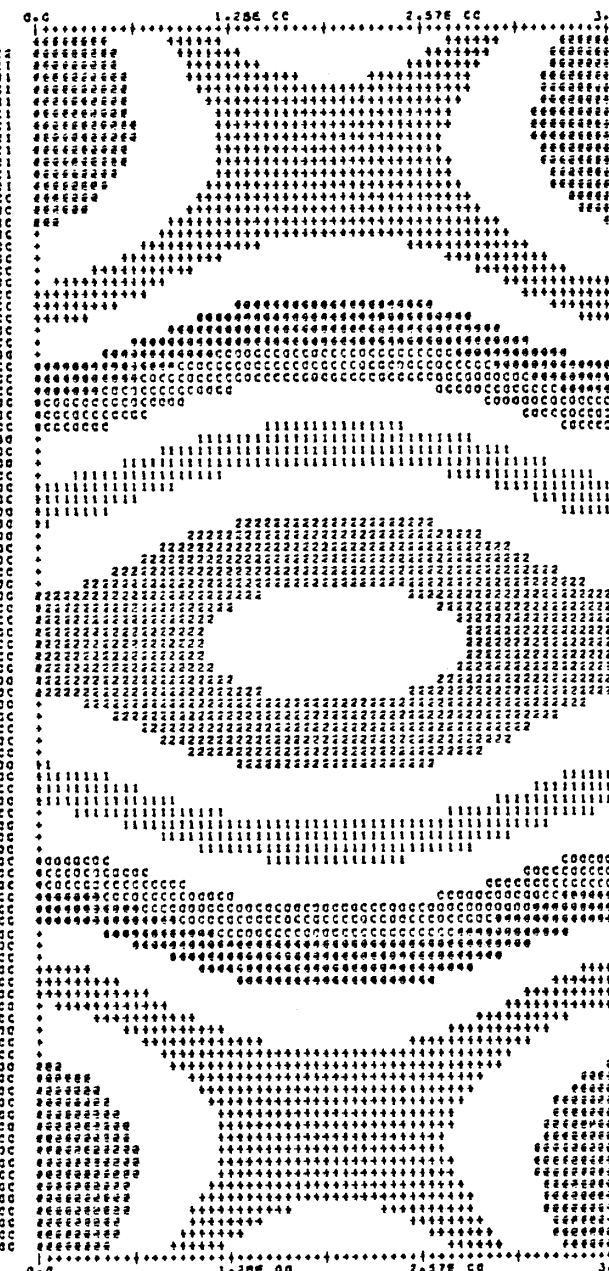
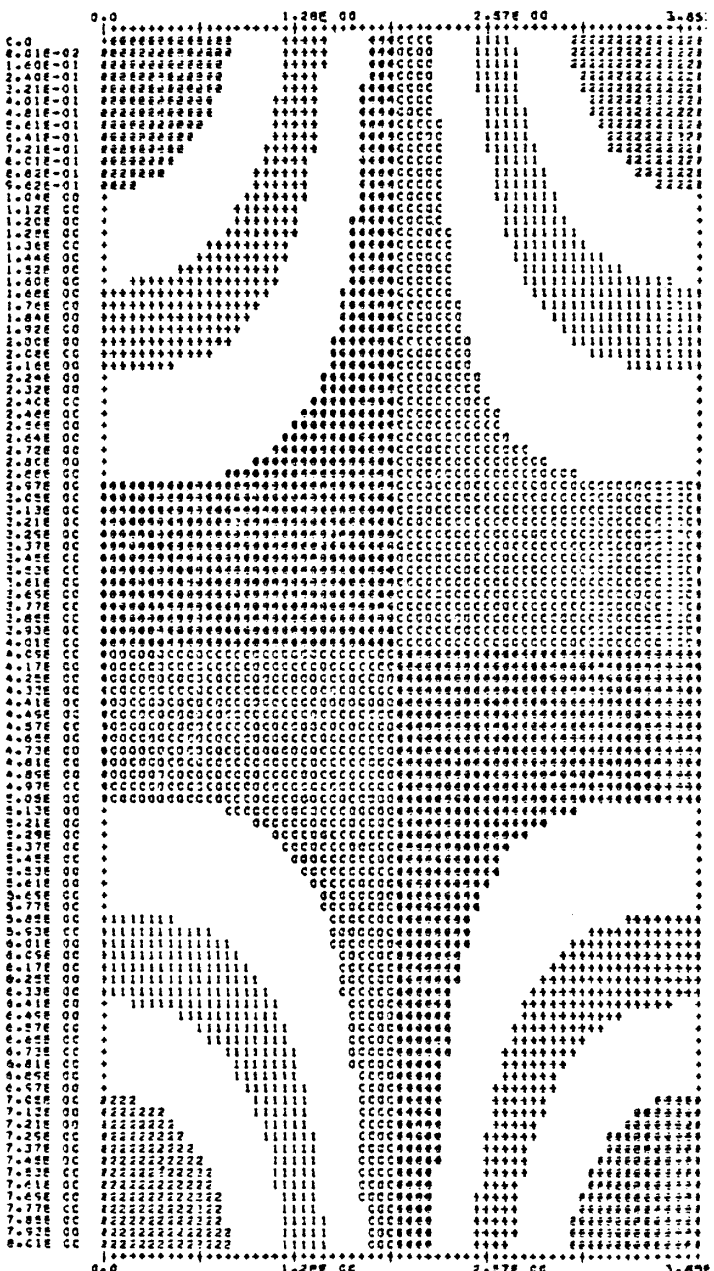


Figure 67. Eigenmode for rectangular (uniform) basin.

$$(r^2, s^2) = (0.246, 1.60), f = 0.40.$$

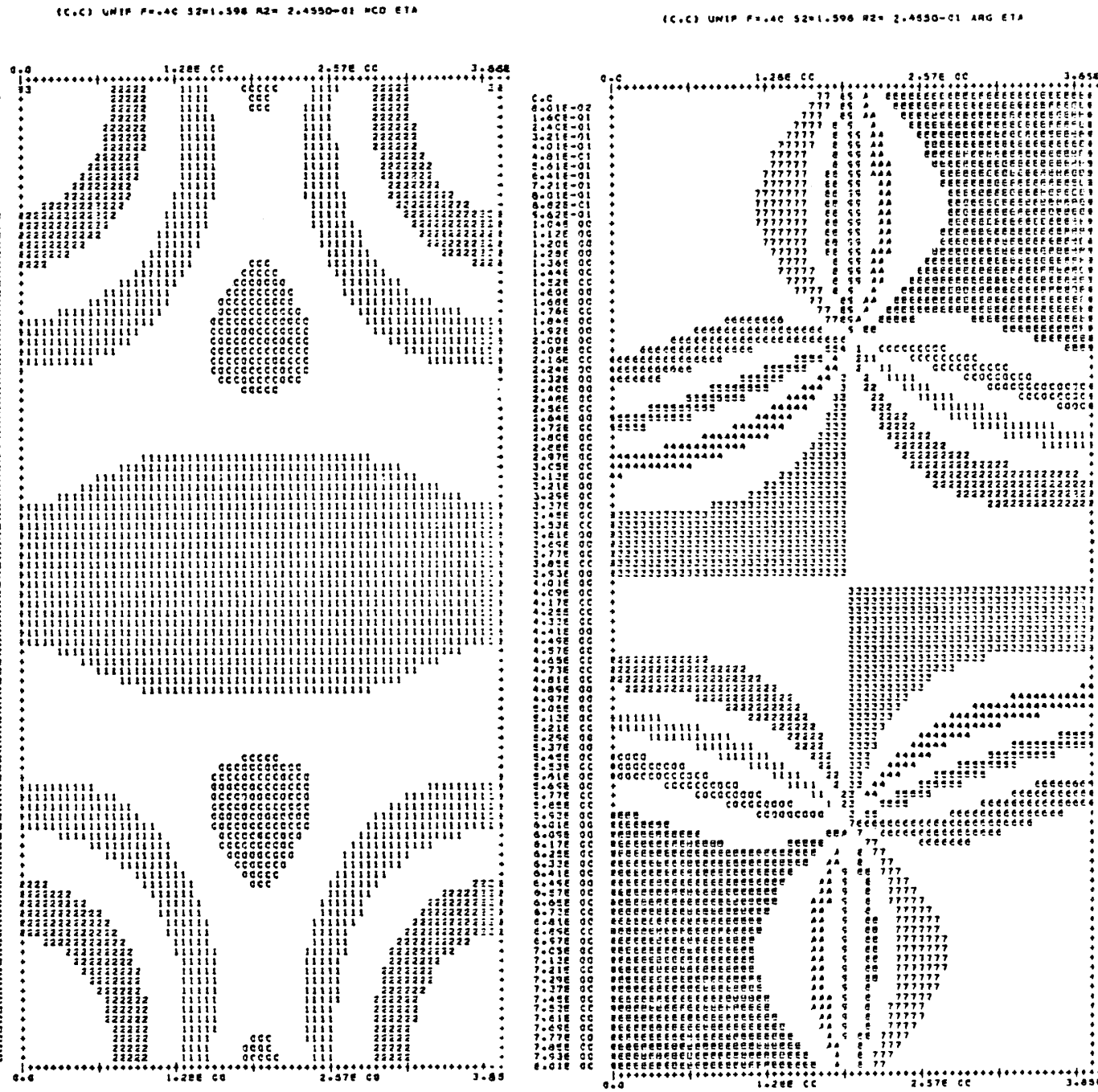
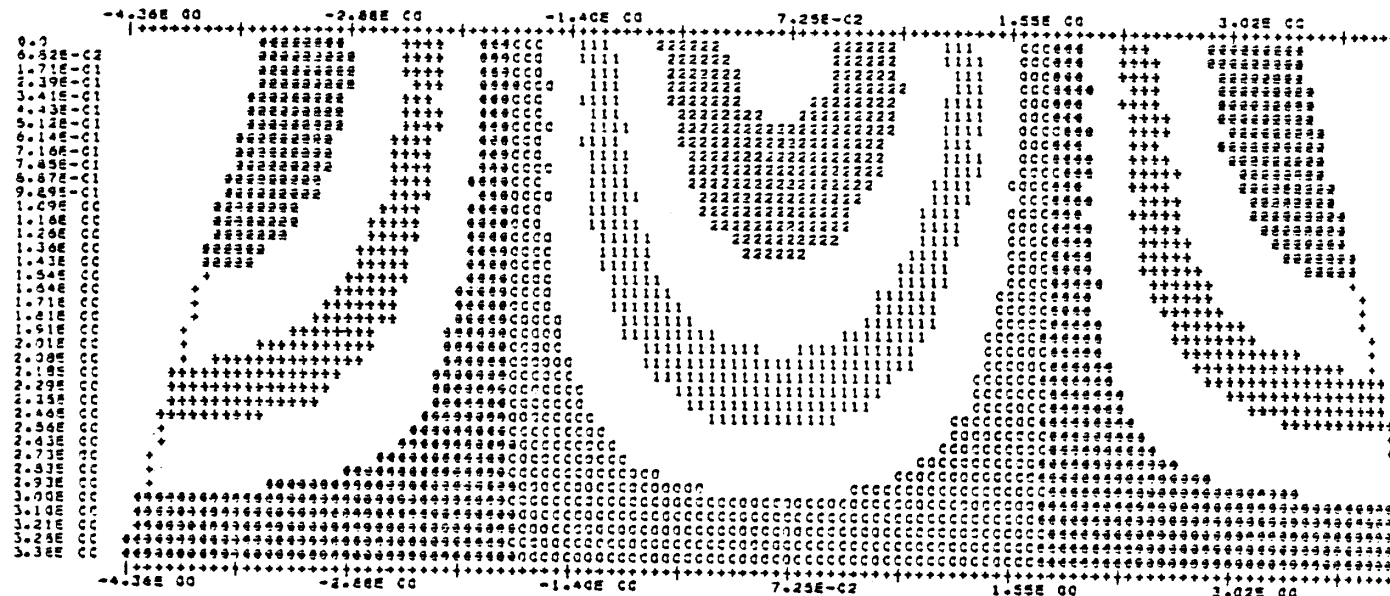


Figure 67. (cont.)

(C,C) BAY F=0.25 S2=4.800 R2= 4.0700 CC REAL ETA



(C,C) BAY F=0.25 S2=4.800 R2= 4.0700 CC IMAG ETA

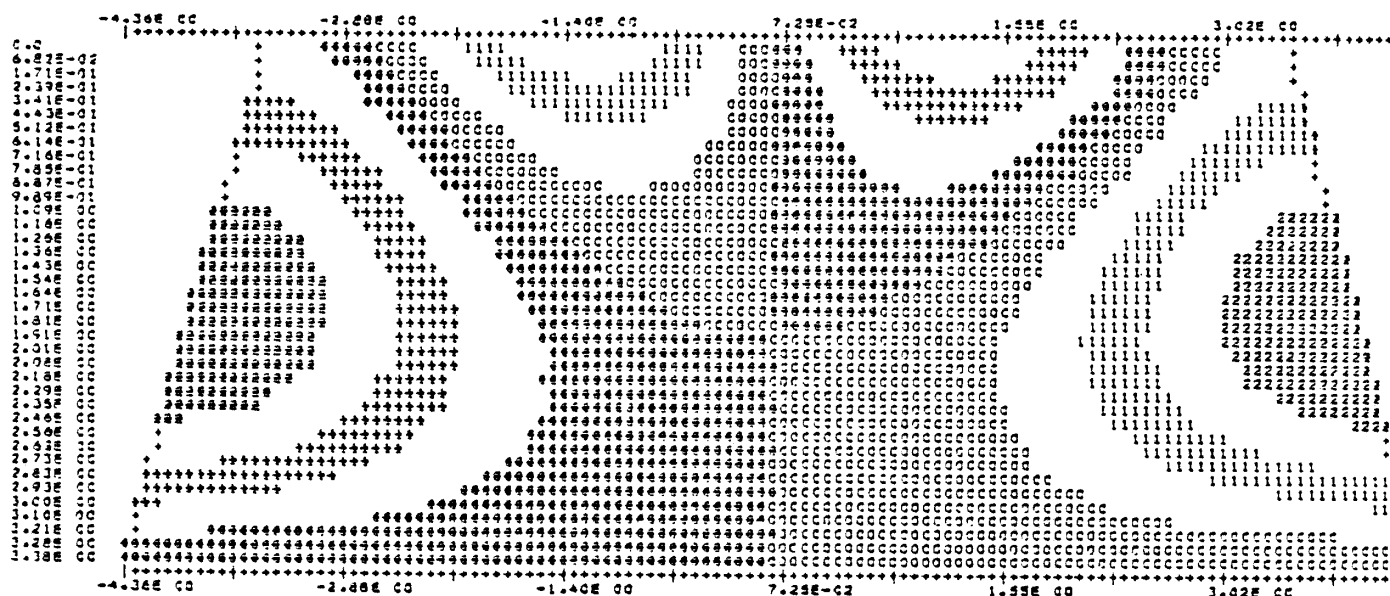
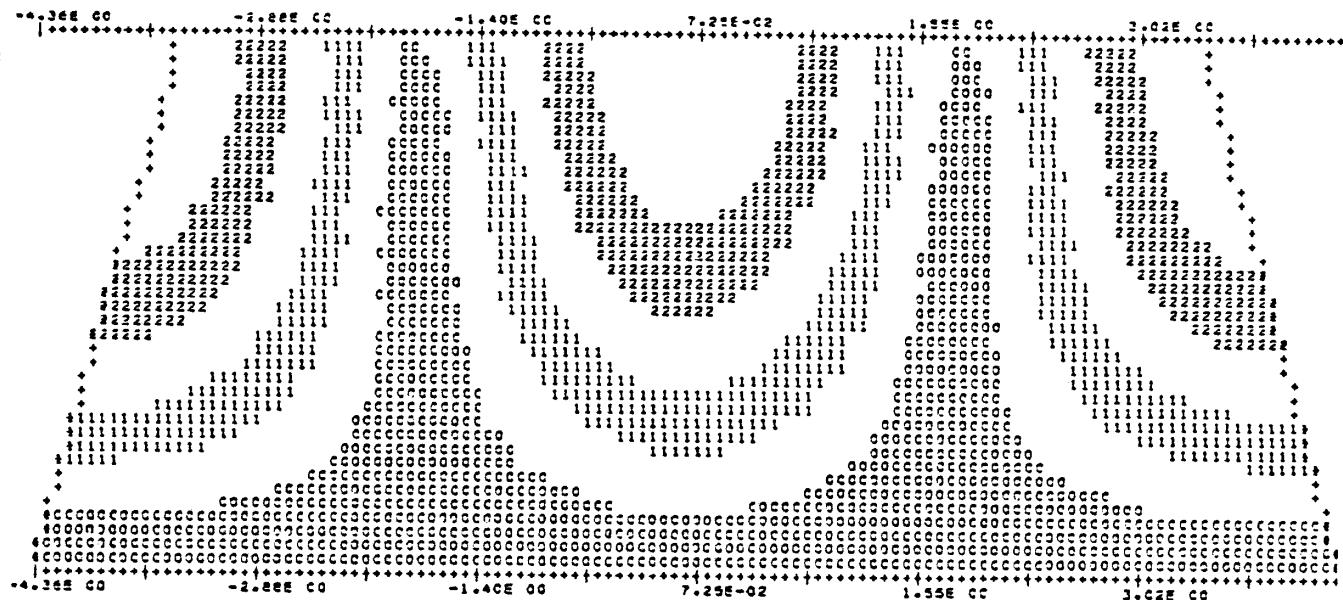


Figure 68. Eigenmode for (c,0) trapezoidal (bay) basin.

$$(r^2, s^2) = (4.07, 4.8), \gamma = 7.5^\circ, f = 0.25.$$

(C.C) BAY F=.25 S2=4.800 R2= 4.0700 00 NCC ETA



(C.C) BAY F=.25 S2=4.800 R2= 4.0700 00 JFG ETA

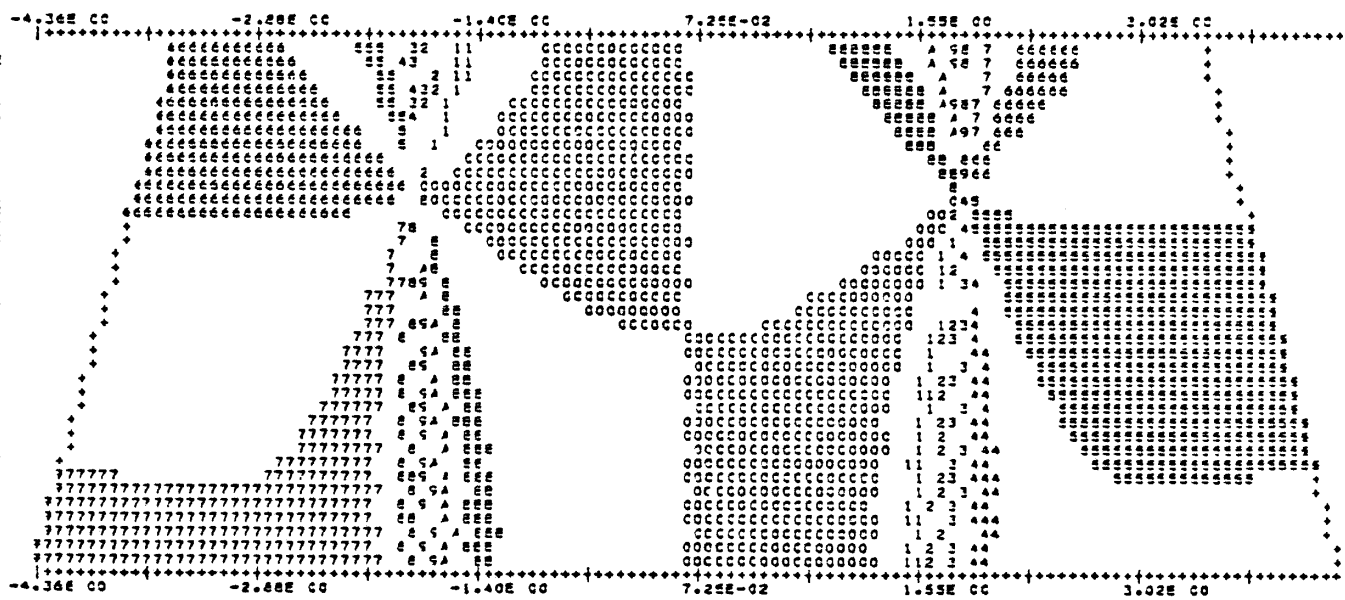
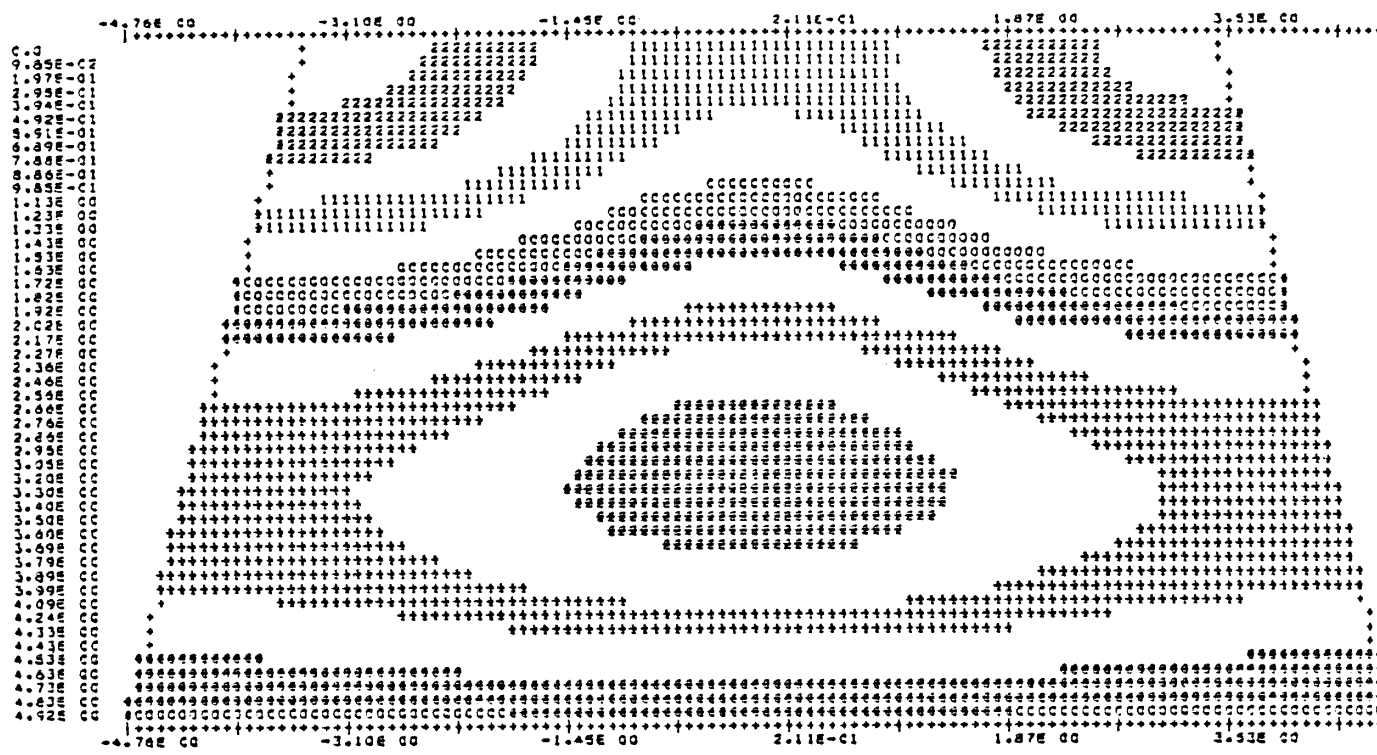


figure 68. (cont.)

(C,C) BAY F=0.25 S2=4.800 R2= 1.9530 OC REAL ETA



(C,C) BAY F=0.25 S2=4.800 R2= 1.9530 OC IMAG ETA

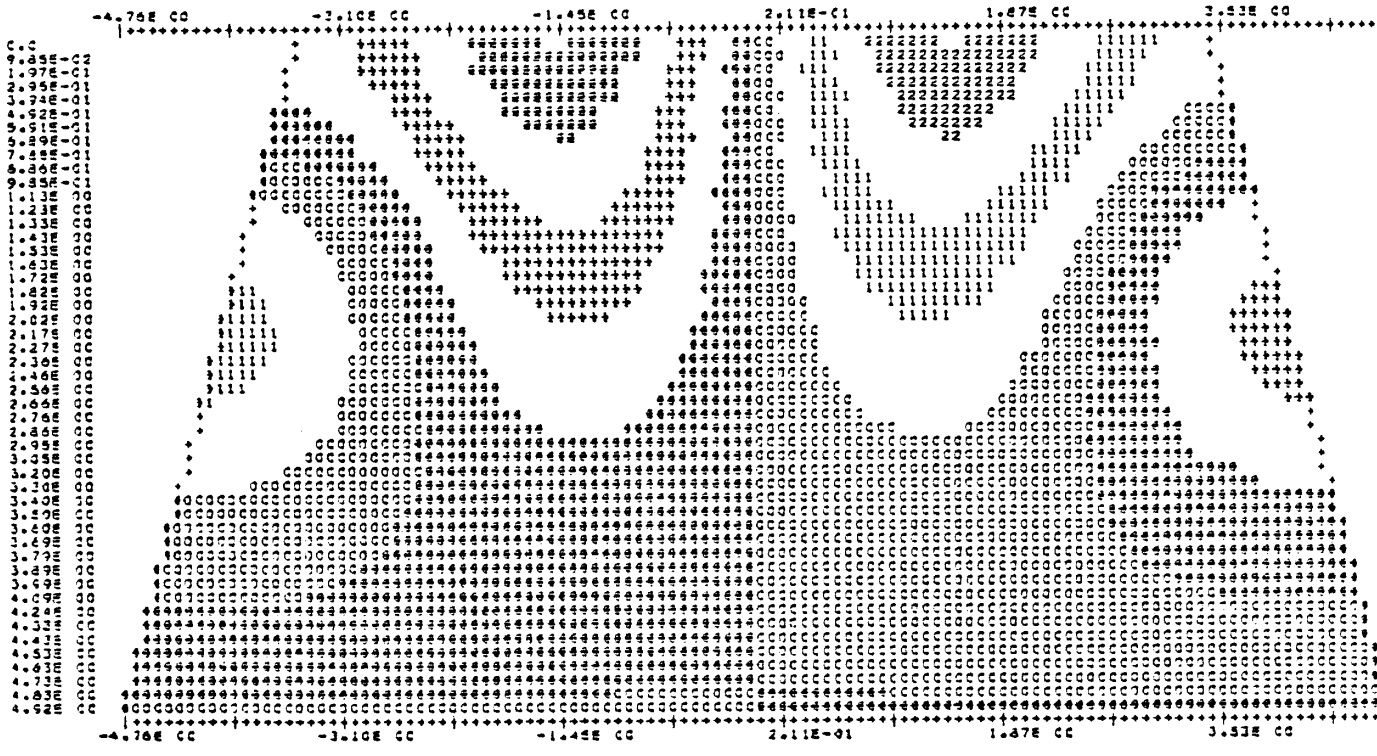
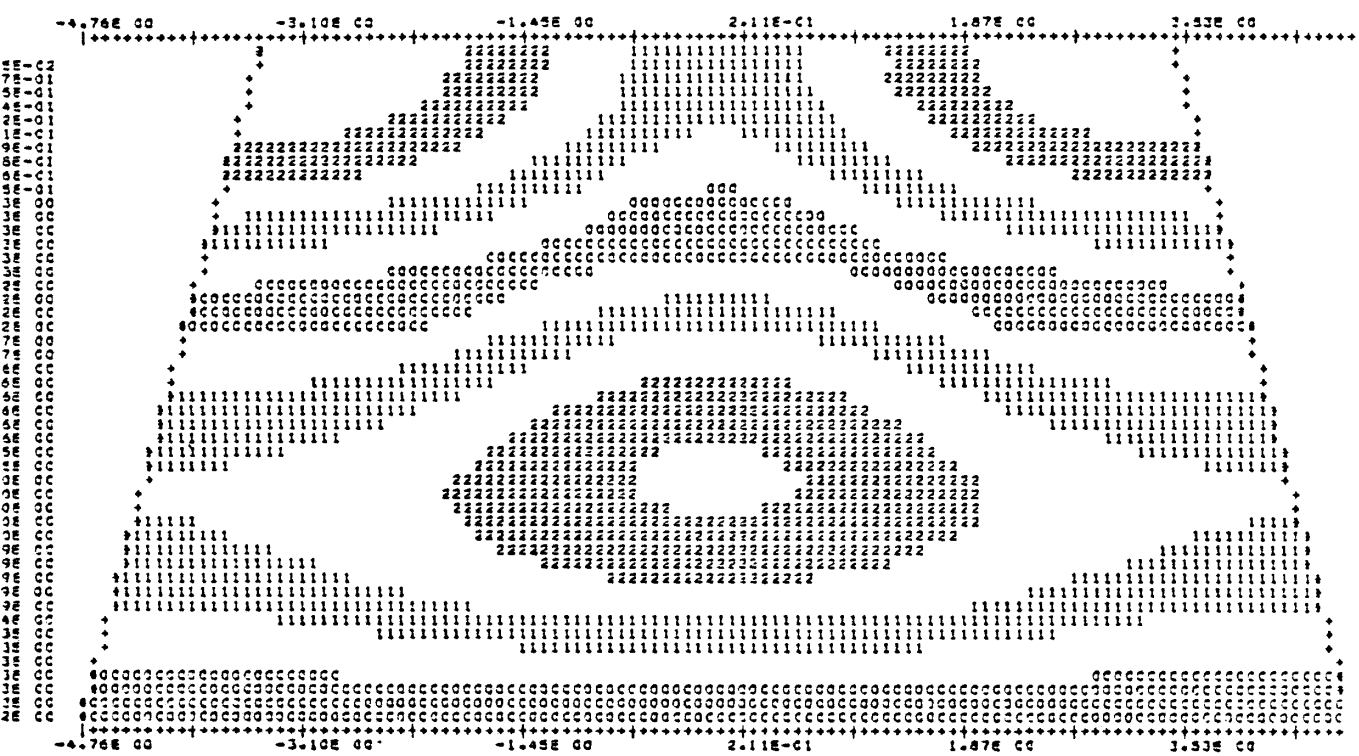


Figure 69. Eigenmode for (c,0) trapezoidal (bay) basin.

$$(r^2, s^2) = (1.95, 4.8), \gamma = 7.5^\circ, f = 0.25.$$

(C,C) BAY F= .33 \$224,800 R2= 1.9530 00 X00 ETA



(C,C) EASY PW=22 S2=4.800 R2= 1.9930 00 ABC ETA

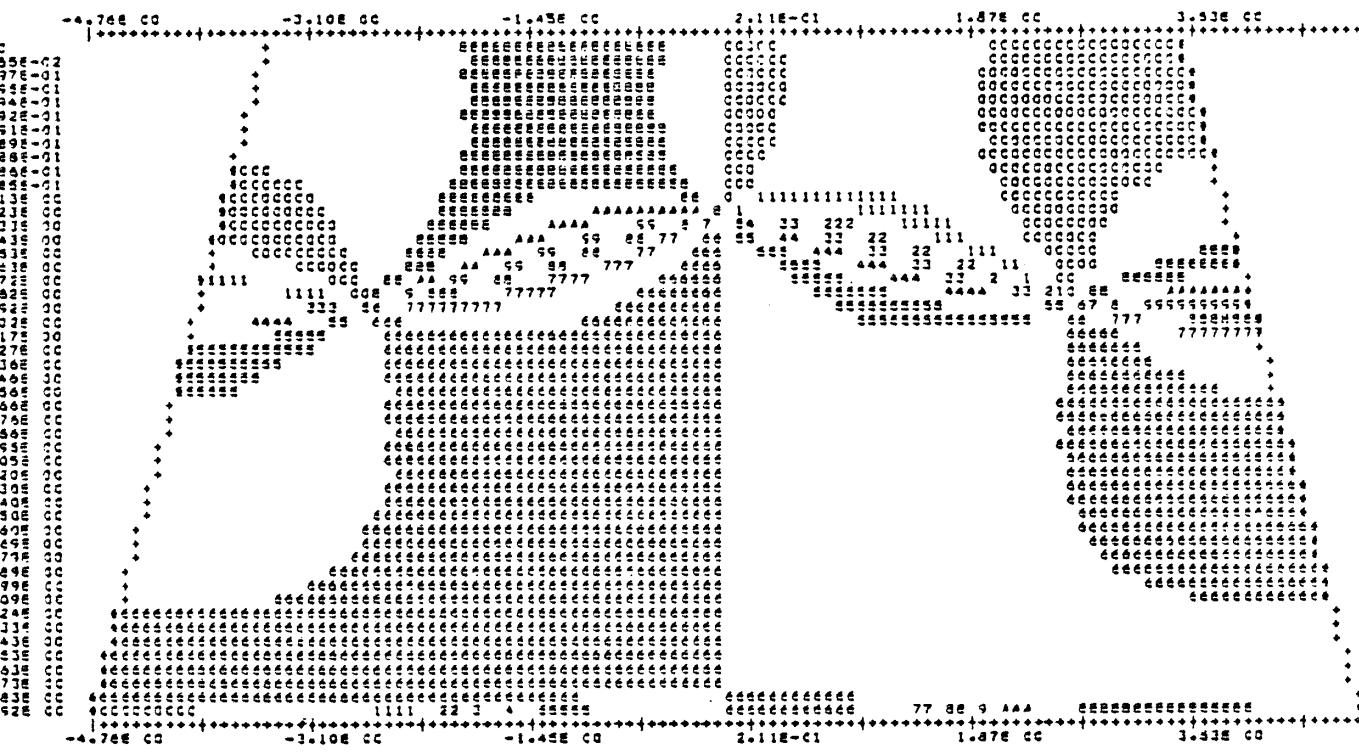
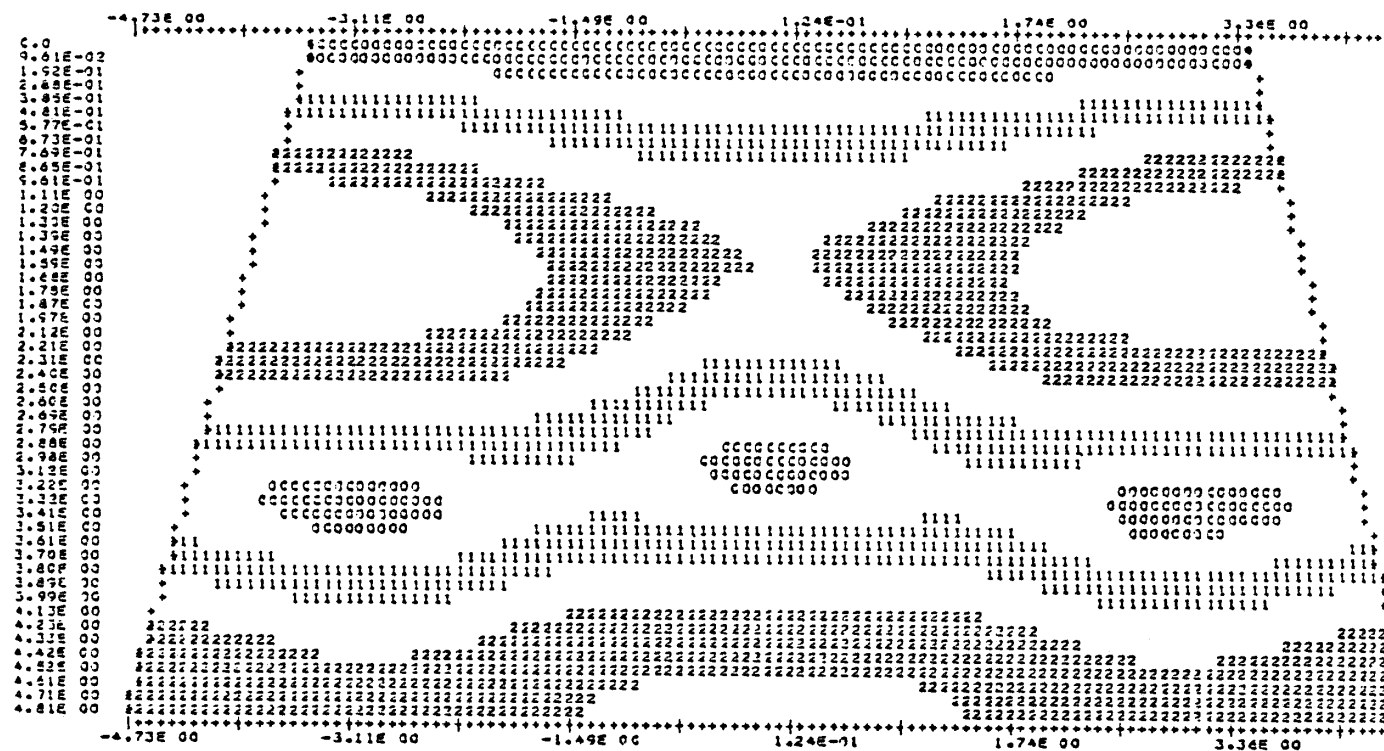


Figure 69. (cont.)

(Q,C) BAY F=.25 S2=4.200 R2= 2.0500 CG MDO ETA



(Q,C) BAY F=.25 S2=4.200 R2= 2.0500 CG ARG ETA

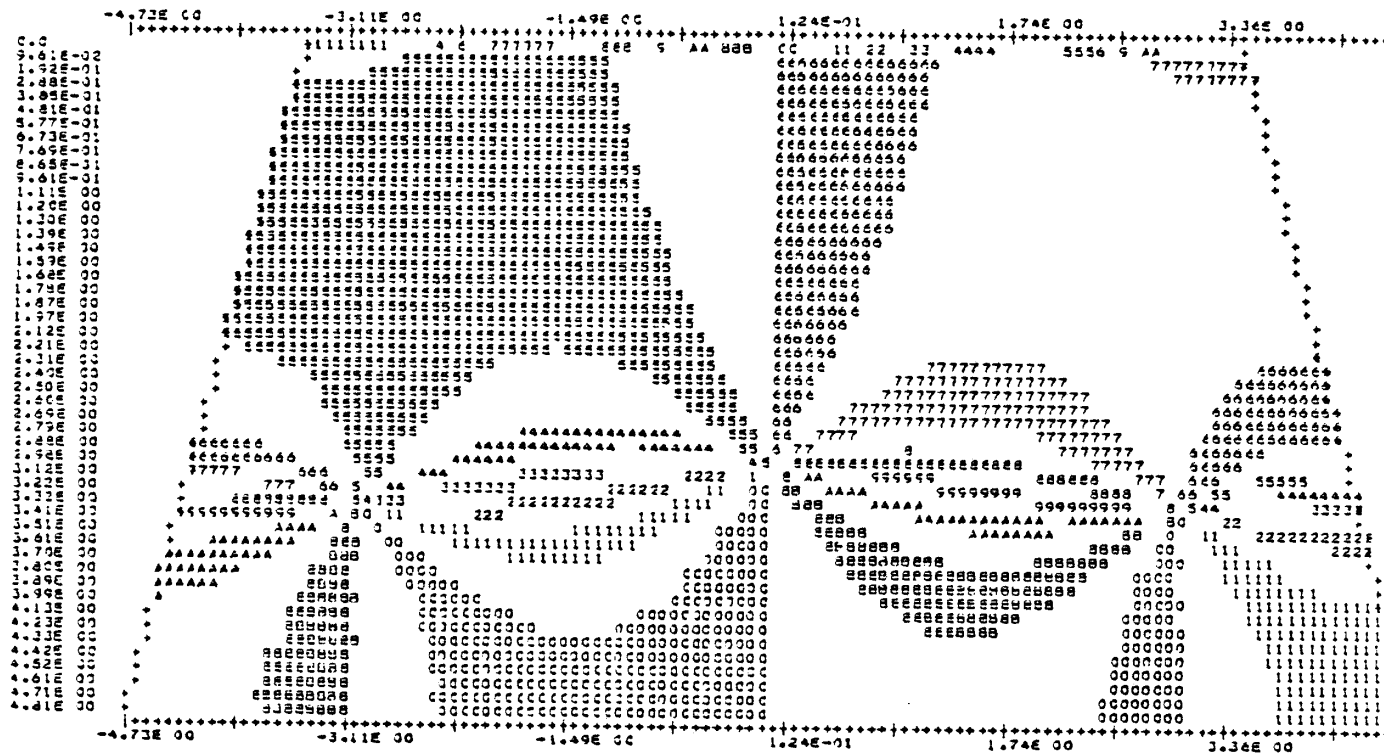


Figure 70. Eigenmode for (0,c) trapezoidal (bay) basin.

$$(\tau^2, s^2) = (2.05, 4.8), \gamma = 7.5^\circ, f = 0.25.$$

(0,C) SAY F=.23 52=4.80€ R2= 2.65CD 00 REAL ETA

(O,C) SAY F= .25 S2=4.800 R2= 2.0500 00 IMAG STA

A 3D surface plot showing a function of two variables. The vertical axis (z-axis) ranges from -4.73E-00 to 1.24E+01. The horizontal axes (x and y axes) both range from -3.11E-00 to 3.34E-00. The surface features a prominent central peak that sharply declines as it moves away from the origin, creating a bell-shaped or Gaussian-like distribution.

Figure 70. (cont.)

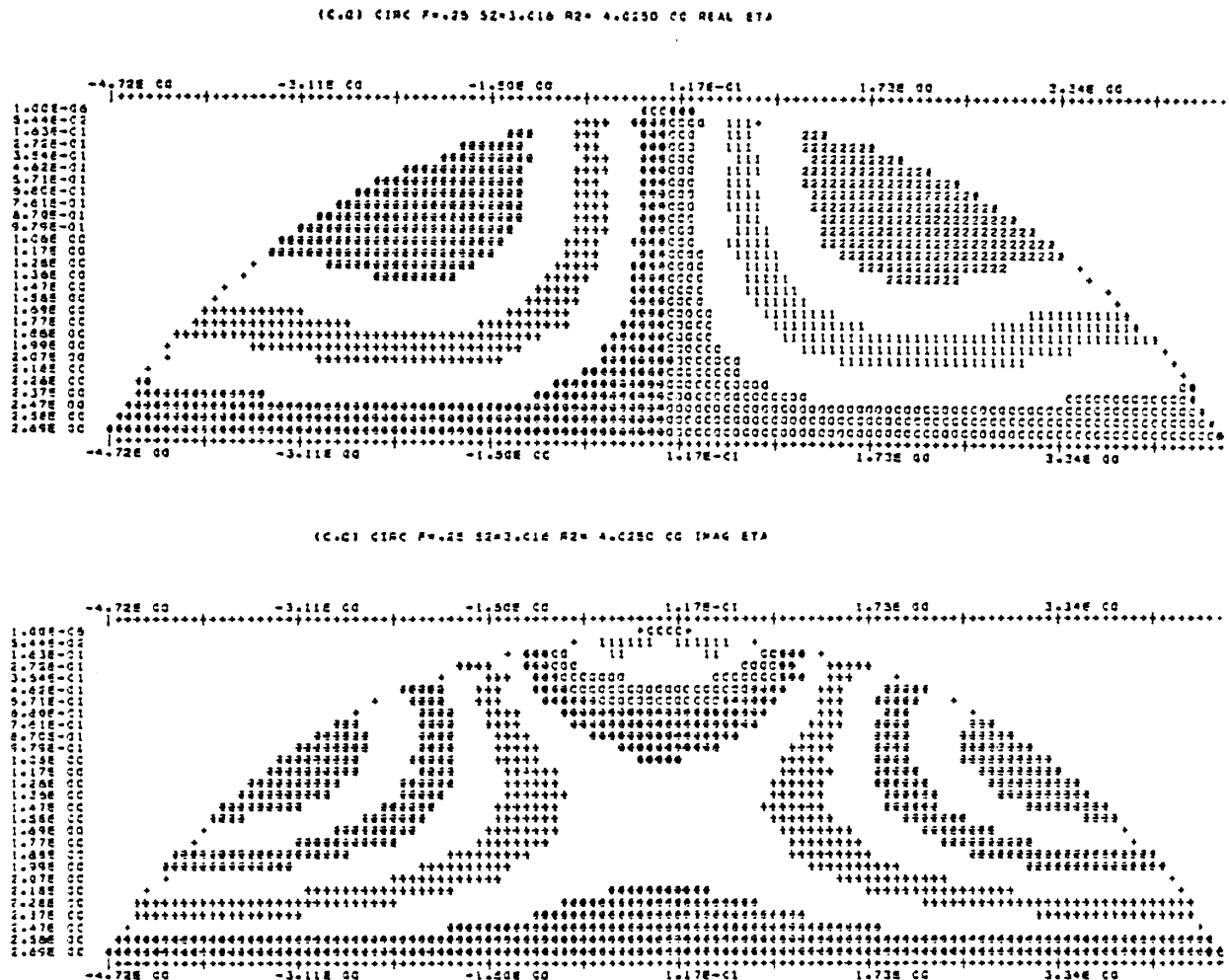
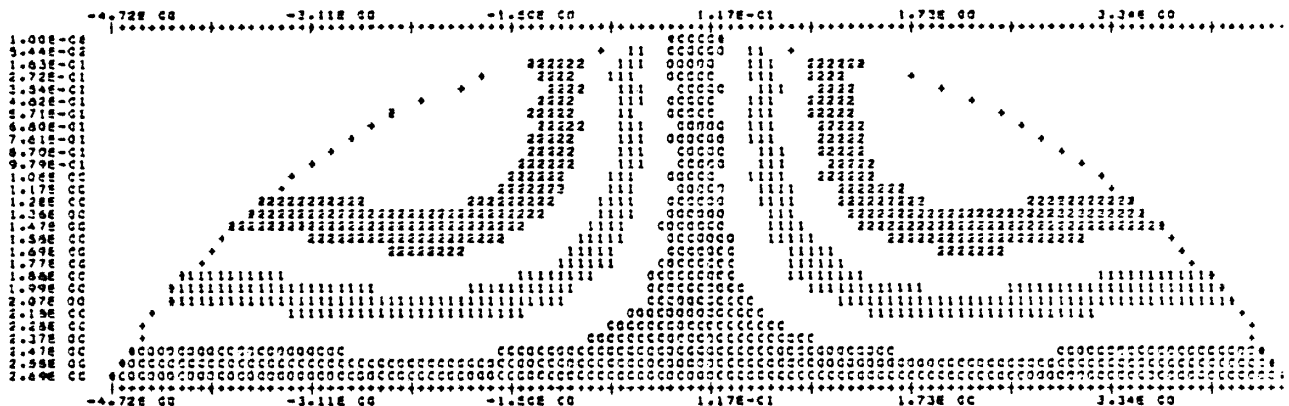


Figure 71. Eigenmode for (c,0) circular segment basin.

$$(r^2, s^2) = (4.025, 3.016), f = 0.25.$$

{C,C} C1AC Pv,2E 92*3+C14 P2= 4.0890 QD RCO R7A



(C,C) CIRC P=0.25 S2=3.018 F2= 4.0250 CC AFG STA



Figure 71. (cont.)

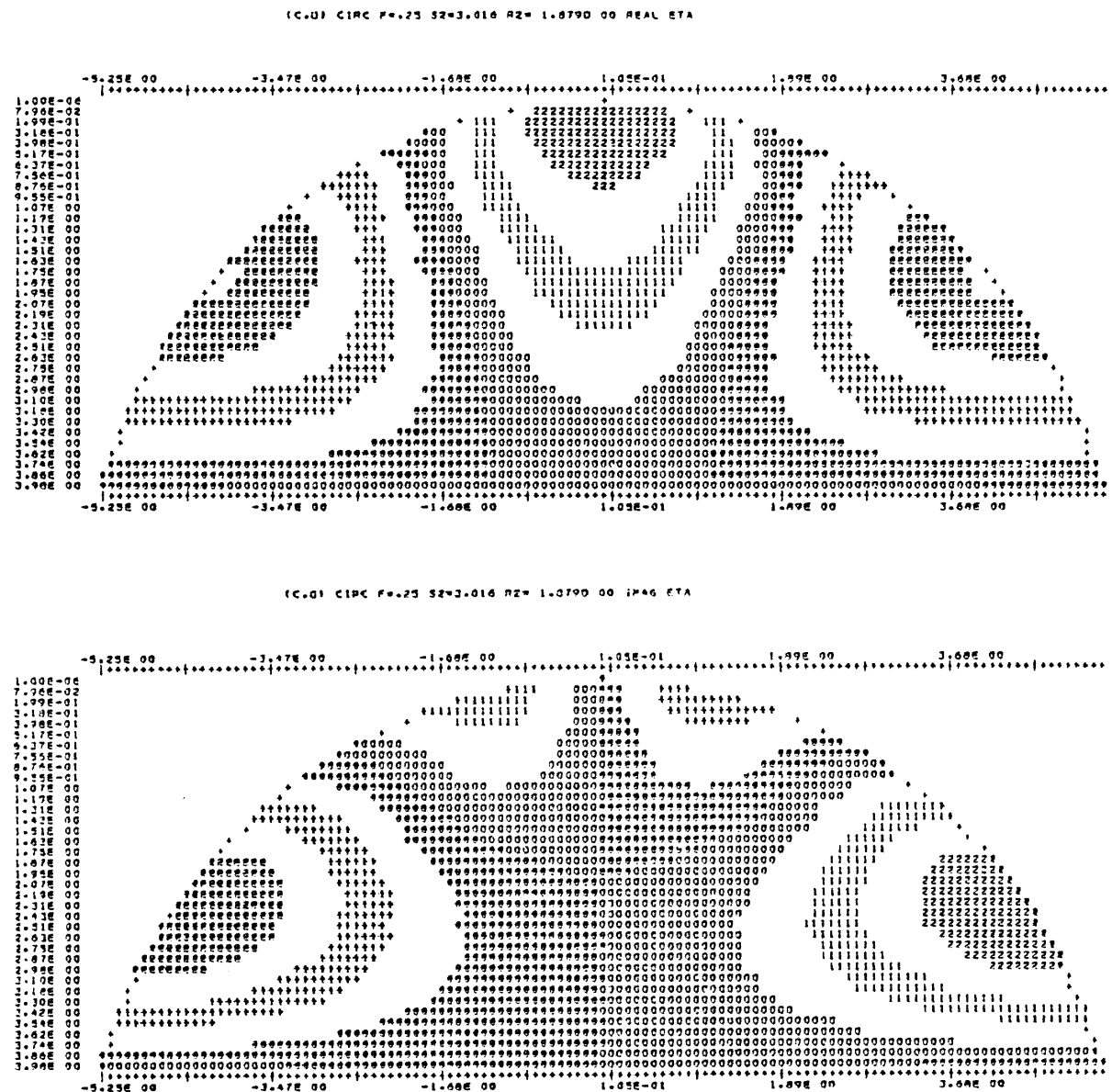
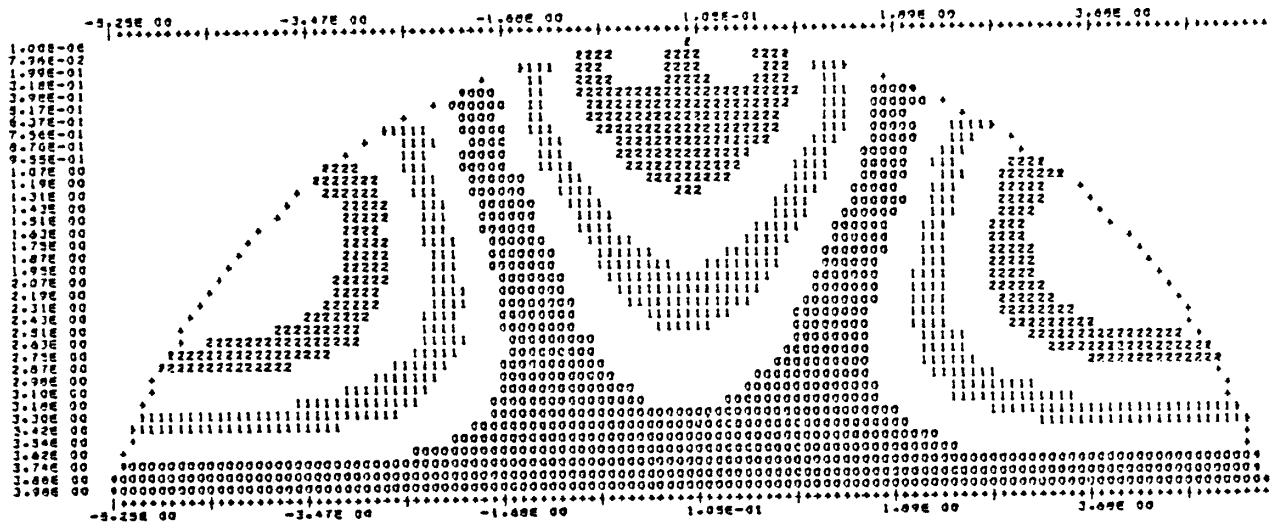


Figure 72. Eigenmode for (c,0) circular segment basin.

$$(r^2, s^2) = (1.879, 3.016), f = 0.25 .$$

(C.G) CINC P=.25 S2=3.016 R2= 1.8790 00 HGO ETA



(C.G) CINC P=.25 S2=3.016 R2= 1.8790 00 ARG ETA



Figure 72. (cont.)